"SAPIENZA" UNIVERSITÁ DI ROMA
Scuola di Ingegneria Aerospaziale

Dottorato XXIV ciclo

TITOLO

Candidato: Daniele Spano .....

Tutor: Antonio Paolozzi .....

Co–Tutor: Reinhart Neubert .....

Roma, Data

Contents

List of Figures

Abstract

In this document will be shown and explained all the experiences and the activities executed during the Ph.D. studies, from November 2009 up to November 2011. The whole work has been developed in "*La Sapienza - Università di Roma*", in a special facility for simulated space environment settled up in 2010. To refine some part of this work a stage in "*GFZ - GeoForschungsZentrum* " has been attended, thanks to the collaboration of Dr. Reinhart Neubert. The aim of this work was been to qualify the CCRs of the LARES satellite. The last developments of the project LARES have led to some results that have called for these kind of tests: thermal simulations have shown an operative temperature of the satellite in orbit in a range from 80°C up to 150°C, higher than the values expected. According to these last results, to ensure the good working of CCRs and of their mounting systems, a procedure of painting of the surface of the satellites has been proposed. Anyway, even if these proposal would assure the drop in temperature, there were some risks about the fragmentation and detachment of the paint during in-orbit phases, after some years of exposition to the space environment. Because LARES satellite aims to measure Lense-Thirring with a very high precision these effects could introduce some errors. So the proposal of validation of the CCRs in simulated space environment in the range calculated by the simulation has been performed to ensure the good working of the op-

tics of LARES satellite, avoiding the painting procedure in case of successful results. All the tests realized on CCRs have shown a good working capacity of the systems even at high temperature, with just some negligible effects of energy loss because of mechanical deformations caused by the severe thermal condition imposed to the system.

Chapter 1

Introduction: LARES Satellite

The measurement of distance has always been a fundamental issue in science, engineering and astronomy in general. So far, laser ranging has been the most accurate technique for measuring the distance to the Moon and to artificial satellites and can therefore give a significant contribution to measure the tiny effects on orbital parameters due to General Relativity. LARES satellite design and its orbit will be optimized to perform high precision tests of Einstein's theory of General Relativity, in particular the direct measurement of the "frame dragging" effect. LARES mission was first presented in response to an Italian Space Agency (ASI) call for ideas issued in 1997 [1,2]. LARES mission is an improvement of the LAGEOS III project proposed in 1986 by I. Ciufolini [3]. Some further developments are described in [4-7]. In 2004 INFN started to fund R&D for LARES in view of a future construction and launch of the satellite.

1.1 Frame dragging effect

In 1918 Austrian physicists J. Lense and H. Thirring derived from Einstein's equations of General Relativity the twisting of the fabric of space-time around a spinning object, in other words, rotating masses drag space-time around themselves as they rotate. Similarly, as the Earth rotates, it pulls space-time in its vicinity and therefore will shift the orbits of satellites near the Earth. This effect is called Frame dragging, or Lense-Thirring (LT) effect, it is so small that it has been hard to measure.

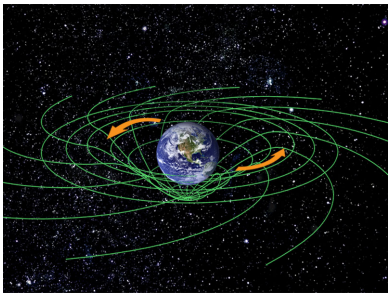

Figure 1.1: Frame dragging effect: artistic reconstruction

The LAGEOS series was designed to be a passive long-lived satellite with a stable, well-defined orbit. As such, it functions as a reference point in inertial space. An international ground-based network of laser ranging station is using the LAGEOS as passive reflectors to obtain ranges to the satellite by precision laser echo-bounce techniques. When a laser pulse is transmitted towards a Cube Corner Reflector (CCR) from a distance R, it is reflected back towards the source by the cube corner and arrives back at the sources at time $t = 2R/c$. Since c is known (actually one source of error is due to small uncertainties in the 4 atmospheric portion of light propagation), then if time t can be measured accurately, the *R-distance* of the cube corner can be derived. This is the classic echo bounce experiment used in sonar and radar

for many decades and the time-of-flight techniques used in particle physics. Since the position of the satellites is determined by some laser ranging stations with uncertainties of less than one centimeter, there was a potential for measuring the two meters per year drift of the nodes of LAGEOS due to the LT effect.

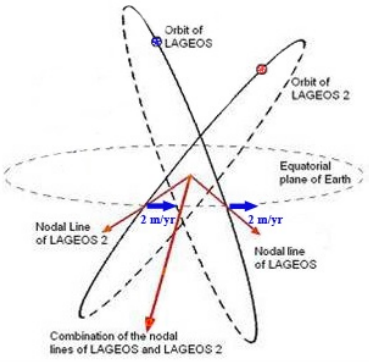

Figure 1.2: Frame dragging on LAGEOS I and II

However, uncertainties in gravitational and non gravitational perturbations, on one single satellite, are bigger than the LT effect. Using a combination of satellites it is possible to reduce those uncertainties at about 10% of the LT effect [9]. The launch of LARES satellite can significantly reduce those uncertainties. The main scientific objective of LARES can be summarized as follows:

- A series of high precision tests of Einstein's theory of General Relativity, in particular a measurement (about 1% accuracy) of the Lense-Thirring (frame dragging) effect due to the Earth's angular momentum and a high precision test of the Earth gravitomagnetic field;
- measurement of some Parametrized Post Newtonian (PPN) parameters;

- tests on the $1/r^2$ law in very weak field;

1.2 Requirements for the structure

Since the orbit of the LARES satellite will probably be lower than those of the two LAGEOS, the satellite should be designed in such a way to minimize all the non gravitational perturbations such as particle drag and thermal thrust, the latter induced by anisotropic black body radiation caused by the temperature difference over the satellite surface. Furthermore for a given satellite altitude, the gravitational perturbations can be reduced by choosing an optimal inclination of the orbit and by using a combination of data from LARES and the two LAGEOS as well as the new models of the gravitational field and the data from GRACE. The non gravitational perturbations are of particular interest since, as mentioned, the orbit will probably be lower than those of the two LAGEOS. Therefore satellite design must be different with respect to that of LAGEOS. Surface-to-mass ratio for the satellite.

1.3 Surface-to-mass ratio

It is well known that the minimization of the cross-sectional area-to-mass ratio

$$\frac{S}{M} = \frac{3}{4\rho r} \tag{1.1}$$

where ρ is the mean satellite density and r its radius, is a critical parameter for a satellite to be used as proof-particle in the gravitational field of Earth. From this simple relation one deduces that the satellite should be very large. However due to obvious limitations on size and weight of

space structures we cannot optimize looking only at parameter r. The main constraint is the mass which has been established to be about 400 kg, i.e.

$$\frac{3}{4}\pi r^3 \rho = 400kg \tag{1.2}$$

Consequently our optimization problem simplifies because the optimal condition will be obtained by taking the highest value for ρ.

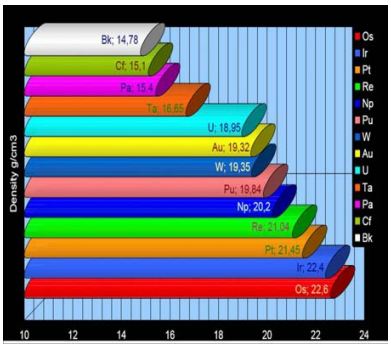

Figure 1.3: Element density table

In the table above are shown all the elements with the highest densities in the periodic table: the bar length is proportional to the element density. The highest value is provided by osmium which reaches 22600 kg/m3. Second in the list is iridium. Osmium and iridium are valued, 12000 $/kg and 14000 $/kg, respectively, which is a bit over half the price of gold, at 22000 $/kg. Platinum's density is very high but price of 43000 $/kg is around twice that of gold. The price of rhenium put it out of the question since at the moment it is selling at 190000 $/kg. So in the hypothesis to be able to collect as much osmium as 400 kg, the cost of the row material would be about 4 million euros, iridium is a bit more expensive, but with a melting temperature much lower, 2410 °C instead of that of osmium of 3045 °C, which makes casting process much easier. The cost is certainly compatible with typical satellite

cost budgets. However workability and procurement time for osmium or iridium would need to be checked. Consequently it seems at the moment that the best compromise is to use tungsten with a density of 19350 kg/m3. However, pure tungsten is not workable and therefore a tungsten alloy should be considered for LARES. There are a variety of tungsten alloys some of which can reach a density as high as 18500 kg/m3. Another parameter that affects the S/M ratio is the geometry of the cavity containing the CCRs. In order to minimize S/M, this cavity should be as small as possible. The following figures show two possible solutions: cylindrical cavities (design directly derived from LAGEOS cavities) and conical cavities that minimize S/M.

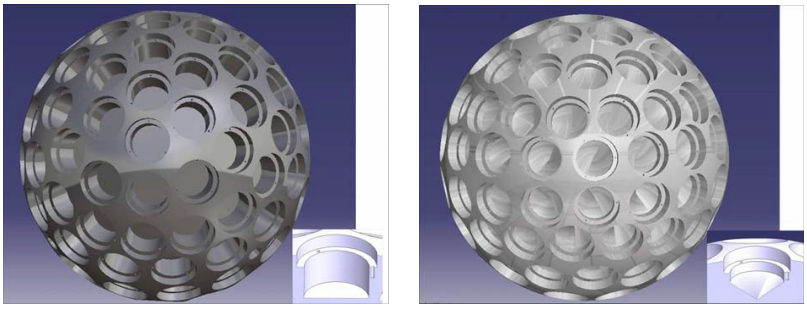

(a) Cylindrical cavities (b) Conical cavities

Figure 1.4: LARES with different cavities types

The choose for the shape of the cavities can be done using the normalized S/M ratio:

$$\frac{M/S_{LARES}}{M/S_{LAGEOS}} \tag{1.3}$$

This quantity is very useful because it provides approximately the improvement factor for the error due to non gravitational perturbations. The red curve with triangular points provides the mass of the satellite as a function of satellite radius. The two curves are relevant to conical cavities and

refers to the satellite completely assembled, i.e. containing all the CCRs and mounting systems. The tungsten alloy considered had a density of 18000 kg/m3. If the cavities were cylindrical the values of M/S would be slightly worse. By considering an alloy at 18500 kg/m3 the M/S ratio will be more favorable. The availability, workability and compatibility with respect to CCR and space environment need to be checked for such an alloy. From Fig. 7 it can be seen that with a radius of 180 mm the mass is about 390 kg with a M/S ratio 2.65 times higher than LAGEOS satellites. If extra payload mass is available on the launch vehicle one could gain more on the M/S ratio. For instance, for payload mass of 700 kg the normalized M/S ratio would reach about 3.4.

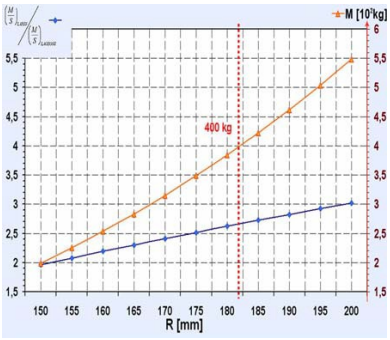

Figure 1.5: Normalized M/S ratio normalized on LARES radius

It may be asked whether it could be more advantageous to have a higher density alloy, even if much more expensive, or to have a heavier and bigger satellite made of tungsten alloy and pay more for the launch. To answer this question a relatively quick study can be performed but it is worth while only if a more expensive mission can be funded.

1.4 Number and position of CCRs on satellite surface

Another important issue to be addressed is the number of CCRs to mount on the satellite surface. The optimal number and position of CCRs depends on the following considerations:

1. A higher number of CCRs reduces the M/S ratio. The reduction is not drastic but needs to be considered.

2. A higher number of CCRs reduces the M/S ratio. The reduction is not drastic but needs to be considered. For instance for a LARES satellite with 102 CCR arranged on a 15 cm diameter sphere the number of CCRs capable of reflecting light varies from 1.3 to 2.0 CCR equivalent, depending on the attitude of the satellite. So, for instance, a value of 1.5 could mean that LAGEOS say three CCRs are reflecting half the maximum energy because of the non optimal orientation. In fact the energy reflected by a CCR is a function of:

   - the angle the incident light rays make with the normal to the front surface;
   - the angle between the light polarization vector and the mounting azimuth;

3. A higher number of CCRs theoretically increases slightly the ranging accuracy, but on the other hand the laser return could become a composition of laser returns from different CCRs. That results in a wider (time wise) laser return pulse and in a more difficult accurate ranging determination. In order to have single CCR laser return, a large recess

(the distance between CCR top surface and the circular upper edge of the cavity) would need to be considered. Single CCR return reduces reliability on laser return because there is no redundancy if one CCR should not work properly. However it should be noted that existing satellites intentionally built with a significant recess performed worse than expected. In addition, a recess on the CCRs will introduce an unknown effect induced by particle drag. It is therefore very likely that we are not going to apply any significant recess on the CCR.

4. One of the perturbations more difficult to estimate is the thermal thrust that is due to uneven temperature distribution over the satellite surface. Such an estimate will be improved by determining the satellite attitude from ground based photometric measurements of sun glints from the satellite or from spin signature contained on the returned laser pulses. Both techniques require a particular choice of CCR arrangement on the surface.

1.5 CCR specifications

The most important parts of LARES satellite are the CCRs. The Far Field Diffraction Pattern (FFDP) of each CCR has to be accurately checked and certified by the manufacturer. In particular, the so called dihedral angle offset between the CCR back faces must be calculated very reliably before the construction of CCRs starts. This angle is a deviation form the 90° dihedral angle: it is necessary to compensate for the velocity aberration induced by the satellite motion and it is required to be able to receive the laser pulses back to the ground station.

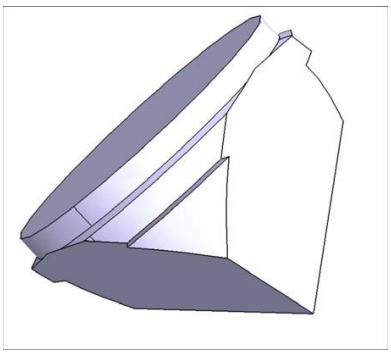

Figure 1.6: View of LARES CCR

Chapter 2

Fundamentals: CCR and FFDP

In the following chapter general informations about retro-reflectors will be shown, in order to better understand the devices employed during the experiences in simulated space environment. All the basic laws of optical physic will be discussed and analyzed to focus the behavior of the devices in operative conditions. Some additional information about general diffraction and diffraction patterns has been included in the chapter to clarify what kind of results has been sought during the tests and what kind of effects has been analyzed.

2.1 CCR

A retroreflector consists in a device provided with three mutually perpendicular reflecting surfaces [1]: the main feature of the device is that it reflects the light back to its source with a minimum scattering of light. Usually it is realized simply "cutting" a cube so that the perpendicularity is respected: for this reason it is often called *corner retroreflector*, or more precisely *Cube Corner Reflector* (acronym: *CCR*).

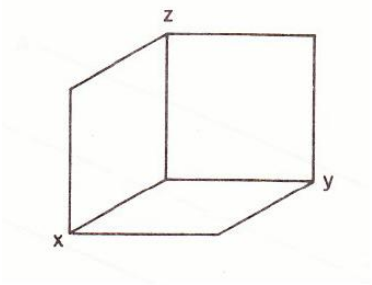

Figure 2.1: Basic Retroreflector

Referring purely to the design of the device, the most common shape employed in space applications is just the corner cube: it can be of two different types:

- CCR Full: it is literally a truncated cube realized in optical glass or other materials. When retroreflection occurs the variation of refractive index must be considered.

- Hollow CCR: it is composed by three reflective surfaces facing each other. In this case there is no change in refractive index. The surfaces are usually covered with optical mirrors or realized in metallic material, depending on the accuracy required by the device.

Retroreflection phenomena can be achieved also using a combination of optical element so that the focal surface of the refractive element coincides with the reflective surface. For this case a transparent sphere and a spherical mirror can be used.

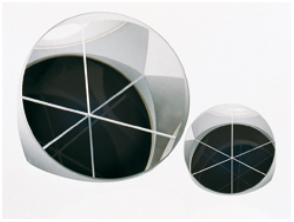

(a) Full CCR

(b) Hollow CCR

(c) Hard-mounted CCR

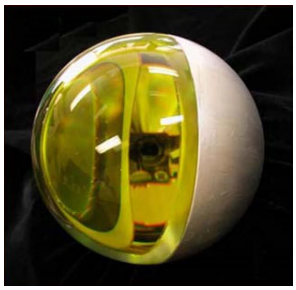

(d) Spherical CCR

Figure 2.2: Various type of CCRs

The principle of operation of a common retroreflector is quite simple: by definition, because the reflected light must be reflected back in the same direction of the incident one, reflecting surfaces must be positioned at 90° each other. Let's consider a single ray of light: when retroreflection occurs, the component of incident light normal to one of the back faces is reversed three times: if light outgoing from the devices must have the same direction of the light entering in CCR, follow that the incidence angle between the ray and the first face on which it is reflected will be equal to the angles that the ray create when it is reflected on the other two faces. This means that incident and reflected rays stand into a symmetry condition. For the same reason it is possible to demonstrate that all rays that hit the CCR cover an equal length path.

If it refers to a full CCR, realized with materials that have refractive

index greater than 1, all the comments above must be revisited considering a range correction for the path length: obviously, from the laws about the refraction, if n is the refractive index of the CCR material, and i and r are the angles of the incident and refracted rays:

$$\frac{\sin i}{\sin r} = n \tag{2.1}$$

it follows that direction of incident and reflected rays will be not the same. From the sum of this effect, that is the symmetry of incident and reflected rays and the three reflection inside CCR it is possible to define the concept of "*active reflecting area*": if the "*output area*" is the reflected image of the shape of the CCR, reconstructed by moving each point on the outline on the face an equal distance on the other side of the vertex, and "*input area*" is simply the area of the CCR, "*active reflecting area*" can be defined as the overlap of the two figures [1]. If a ray is incident outside the active reflecting area it will be not retroreflected.

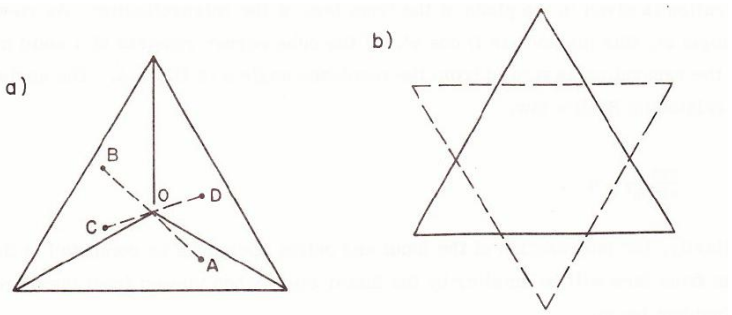

Figure 2.3: Active reflecting area: solid line is the real surface of CCR, dotted line is the reflected one. Active Reflecting Area is the overlap of the triangles

As it has been explained above, in a perfect retroreflector the three faces are separated by 90° angles in order to have the reflected beam exactly anti-

parallel to the incident beam. It is possible to modify the angle by a small amount to have a return signal spitted into several parts in order to better fit the purpose of the CCR. So, changing the dihedral angle of one, two or three faces will be possible to have a return image composed by two, four or six lobes and each lobe corresponds to a particular order of reflection. It is easy to understand that in a common CCR the number of reflection is $3! = 6$.

Referring to basic principle of optics, to have the effect of retroreflection it is necessary that light that enters into the front face must be totally internal reflected inside of the CCR: it is possible to calculate the cutoff angle for total internal reflection using the following law:

$$n \sin r_c = 1 \tag{2.2}$$

where n is the refractive index of the material and r_c is the angle of incidence of the ray. A ray of light will be retroreflected if,

$$r > r_c = \sin^{-1} \frac{1}{n} \tag{2.3}$$

where r is the generic incidence angle. Using this law it is possible to obtain all the angles that not give total internal reflection: they will be contained into a cone of half-angle r_c drawn around the normal to the dielectric boundary [1]. If this procedure is applied on the three back faces it will be noticed that the three cones do not overlap: this means that there will be a small area in which total internal reflection is allowed. Anyway it is possible to calculate the values of incident angles and azimuth angles of the rays that will be totally internal reflected.

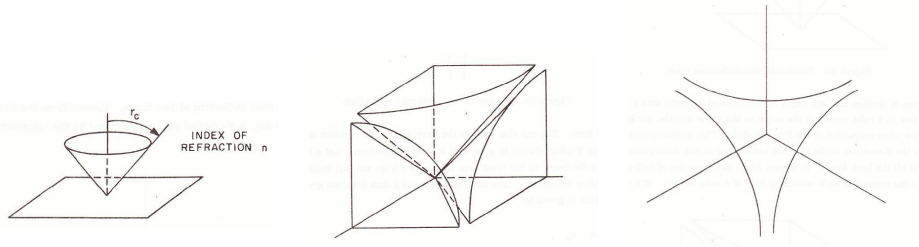

(a) Single Cone

(b) Cones for the back faces

(c) Area with no total internal reflection (inside triangle)

Figure 2.4: Various type of CCRs

2.2 Velocity Aberration

Referring to a retroreflector mounted on a satellite, a laser beam incident on the CCR will be reflected on the same path of the incident beam. Because satellite is moving it is necessary to evaluate a change of reference to better understand what happens to the reflected ray if it is observed from the ground. So the reflected beam will make an angle $2v/c$ with the incident beam, where v is the orthogonal to the light beam component of the relative velocity between satellite and observer, including also Earth rotation. This means that the tracking of the satellite operated by the receiving equipment on the ground will be strictly linked to the relatives movements earth-satellite and to the brightness of the satellite. This component of velocity create also some changes in diffraction image of the CCR: this effect can be reduced at negligible values if the returning beam is intentionally widened, realizing CCR with dihedral angle offset.

2.3 Polarization

A beam of light from a CCR undergoes two refractions and three reflections. Obviously each of the steps introduce into light beam some changes in amplitude or phase or both. These changes will be different for parallel and orthogonal components of the beam in any reflection or refraction: so this means that also the polarization state of the electrical field vector will undergo some changes. All these changes will affect the total energy retroreflected and active reflecting area of the CCR: for this reasons the diffraction figure of the retroreflector will be affected by changes both in amplitude and phase. Because all these changes are strictly connected to the index of refraction, all the changes mentioned above will be strictly correlated to the material composing the CCR.

2.4 Far Field Diffraction Pattern

Far field diffraction pattern (acronym: FFDP) is the distribution of reflected light intensity in a large distance from the reflector (i.e. on ground): it is simply a figure of diffraction of the laser light exiting from the front face of the CCR. When diffraction occurs light deviates from a straight line path and enters a region that would otherwise be shadowed. This deviation from geometrical optics behavior occurs when waves pass through small openings, close to obstacles, or past sharp edges. These patterns can only be described using the wave theory of light which predicts these "smeared" areas of constructive and destructive interference. There are, however, two basic types of diffraction situations, both due to different conditions. These two types of diffraction are called Fresnel (for the near field) and Fraunhofer (for the far field): obviously in this case only Fraunhofer diffraction will be consid-

ered. This phenomenon occurs when both incident and diffracted waves are plane, even if the incident wave is always approximately plane because of the large distance from the source and the reflected wave is not plane at the front face of the reflector. To create such a situation, one must make the distance from the light source to the diffracting obstacle to the observation point large enough to neglect the curvature of incident and diffracted light. In other words, referring back to Huygen's Principle (*"All points on a given wave front are taken as point sources for the production of spherical secondary waves, called wavelets, which propagate outward with speeds characteristic of waves in that medium" (1036)*), when the light reaches the diffracting aperture, there will be a spherical wavefront large enough that it could be considered virtually a plane wavefront. To observe the diffraction figure of an object it is necessary that ray of light hitting the object must be parallel. The plane where diffracted rays create an image is called *Fraunhofer plane*: the image created on the is also called *Far Field Diffraction Pattern*. Far field can be defined as the point in which the light diffracted can be considered as coming from a point source. To estimate the distance where the far field begins, the following law can be employed:

$$z = \frac{2a_0^2}{\lambda} \tag{2.4}$$

where a_0 is the beam diameter of the laser beam at the exit aperture and λ is the wavelength of light emitted by the laser. The laser beam diameter is commonly defined as the value at which the intensity has fallen to 13.5% of its peak value (that is 2σ). To make simple examples of diffraction some qualitative system will be described: this kind of figure of diffraction is often employed during the calibration of the optical system for the observation od the FFDP.

- Single-slit diffraction: a long slit of infinitesimal width, if illuminated by light, has a figure of diffraction composed by a series of circular waves. A slit that is wider than a wavelength will produces some interference effects downstream of the slit. It can be easily explained referring to a monochromatic light source, so with constant phase, and supposing that the light entering into the slit can be approximated to several point sources spaced evenly across the width of the slit. The light outgoing from the slit will have some maxima and minima respecting the superposition principle: because source points are in different position, the phase of the light emitted by this points will vary of 2π or more, due to difference in path lengths.

- Diffraction Grating: it is an optical element that creates a regular diffraction pattern. The form of the light diffracted by a grating depends on the structure of the elements and on their number. Usually an optical grating is composed by several apertures of infinitesimal width and light diffracted can be considered as a convolution of the light diffracted by each element. A very row optical grating can be created also using two apertures on a thin plate in order to have the composition of the single slit pattern. This kind of system is often employed to have a calibration of an optical bench for far field observation.

- Circular Aperture: the far field of a plane wave incident on a circular aperture is often referred to as the *airy disk*. It can be considered as the best focused spot of light that a perfect lens with a circular aperture can make, limited by the diffraction of light. The series of disks all around the airy disk is the *airy pattern*. Both phenomena takes the name from George Biddell Airy.

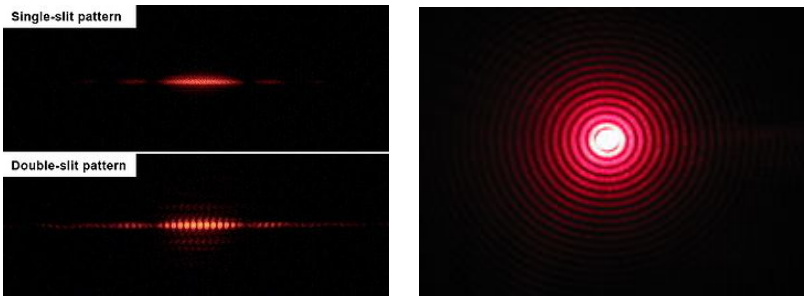

(a) Single-Double Slit (b) Airy Pattern

Figure 2.5: Figures of diffraction

For a cube corner retroreflector, internal reflections make the interference pattern much more complicated, hence the FFDP figure for such an object will have different lobes and different shapes, depending on polarization state of the incident light, on the material and on the type of CCR considered. Usually a CCR have a diffraction figure composed by a number of lobes: if there is no dihedral angle offset FFDP will be created by 5 lobes very close to a central spot. If dihedral angle offset is introduced this lobes degenerate, becoming light distribution without any kind of specific shape: this can be useful to avoid the central spot of light - as in the previous case - so that all light coming from the CCR can be detected (light returns exactly on the laser generator). Also the material could affect the shape of the FFDP, because of the refraction index.

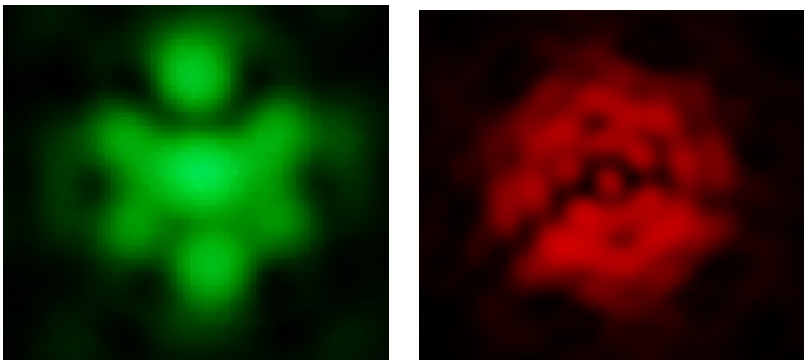

(a) No dihedral angle offset (b) Dihedral angle offset

Figure 2.6: FFDP: example of the influence of dihedral angle offset

Chapter 3

Facility Description

This chapter will show in detail what kind of devices and structures has been employed to perform all the tests: the whole facility has been settled up in 2010 and all the systems and subsystems has been selected or realized by LARES Team: the decisions and the selections taken about that particular kind of devices will be explained, as possible, referring to the ECSS normative for the thermo-vacuum tests. Each of the system composing the thermo-vacuum facility for simulated space environment will be depicted and, where possible, some design drawings or photos will be attached. Particular attentions will be dedicated to the optical table realized to achieve the condition of far field and to take the diffraction figures from the CCRs: because of all the changes in the configurations of optical devices employed, a definitive version of the optical bench has been reached only in April 2011. The attainment of this last configuration will be discussed step by step, with drawings and optical schemes, following all the evolutions and the changes made to reach it.

3.1 Thermo-vacuum System

The laboratory settled up for thermo-vacuum experiment is composed by several subsystems and each of them contribute to perform some of the operations to realize the tests: (TO CHECK!)

3.1.1 Vacuum chamber

The core of the facility is a vacuum chamber produced by *Kurt J. Lesker*, an English company: the chamber is fully made of stainless steel with an aluminium door and has a useful volume of 60x60x60 cm. The chamber is provided with several flanges, all guaranteed for UHV (Ultra High Vacuum): some of these are employed like window to see inside the chamber. There is an optical flange made of fused silica (surface tolerance: $\lambda/20$) that allows precise measurements for the optical circuit, and a more larger optical flange now dedicated to a sun simulator. On the top of the chamber there is a special flange that allow to rotate objects inside the chamber, moving a plug from outside (Magi-Drive system). This system guarantee UHV even if it is a moving part: in order to put the test item in the center of the chamber a special support has been manufactured. This is composed by a bar connected with some screws to the Magi-Drive and locate objects right in the middle of chamber volume. In order to perform very accurate thermal tests it is possible to employ some modeled pieces of Teflon to avoid thermal contact with the bar, insulating the unit under test from the rest of the support. The chamber has also some flanges for electrical connections: there is a flange with 25×2 pins plug and a 9 pins plug. This kind of flange allows to control from outside all the sensors used for monitoring objects inside the chamber: in present configuration the first flange is completely dedicated to sensors,

while the second one is dedicated to other electrical devices employed inside the chamber during the tests (ex. heaters, lights, etc.). The vacuum chamber is guaranteed for UHV, that is up to 10^{-9} mbar.

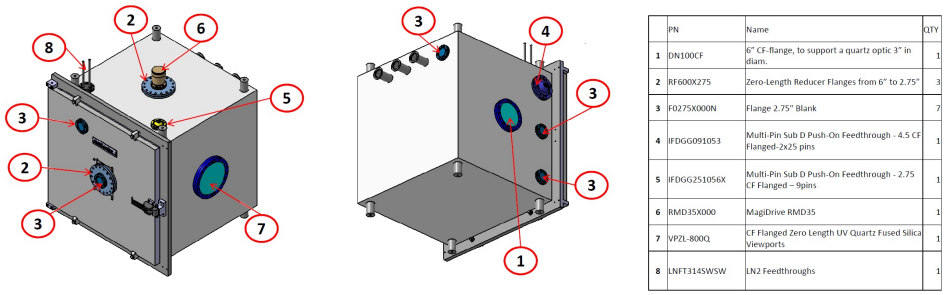

	PN	Name	QTY
1	DN100CF	6" CF-flange, to support a quartz optic 3" in diam.	1
2	RF600X275	Zero-Length Reducer Flanges from 6" to 2.75"	3
3	F0275X000N	Flange 2.75" Blank	7
4	IFDGG091053	Multi-Pin Sub D Push-On Feedthrough - 4.5 CF Flanged-2x25 pins	1
5	IFDGG251056X	Multi-Pin Sub D Push-On Feedthrough - 2.75 CF Flanged – 9pins	1
6	RMD35X000	MagiDrive RMD35	1
7	VPZL-800Q	CF Flanged Zero Length UV Quartz Fused Silica Viewports	1
8	LNFT314SWSW	LN2 Feedthroughs	1

Figure 3.1: Details of vacuum chamber

3.1.2 Shroud

To realize a simulated space environment inside the vacuum chamber a cooling system is needed in order to guarantee a low wall temperature. Often to perform space environment simulation liquid nitrogen or liquid helium is required: hence the cooling system for the vacuum chamber has been designed to be supplied with this two substances. Another guideline for the design of the shroud was the matching with the shape of the chamber, optimizing the minimum useful volume employment and the maximum thermal exchange. To respect all the guidelines, minimizing the costs relative to this subsystem and of the cooling liquid consumption, the shroud has been completely designed by LARES team. It is realized completely with copper in order to oversimplify the manufacturing (bending of the pipes) and then painted with *Aeroglaze Z306*, a special black paint used to simulate deep space. Plates have been modeled respecting all the flanges and the aperture of the chamber's

walls, so that all the pipes must be bent all around the holes of the plates, corresponding to the ones on the chamber. Behind the plates the circuit is split into inlet and outlet lines: the lines are quite near to reach the operative temperature faster - liquid nitrogen outgoing from the circuit helps to cool the plates - covering quite all the surface of the plate. Moreover, to allow the usage of the floor of the chamber in case of heavy duty unity under test, an independent plate has been designed: it is joint to the main shroud with two KF VCR links. The holes on the plates can be closed using some painted copper disks screwed on the shroud if the correspondent flange on the chamber is not employed in the test: with this solution minimum surface exposed to the external environment is ensured. Moreover behind the plate, among the pipes, some small teflon cylinder are positioned, so that the thermal exchange between the shroud and the walls of the chamber is minimum: this solution has been applied in order to reduce as possible the cooling fluid consumption and to avoid that the vacuum chamber walls reach a temperature near to the one of the shroud. Hence, opening the vacuum chamber, the shroud seems like a black empty square: the door is not covered with any plate of the shroud in order to allow the opening/closing of the chamber. With the shroud also the the flange for the feeding of the circuit has been totally re-designed: it is composed by two tubes, bent towards the bottom of the chamber on the inner side, and directed upwards on the outer side, so that they can be fastened with two VCR links to the tubes from the external dewar. A smaller shroud, following the same principles, has been designed: it is linked directly to the feeding flange and is employed for all the tests that not require a total exposure of the unit under test to deep space.

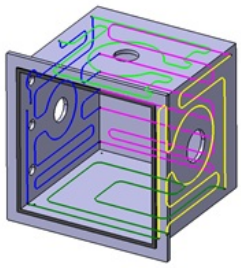

(a) Shroud design

(b) Shroud

(c) Mini Shroud

(d) Mounting system

Figure 3.2: Photos of the two shrouds.

3.1.3 Vacuum pumps

To create vacuum inside the chamber a double stage pump system from *Edwards* is provided. The first stage is a scroll pump (XDS5 series) that allow to reach 10^{-2} mbar. Scroll pumps use intermeshing fixed and orbital scrolls to form non-contacting, crescent shaped gas pockets that are continuously compressed by the orbiting action. This means that, unlike oil-sealed rotary pumps, there is no sealant or lubricant required in the swept volume of the pump [8]. Scroll pumps can run also for 48 hours(RIFERIMENTO DATASHEET): this aspect of these devices is often considered during outgassing tests that has to be run for a great number of hours. The second stage is a turbo-molecular pump (EXT-255DX series) that allow to reach 10^{-6}

mbar: these kind of pumps employ multiple stages consisting of rotor/stator pairs mounted in series. Rotor speed is often very high: the model employed in the lab has a rotational speed higher than 20000 rpm. To reach the pressure and the speed mentioned above turbo-molecular pump must be realized using particular solutions: bearings are usually realized with some special ceramics that must to be lubricated after some cycles of work, or, if the reliability required must be more higher, magnetic bearings are employed. The EXT-250 series has a rotor entirely supported by magnetic bearings in order to have also advantage in cooling the system, in reducing vibration and noise and low maintenance. With this complicated pumps it is easy that a failure occurs. The main rules to preserve the system from typical problems are: taking care of the position of the pump (a right orientation must be respected and dumper system must be taking into account) and avoid to restore pressure into chamber if the pump is still running (a reverse flow can seriously damage palettes of rotor and stator). Moreover it must be switched on only if the first stage of the vacuum system is 100% operative. A sensor positioned on the top of the vacuum chamber and mounted into a special flange allows to measure the level of vacuum reached into chamber (Edwards WRG-S-NW25): it is a combination gauge, using Pirani technology for the upper pressure range, with a seamless switch over to an inverted magnetron for the lower range. For ease of operation and more accurate pressure reading, the vacuum setting of the Pirani gauge is set automatically, while a single push button sets atmospheric pressure. The WRG has an easy-to-program set-point which operates over the entire measurement range. The magnetron uses an advanced technique for highly reliable striking, even at high vacuum or in relatively contaminated conditions. To optimize the lifetime of the gauge, the magnetron voltage is reduced after ignition and the

magnetron operates with a low discharge current [8]. All the measurements and the pumps can be controlled using a special controller from *Edwards* (TIC Monitor) provided with three active gauges for pressure sensors. It is also possible to interface the pressure monitor with a PC in order to have pressure values in real time or to have detection of possible failures event during the tests. The vacuum level normally reached with this two stage system is around 10^{-6} mbar: when shroud is feeded with liquid nitrogen a sort cryo-pumping trap is created. In this way the movements of molecules are strongly slowed down, so vacuum level can reach more higher level, up to 10^{-8} mbar, if no degassing event inside the chamber is happening.

(a) Scroll Pump

(b) Turbo-molecular Pump

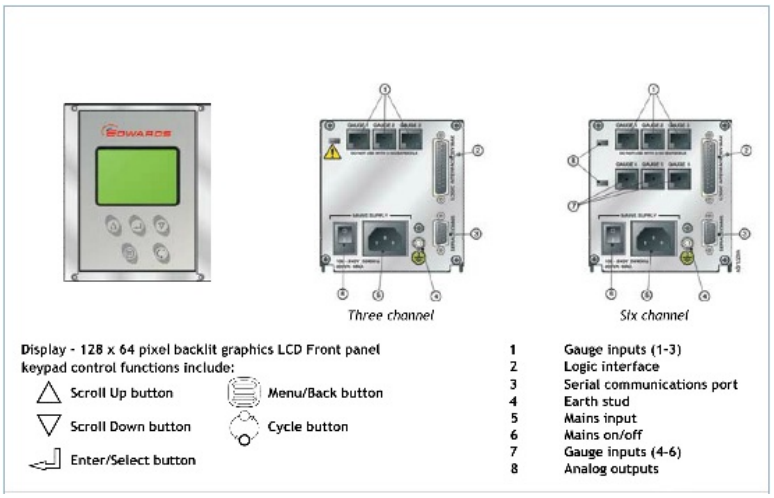

(c) TIC Controller

Figure 3.3: Pumps

3.1.4 Sun Simulator

To perform some of the tests in which the presence of sun light was required a sun simulator has been settled up in the laboratory to complete the space simulator system. The simulator Spectrolab X-10 has been mounted in front of a glass window on the right side of the chamber, so that when it is active most of the active volume of the chamber can receive the sun light. Spectrum intensity from the sum simulator is AM0 +/- 3% class: following the ASTM E927-05 standard (common specification for solar simulator dedicated

to photovoltaic testing) the integrated irradiance across several wavelength intervals can be resumed as follows:

Wavelength Interval [nm]	AM0
300-400	8.0%
400-500	16.4%
500-600	16.3%
600-700	13.9%
700-800	11.2%
800-900	9.0%
900-1100	13.1%
1100-1400	12.2%

From datasheet of the simulator overall irradiance is $1367 W/m^2$ The simulator has a continuous light source realized with xenon arc lamps: these lamps offer high intensities and an unfiltered spectrum comprising UV components strong enough to allow to obtain AM0 spectrum after filtering [3].

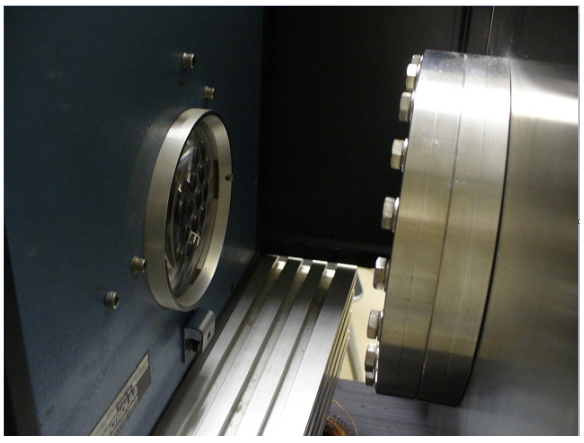

Figure 3.4: Sun simulator facing the dedicated window

3.1.5 Sensors, actuators and data reading

Electrical flange of the vacuum chamber allows to manage several kind of sensors, if special plugs for the sensors are realized or already available in commerce. For all the tests realized some temperature sensors have been employed: the decision about the type of sensor has been made according to the following guidelines. For the tests high accuracy and high reliability were required. Moreover sensors have to be small enough to be glued without problem for sensing also some little parts of the unit under test: hence decision fell on thermo-resistive sensors. Commonly called PT-100 - because they are realized with platinum and their nominal resistance is 100 Ohm - their working principle is well known: they exploit the predictable change in electrical resistance of platinum with changing temperature. The sensors employed are of thin-film category in order to be glued on the parts under test. In order to be employed in thermo-vacuum tests particular care has been taken about the choice of the enclosure of the sensor, in order to avoid degassing. So a special sensor from *Minco* has been selected: S12768 PAX8A. It is suitable for thermo-vacuum operations because of its good accuracy and its enclosure made of kapton (that not suffer degassing) and its temperature range spanning from -200°C up to 200°C.. To increase accuracy of the sensors a three points calibration has been required: so accuracy increased from $\pm 0.1°C$ to $\pm 0.05°C$.

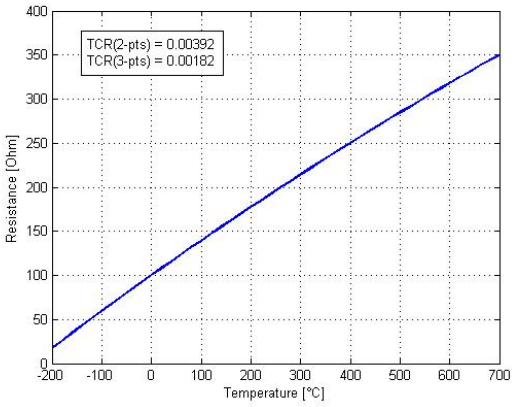

Figure 3.5: Theoretical curve of PT-100 employed.

Data are acquired and transmitted to a PC using an acquisition device "MGC Plus" from *HBM*. To read the data from the PT-100 sensors a special board has been acquired. All data can be shown in real time and processed after the acquisition with "CatMan", a software from *HBM*. Because tests also require that objects inside of the chamber are heated up to 150°C some thermofoil electric heaters has been employed. The enclosure of the device is realized with polyamide (kapton) in order to respect outgassing specs. Because of its light weight and its circular shape it is possible to glue it on the surfaces of the units under test quite easily. It is driven directly by a power supply and all the changes in temperature are made by regulating current or voltage of the device, so that a quite fine temperature regulation is obtained on the parts on which it is glued. The only warning in using this kind of devices is that they have to be glued on curve surfaces to not ease the detachment of the kapton enclosure because of overheating of the internal resistor.

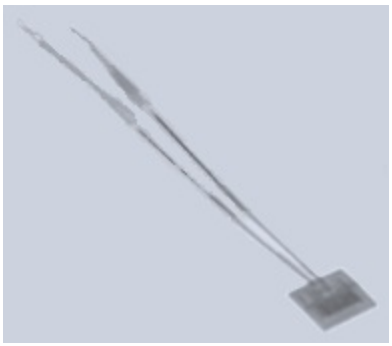

(a) PT-100 Sensor

(b) Heater

Figure 3.6: Sensors and Heaters

3.2 Optical Table

The optical table of the thermo-vacuum facility has been settled up in June 2010: all elements of the optical circuit have been mounted on a special pierced plate realized in honeycomb. This kind of support is usually employed for optical bench because it allows to fix all the instruments with good precision thanks to the equal distance any hole has from the other round it. Moreover the internal structure in honeycomb allow to screw/unscrew any kind of linkage system to the table without a great deal of effort. In more advanced kind of optical table a system that provides an air pad that avoid any kind of vibrations of the components mounted on it. FFDP is obtained simulating the optical path that exist from CCR and the telescopes's CCD matrix: the basic elements to realize such a circuit are:

- Laser: it generates the laser beam that goes through the whole circuit. In experiments often a He-Ne (red) laser is used: according to the ECSS standards laser experiment can be performed using such a laser instead of a more expansive and dangerous Nd-Yag (green) laser

(RIFERIMENTO). For the tests made in Rome a continuous He-Ne laser has been employed: the power was adjustable using a dedicated power supply.

- Mirror: are used to deflect the beam in order to create the desired optical path. A flat mirror is used also to create the reference to calibrate optical circuit.

- Filters: are used if the energy of the beam is too high or if is necessary to introduce a polarization state after a stage of optical circuit. Some of them are adjustable giving more or less energy or changing the state of polarization by rotating the filter.

- Beam Expander/Reducer: such a device is used when laser beam is too small to hit the whole object. Often a small telescope was used as a beam expander. All internal lens adjustments could be realized with a pin-hole, that is a calibrated internal diaphragm that allows to "clean" the beam. An expander could be employed as a reducer by simply inverting the entry side of the beam.

- Beam Enlarger: it is used to make the beam converge on the camera. It is possible to change the zoom rate if a smaller part of the beam has to be analyzed.

- Beam Splitter: this is the core of the optical circuit. Realized as a membrane or as a solid, it splits beam in two parts, with direction fixed by its orientation. Energy loss in this process are usually small.

- CCD Camera: to recover FFDP in real time.

Obviously other elements are necessary to complete the optical circuit: mirror, lens and filter are used to complete optical path in order to reach CCR

with the right energy or in the right position. To realize a good optical circuit is necessary to use great precision in positioning the instrumentation, in order to assure laser beam density - it has to be collimated in every stage, that is after each optical device, to have good images on the CCD camera - and to assure that the laser path is realized without deviation or laser intensity loss. So a little error in positioning a lens or the beam splitter could create error - that is any kind of aberration or a crop - in the final image. In all the configurations that will be shown in this chapter CCR is positioned on the right side of the bench. The first configuration of optical table was realized using a He-Ne laser, a filter, a 3 cm lens, a flat mirror to deflect the beam toward the CCR, a pellicle beam splitter, a lens to make the beam converge, an enlarger and a webcam without objective. This configuration was affected by several problems:

- The laser beam needed a filter to better modulate its power and to avoid overexposure of the CCD camera. Moreover the beam from laser generator, even if it is expanded by the lens, was also too small to hit the whole CCR. Moreover laser from He-ne is composed by a great number of plane wave: so, on the exit, beam aim to diverge before hitting the lens or the beam expander, losing most of its energy, and resulting not collimated.

- The filter could create some kind of disturbance on the laser beam (misalignments, reflections). Moreover, to avoid that the beam returning from the beam splitter make interference with the beam from the laser generator, the filter was mounted with a little angle of deviance, in order to make all the reflections lost. Offset angle had to be calculated with great precision to avoid reflection or beam loss.

- Even if a lens is used to enlarge the laser beam, its diameter was not wide enough to hit the whole CCR. In this configuration 35 mm lens has been employed: the spot outgoing from the lens was not wide enough to hit the whole front face of the CCR.

- The pellicle beam splitter has some problems for its assemblage on the optical support used for the other components: because it was very large and very light the mounting system does not allow a perfect positioning and so it results twisted with respect to the beam path. Moreover because of the not perfect mounting, return beam was distorted form any mechanical movements of the pellicle (that is vibrations induced by steps or by pumps, air moving around the table, etc.).

- The camera used (webcam) was not a specific instrument to see FFDP: it has an automatic black level regulator that forbid to see the real image of the FFDP.

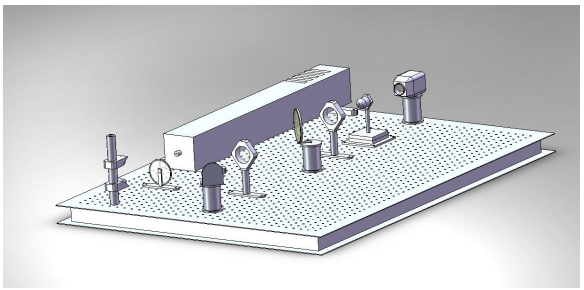

(a) Trimetric View

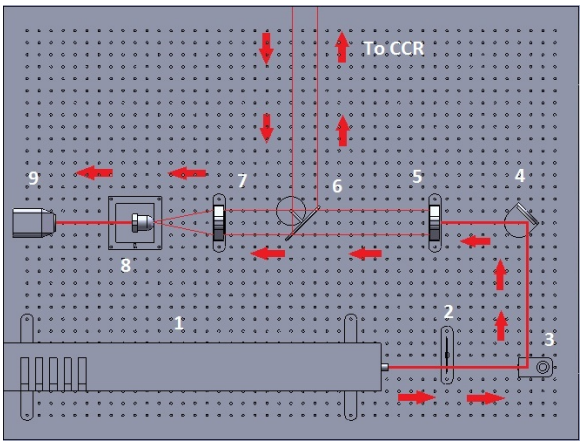

(b) Optical Scheme

Figure 3.7: Optical table, first configuration: 1. Laser 2. Filter 3. Elevator 4. Mirror 5. Lens 6. Beam Splitter 7. Lens 8. Enlarger 9. Camera

In the second configuration the pellicle beam splitter and the webcam were substituted with a solid cube beam splitter and a professional camera for night vision. Moreover the optical circuit was provided with a beam expander to have a more wide laser beam right after the filter. In this configuration other problems faced up:

- Using the expander, some of the laser beam power density was lost on the contour of the spot: even using a pin-hole inside the expander the density loss remain the same. In a few words an expander make

laser beam not collimated. Even if the beam was expanded, it was not enough wide to hit the whole CCR. Moreover the internal lenses could introduce some kind of aberrations depending on how the laser beam hits the entry lens of the expander - if beam enters perfectly following optical axis or if it enters a little deviated.

- Solid cube beam splitter solve all the problems introduced by the pellicle beam splitter: could only be some cases of barrel distortion or beam cutting if beam enter not straight into it.

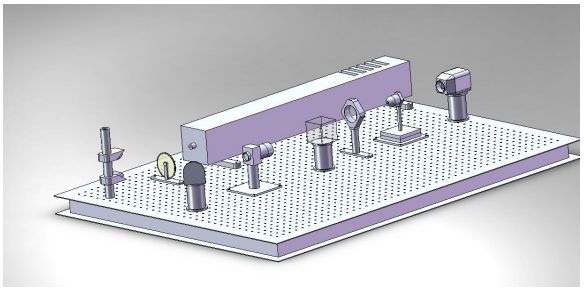

(a) Trimetric View

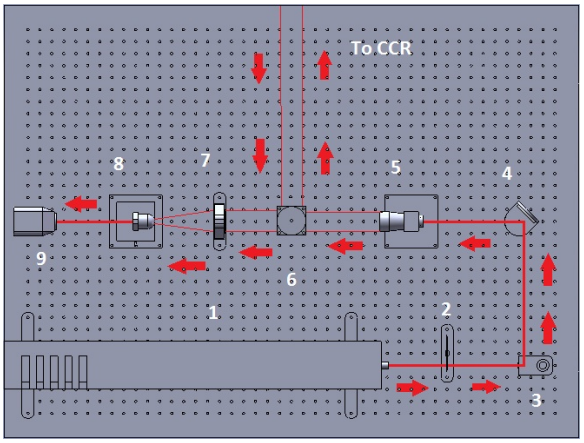

(b) Optical Scheme

Figure 3.8: Optical table, second configuration: 1. Laser 2. Filter 3. Elevator 4. Mirror 5. Expander 6. Beam Splitter 7. Lens 8. Enlarger 9. Camera

After some other configurations obtained moving optical components on the table, a better configuration has been reached (Fig. 2.9). The He-Ne laser has been substituted by a laser diode coupled with a mono-modal optical fiber, filter has been eliminated, an achromatic doublet has been placed right after the laser generator and another one has been placed before the enlarger. In this way the optical circuit function as follows: the laser beam outgoing from the diode goes towards the first lens and it is expanded. Then it is reflected by two mirror towards the beam splitter, so that a part of the beam could enter in the chamber: the beam returning form the CCR is directed by the same beam splitter towards an achromatic doublet that let the beam converge to the microscope objective. The beam is then directed towards the CCD camera. With this changes the following advantages has been gained:

- Beam from the fiber optical laser is more collimated then the one form He-Ne laser: optical fiber work as a waveguide and make beam more precise and more dense in the outgoing spot. With the laser diode the outgoing waves are spherical: this means a more converging beam at the exit and so, when beam hit the lens, all energy is conserved, because spot in the middle is stronger than in the external part. Moreover laser diode can be positioned simpler on the optical table, thanks to its small dimension and to its light weight. Obviously is indispensable to use a mounting system to avoid movements or vibrations: particular attention must be payed to the position of this device to avoid any kind of deviation from the calculated optical path.

- Achromatic doublets replaced beam expander: the last one could introduce a lot of aberration on the outgoing beam depending on how beam hits his entry lens. Positioning lenses in the right places is possible to have an outgoing beam large and collimated: this kind of lens not

introduce achromatic aberration and, if it positioned in the right place - with great precision on the perpendicular plane respect to the incident beam and according to the focal distances - it does not introduce any kind of geometric aberration. The lens positioned right before the beam microscope objective is used to make the beam converge on the entry lens of the objective: is very important to realize the condition of coincidence between the focus of the lens and the boundary of the microscope objective. With this condition the beam is totally introduced in the enlarger and, if the CCD camera is positioned in the right place, the whole image of FFDP is available, with minimum distortion.

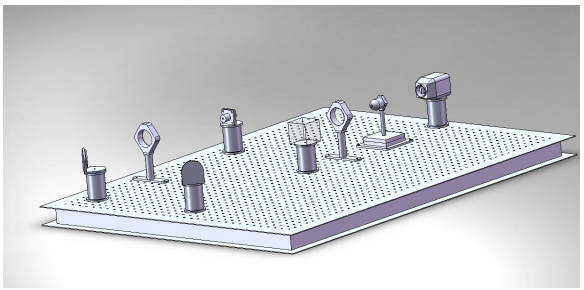

(a) Trimetric View

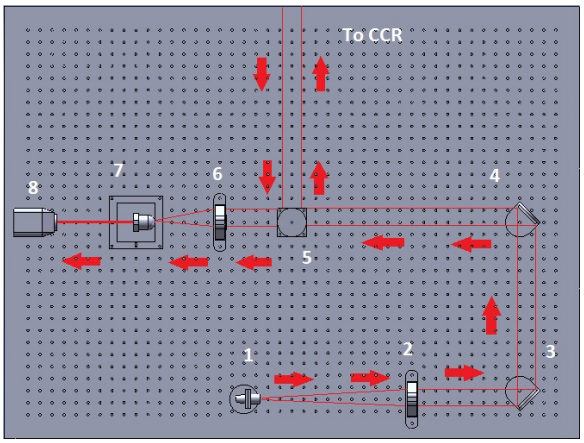

(b) Optical Scheme

Figure 3.9: Optical table, third configuration: 1. FO Laser 2. Lens 3. Mirror 4. Mirror 5. Beam Splitter 6. Lens 7. Enlarger 8. Camera

In this configuration there are some critical points: even if the laser beam is collimated and the spot is enough dense the correct mounting of the lenses is fundamental to assure the absence of geometrical aberration along the optical path. If lens is mounted with an angle offset in the plane perpendicular, respect to the direction of the incident beam both spherical aberration or coma can arise. Even if chromatic aberration is suppressed by the achromatic characteristic of the lens, presence of geometrical aberration could invalidate the FFDP. As seen before the laser beam has to hit every stage of the optical circuit as close as possible to the nominal angle: another critical point is

the enter lens of the microscope objective. The laser beam outgoing from the convergence lens has to enter perfectly orthogonal inside the objective to avoid cropping of the final image or any other kind of distortion. The CCD camera has to be positioned in the right point beside of the enlarger: because of the series of lenses inside the microscope objective make the beam converge at a distance fixed depending on zoom rate, it is fundamental to make the focus converge on the CCD of the camera, in order to have an image without dimensional distortion. Because the camera has a reduced systems of setting for the exposure and the correction of the background noise the patterns acquired has to be processed with a software to filter the FFDP and make clearly visible only the zone of interest. In order to reduce the problems introduced by the components of the last configuration described, optical table has been re-arranged in March 2011, thanks to the advices of Dr. Reinhart Neubert: all the changes introduced in the new optical bench has been applied also storing all the experiences from the previous configurations. The actual optical bench is settled up using the following components:

- Fiber optical laser
- Solid beam splitter
- New lens (from a telescope) of 800 mm diameter and 600 mm of focal length
- Beam enlarger (microscope objective) with 40X magnification
- Canon EOS 1100D

The number of the components on the optical table has been reduced: the most relevant differences form the previous configurations are the new lens and the new camera. The first one has been acquired in order to have

a more stable FFDP and to have a more large laser beam ingoing towards the breadboard if referred to the previous 50 mm lens. The camera for night vision has been replaced with a common camera in order to modify the parameters for exposure and light sensibility: this change was necessary to reduce the noise introduced in the patterns by the external environment. The lens has been mounted on a more stable and precise slit system in order to better find the focus point and so have a more stable pattern. With this new configuration most of the previous critical points has been resolved: some of the residual aberrations has been reduced, the better focusing makes the patterns stable even if the CCR moves - only for translations, rotations changes FFDP - inside the chamber and background noise of the patterns has been reduced. The alignment procedure for the new optical bench is changed and now it is more simple: the micrometric slits under the the new lens (x and y movements) and the micrometric slits mounted on the beam enlarger (x and z movements) allow to have a more precise positioning of the components.

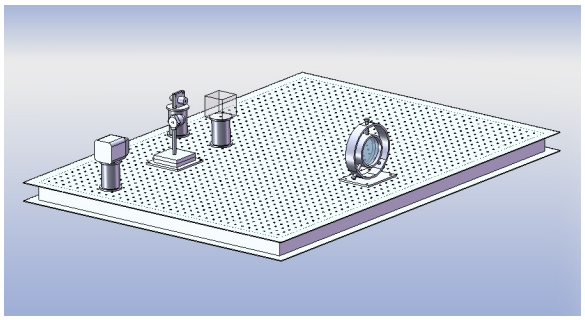

(a) Trimetric View

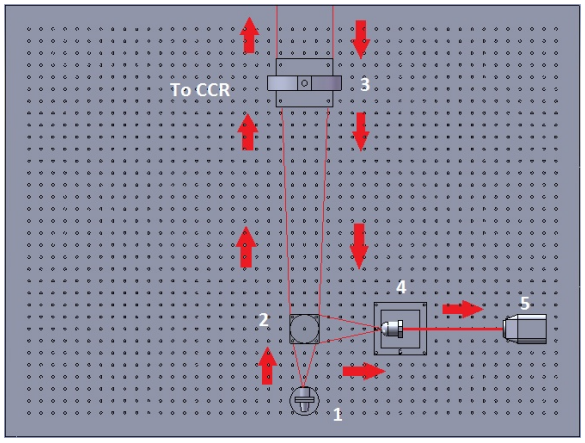

(b) Optical Scheme

Figure 3.10: Optical table, definitive configuration: 1. FO Laser 2. Beam Splitter 3. Lens 4. Enlarger 5. Camera

3.3 Alignment Procedure

The laser beam is defined aligned when the laser optical path, which hits the CCR, superimposes on that getting back to the source through the beam splitter and the altitude remains constant for all the optical path. So the laser beam has to remain on a plane assumed as a reference: using this method all adjustments on the optical circuit can be made in 2D dimension. In this case the reference plane parallel to the optical bench is at 13 cm altitude.

In order to maintain the beam on this plane, is necessary that on every circuit component the ingoing and outgoing beam is at a constant altitude: so the reflection plane must be superimposed on the reference one. The beam must be aligned both to be able to define the optical axis and to realize the circuit equipped with all the optical devices, in particular with lenses and beam enlarger. In this case the most critical components, which need refined regulations - using micrometric regulators where possible - are lenses and microscope objective. Because of position of thermo-vacuum chamber is fixed, and it is also fixed the position of CCR, the beam splitter don't need fine regulation: it's just useful to pay attention at the shape of the outgoing beam, in order avoid any potential cut in the beam hitting the CCR. Lenses are not provided with micrometric regulator: this means that an accurate work of hand-positioning has to be done. Nevertheless the achromatic doublets, thanks to their shape, guarantee the absence of any geometric aberration if the mounting angle offset is included in few degrees tolerance, fixed by the data sheet of the lenses. Beam enlarger has micrometric regulations on the x and y axis: so the difficult operation consists, if the beam is aligned, in making coincident the focus of the second doublet with the entry lens of the objective. The alignment procedure could be summarized as follows:

1. Fix fiber optical laser on the mounting system, evaluating the height of the beam with respect to the optical table using a meter or a white board.

2. Position the first lens at the right focal distance in order to make the whole beam enter inside it: to evaluate the focal distance with precision lens has to be moved forwards and backwards along the optical axis and density of the beam has to be verified after each movement. If the lens

has been mounted correctly the outgoing beam will be collimated and with a diameter exactly equal to diameter of the lens.

3. The mirror has to be positioned right in front of the beam splitter: to have continuity in the optical path it is necessary to test with a target beam reflected before mounting the beam splitter.

4. The beam splitter will be mounted in the middle of the length between mirror and optical window of the chamber: it is necessary to verify that the outgoing beam is always collimated and has the correct shape from each reflecting face of the splitter using a target.

5. Position the second lens after the beam splitter paying attention as done with the first lens. A verification with a target is required in order to estimate the focal distance, that will be the mounting position of the beam enlarger.

6. The microscope objective has to me mounted with the entry lens coincident with the focus of the second doublets: if this condition is not verified distortion in outgoing beam can be seen on a target or on a white screen.

7. CCD camera has to be positioned in the focal plane of the microscope objective: because it is not simple to evaluate, it is better to verify directly the images on the camera. Focal distance has been reached if the pattern visualized results blind to small movements of the camera - along the optical axis.

Focusing operations performed on the definitive configuration have been completely changed from the previous procedure, thanks to the new slits and to the new layout of the bench. The steps can be resumed as follows:

- The beam outgoing from the laser and the reflected beam outgoing form the CCR have to be coincident: it means that the focus of the 800 mm lens has to coincide with a point on the surface of the fiber optical laser generator.

- The distance between the laser generator and the beam splitter and the surface of the beam enlarger and the beam splitter has to be the same, in order to respect the focal distance for the 800 mm lens.

- The focusing has to be realized only using the slit for the x movement for the beam enlarger and the y movement for the lens. All the other components has to be fixed to the optical bench.

- Great care has to be dedicated to the mounting system of the 800 mm lens: because the slit allow micrometric movements in translation only in x, y and z direction, the rotational movement around z axis. Lens has to be orthogonal to the optical axis, in order to avoid aberrations.

- Camera has to be positioned respecting the distance imposed by the magnification of the beam enlarger: magnification of the observed figure changes according to the distance between the camera and the microscope objective.

So it can be said that the incident beam has to be parallel to the CCR longitudinal axis, and the image on the camera's CCD has to correspond to the focus. The first goal is considered achieved is if the image in the camera is stable even if CCR is moved. The second goal is achieved only if the pattern from a plane mirror is a well defined airy disc. All the procedure applied to align the circuit count a "try & error" method: some of the steps

has been repeated a great number of times in order to reach the best results as possible.

Chapter 4

Experiments on CCR

This chapter will provide a plain view of the objects tested in simulated space environment and of the test realized on them. The description of the breadboard tested will be given with particular references to their realization and cleanness to achieve the test conditions. A summary of the procedures designed and followed for the good realization of the tests will be reported and explained: in some most of the cases these procedures has been realized following the ECSS normative. Where scheduled the procedure of fixing sensors or heaters will be reported.

4.1 Devices

The unit under tests (UUT) is composed by:

1. Tungsten Cylinder;
2. A couple of plastic rings;
3. 3 M3 tungsten screws;
4. Retainer ring;

5. CCR.

The tungsten cylinder is made with a W-Ni-Cu alloy, the THA-18N, the same tungsten alloy employed for the flight model: this material has been chosen in order to have a satellite with low magnetic permeability and a low area/mass ratio. This guarantees that all the measurements on LARES will be poorly affected by the non-gravitational perturbation effects, in order to preserve the principal aims of the mission.

Figure 4.1: Breadboard: photo during final stage of cleanness

In particular the breadboard is also realized in order to allow the assembly of a single CCR using the mounting system qualified for the flight specs. The cylinder has also some hollows, and some of them are trough holes, in order to have a wide range of possibilities in using sensors for measuring temperature or other parameters of tungsten and CCR. The breadboard available are of 3 kinds, because of their dimensions – 4, 6 and 8 cm – and their different cleaning treatment, in order to better understand the thermal and optical

properties of the tungsten alloy in space environment. For all the breadboards the following cleaning operations have been performed:

- All breadboards and some of the screws and of the retainer rings have been bathed in aqueous solution of caustic soda at 10% in a thermal range from 60°C to 80°C for 1 hour and 20 minutes;
- Then they have been rinsed out with distilled water and then with running water for about 5 minutes;
- Then they have been bathed in aqueous solution of hydrochloric acid at 18% at room temperature for about 10 minutes;
- All breadboards have been rinsed out as in point 2;
- Then have been bathed in a ultrasonic basin with water and basic cleaner at 5% at 40°C for 5 minutes;
- After have been rinsed out with running water and then drizzled with ethyl alcohol;
- The breadboards has been putted in forced ventilation for drying out with air at 70°C.

The 6 cm breadboard has been then putted in autoclave at 500°C for another degassing process: it has been kept in this conditions for about 6 hours. Vacuum level was in a range from $10^{-4}mbar$ up to $10^{-6}mbar$. The 8 cm breadboard has undergone other washing treatments because of some spots near to the holes for the sensors: the ultrasonic washing and the basic cleaner treatment have been repeated. It has been rinsed out with current water. Ultimately another ultrasonic washing with ethyl alcohol has been performed: it has been kept in the basin for 15 minutes at 40°C. However

Figure 4.2: Various stages during cleanness process

this breadboard has shown the spots even after this new washing treatments: probably the spots must to be ascribed to the mechanical manufacturing of the breadboard. At last all breadboards have been put in some vacuum sealed envelope, opened only few minutes before the tests started. In the envelope a retainer ring, a couple of plastic rings and 3 screws have been put in order to be associated to the breadboard inside. The plastic rings are made of VOLTALEF, a plastic material for space purpose, because it has high thermal resistance and it is not affected by degassing effects. CCR is realized with *Suprasil*, that is a quality of fused silica: all the specs on this material can be deduced from the manufacturer data sheet.

4.2 Test

The tests executed on the breadboard an on the CCRs mounted on them can be resumed in three groups: mechanical, thermal and optical group. All the tests performed to check the structural strength of CCRs assembled with

flight specs can be included in the first group. The second and third group are composed by the test performed to better qualify the devices in space environment.

4.2.1 Cleanness test

The cleanness tests was made to better understand in which way the processes on tungsten breadboard shall affect the CCR surfaces. The aim of the test was to select an adequate cleanness process that should be applied to the LARES satellite tungsten alloy. The adequate process has been selected by testing breadboards representing the CCR assembly on LARES satellite. Each breadboard has been manufactured using the same batch material used for LARES body and each one has been cleaned in a different way, as discussed in the previous section. A CCR has been mounted on the assembly. The breadboard carrying the CCR has been put in the thermo-vacuum chamber to simulate the environmental condition in space. After being exposed to thermo-vacuum environment, the breadboard has been visually inspected to verify if any contaminant has been deposited on the back faces of the CCR. The cleaning process that have leaved no visible contaminants on the CCR back faces has been considered adequate to be used for LARES. Only the 4 mm and the 6 mm breadboards have been employed for these tests: the 8 mm has been not tested because of the spots visible on its surface. The CCR mounted on the breadboard was a spare unit in order to avoid the contamination of the flight units. The CCR has been cleaned with isopropyl alcohol before the mounting inside the breadboard. According to ZEISS, acetone can be used too. Lint free optical wipers has been used (Kimtech Science 7552 wipers). The test has been performed as follows:

1. The vacuum bag containing the UUT tungsten parts must be opened

before performing the test.

2. The CCR shall be cleaned with isopropyl alcohol or acetone.
3. An accurate visual inspection of the CCR surfaces must be performed.
4. The breadboard shall be assembled by following the flight specs.
5. PT100 sensors and resistive heaters shall be installed on the breadboard.
6. Breadboard shall be placed on the holder inside the TVC and faced to the shroud.
7. Data recording from sensors starts.
8. The unit shall be maintained at $P = 10^{-5}$ mbar for 24 hours.
9. After 24 hours the heaters shall be switched on and breadboard shall reach 90°C steadily.
10. The shroud shall be cooled by the Liquid Nitrogen System.
11. The system shall remain in this configuration for 16-24 hours.
12. The venting valve of TVC shall be opened and operators shall wait until temperature on the breadboard reaches safe temperature for handling and temperature on the shroud reaches safe temperature to avoid condensation of water vapor present in atmosphere.
13. Data recording shall be stopped.
14. TVC shall be opened and breadboard shall be removed from the holder.

15. The CCR shall be removed from UUT, taking care to avoid touching the rear surfaces of the CCR.

16. An accurate visual inspection of the CCR is performed, to verify if there are contaminants deposited on the glass.

Even if in both cases very few contaminants has been noticed on the surfaces of CCR, the breadboard with only chemical cleanness treatment has been considered compliant to the test success criteria.

4.2.2 Mechanical Tests

All the mechanical tests aim to evaluate the possible variations that the assembly of the containing system could introduce on CCRs. In most cases structural analysis is performed also during the thermal tests because of the coupling of the effects. Some of the tests have been made for the screws and the torque to impress on them for a good assembly: in flight specs a 0.8 Nm up to 1 Nm torque for each screw must be impressed. During the tests a range of torque has been selected and for every step the movement of CCR inside the mounting system has been checked. The tests were been performed as follows:

1. The breadboard shall be disposed in vertical position and on a stiff backing to avoid movements during the assembly operations;

2. Mounting system shall be inserted in the breadboard following the flight specs;

3. Screws shall be inserted in the dedicated seats, sliding them until resting at full-travel stop;

4. With a torque wrench, screws shall be tighten until the defined torque is reached;

5. A FFDP of the prism is taken, referring to the impressed torque.

6. With fingers (covered with gloves), or with a rubber stick the movements of CCR inside the mounting system must be verified;

7. If CCR movements are allowed inside its seat is possible to continue the test with a higher torque level;

8. If CCR movements are not allowed inside its seat the tests end.

Impressing different levels of torque it noticed that in some cases – all the tests were been performed using different couples of plastic rings and different breadboard – the movements of CCR was not allowed. The aim of the test is to investigate the possible mechanical deformations introduced by a wrong mounting procedure: obviously deformations that may affect plastic rings are directly transferred to the CCRs mounted inside the breadboards, and this could create some changes in shape or energy distribution of FFDP.

4.2.3 Thermal Tests

Thermal tests are needed in order to better understand the behavior of LARES satellite exposed to the thermal loads when it is on orbit. From other papers some informations are given on the thermal response of CCRs in a range from -70°C up to 22°C (RIFERIMENTO): the aim of these tests is to extend the range of data up to a higher temperature. Obviously the imposed thermal load can be considered remarkable only for CCRs: with the devices employed during the tests the maximum temperature reached has been of about 160°C, that is negligible to understand the behavior of

tungsten breadboard. The thermal tests must be considered strictly linked to the mechanical ones because of all the possible deformations that the high temperature could introduce in the whole system. To follow the variations of temperature on the unit under test or on the CCR, RTD (Resistive thermal devices) sensors were employed: among all the available temperature sensors these have been considered the most suitable for the purpose, thanks to their accuracy, low drift in measurements and their suitability for precision applications, as explained in the previous chapters. Thermal tests can be divided in two parts: some of them have been realized employing some heaters to warm up the unit under test up to the desired temperature, in some others the sun simulator has been employed to achieve informations about the reachable temperature in sun exposition. In the tests with heaters was possible to regulate the temperature using a power supply in order to command the heaters, while in the tests with the sun simulator there was no kind of regulations, so it was necessary to wait until the breadboard reached the steady state temperature. For the general thermal tests there is no specific procedure: probably the most difficult operations are to realize a good gluing of the sensor on breadboard or CCR and in order to do this as well some technical solutions shall be considered. The position of the sensors can be decided on the particular test to be realized. Only for CCR, the sensors must be glued in specific position to measure the axial thermal gradient between the front face and the tip of the device. Sensors are small enough to allow a not invasive positioning on the whole system, so for the gluing they need few pieces of adhesive tape. However a good gluing must take into account also the possibility to insulate the sensor from the external environment in order to be glued only on the surface on which the sensor is mounted. For the gluing operations some kind of adhesive or bi-adhesive tape has been

employed: the contact between sensors and the mounting surfaces is realized using a special bi-adhesive tape composed by an adhesive matrix in which are placed some little metallic thread in order to better transfer the heat of the surface to the sensor. The insulation process can be realized using some sheet of adhesive kapton or teflon. The insulation from the light of the sun simulator can be realized with reflective tape. All the tapes employed for the purpose and the enclosure of the sensors aren't affected by degassing event in thermo-vacuum environment.

4.2.4 Optical Tests

Any kind of optical test realized can be considered as a proof of the good operations of CCR under thermal or mechanical load. As discussed before the *Far Field Diffraction Pattern* is the response of CCRs hit by a laser beam: all the changes – whit respect to a reference FFDP – in this response could be considered as a signal of changes directly on the CCRs. So all the optical tests can be considered as a part of another test, both thermal and mechanical: all the deformations introduced in the whole system because of a thermal or a mechanical effect can be noticed analyzing the FFDP. All the recommendations on this kind of tests are linked to the set up of the optical bench before any thermo-vacuum test: it means that calibration and alignment, both horizontal and vertical, of the optical bench must be checked before to start any test. A more complete procedure is explained in the previous chapters. The only parameters that can be modified during the acquisition of a FFDP are the laser power and the setting of the camera: so during the tests several FFDP at different laser power have been taken, and for each laser power some of the settings of the camera has been changed (like ISO or Exposition). So in the tests performed following these few points a very

large number of FFDP has been taken: so far more than 1000 FFDP have been recorded and analyzed with the image processing software described in the next chapters.

Chapter 5

Software

In this chapter all the software designed and realized to analyze the FFDP are explained: all the patterns taken from the tests in thermo-vacuum chamber have been processed using a software created in MatLab environment. The analysis treatment is needed in order to better notice all the variations in the patterns, from the microscopic to the macroscopic ones. Obviously the software has been developed following the results coming from the configurations of the optical bench: because of all the continuous re-arrangements of the optical bench, several versions of the software have been developed. Each version give some results in order to better analyze the patterns obtained from the configuration of optical bench in use, focusing on all the defects coming from a wrong setting of optical components. With Simulink a software for video treatment has been developed: it provides to simply geometrical analysis to detect small changes in the FFDPs. With MatLab software a more complex image treatment has been developed: as shown in the next chapter, the software is able to perform simple procedures of feature extraction and pattern detection and it is able to perform both qualitative and quantitative analysis.

5.1 Video treatment

With the first configurations of optical bench, the aim of some tests was to take some small video in order to better understand in real time the changes occurred on the FFDP when CCR was under test condition. The following video treatment process has been implemented to analyze the videos and to perform some first approximation quantitative analysis, so that the frames in which the changes occurred could be selected and re-analyzed after. The Simulink program shown in the next section was also developed to face some of the errors coming from the faulty configuration of the optical table, in order to steady the movements of the FFDP or the changes in shape.

5.1.1 Patterns Acquisition

With the early configurations of optical bench the patterns were acquired using a night vision camera: to transfer the images on a computer an USB decoder has been used. It allow a link between a computer and a camera with PAL way out. So all the video taken during the first experiments are in PAL format (analog video output, 625 line/25 frame per second). The image acquired are in bitmap format, in order to have images of good quality. Resolution can be changed using the acquisition software: to preserve the quality of images the highest resolution has been selected: so it has been imposed at 720×576. the software used for image acquisition was *Ulead VideoStudio SE DVD*, that come with the USB decoder. In the last configuration of the optical bench the night vision camera has been replaced with a reflex camera *Canon EOS 1100D*. With this device the resolution has been increased up to 3888×2592, obtaining images better than in the previous case. The image coming from the camera was in *JPEG* format. In both cases some

diaphragms able to reduce the external light sources has been used.

5.1.2 Image Loading

In all software versions both images and videos have been processed. In both cases the files have been loaded using a procedure that allow to import files in a great number of formats. With this block is possible to change some parameters of the imported file: often both images and videos have been processed separating the color signal (that is *RGB*) and using only a channel for the analysis. This process is useful in the case of patterns realized using a monochromatic light source (like the He-Ne laser or the fiber optical laser): isolating only the channel of interest it is possible to reduce the noise introduced from the external light sources. In some cases of the analysis the creation of a video using some acquired patterns was needed: in this case a freeware software for video creation has been employed to realize an *.avi* video using *.bmp* images.

5.1.3 Filters and Image detection

One of the problems faced has been the image cropping in the zone of interest: in a high resolution photo, FFDP take up only a small region, while the remaining part is composed by almost black pixels. So to apply all the image analysis processes is necessary to crop the whole pattern and take only an amount of pixels corresponding to the FFDP. This operation is simple to be executed: in Simulink environment a *Selector* block is used. This block allow to select only a part of a matrix excluding all the rows and columns not selected. The selection can be performed using as a starting point an index for row and column a whole row/column. This operation can be done also off-line – that is before to load the image in the MatLab software – using other

common softwares for image and photo treatment. As discussed before most of patterns have been taken into an environment not made for good quality photos and the devices employed for the patterns acquisitions were not always high quality optics compliant: several patterns has been taken with lights on and also common webcam was used for patterns acquisitions. All this conditions have introduced some noise into the FFDP taken, especially in the first experiences, that is when CANON 1100D was not available. To compensate these effects several kind of filters have been applied in the image analysis process: some of them was available directly from Simulink blockset, some other have been built up using simple operations. The following filters has been tested during the analysis process:

- *Edge Detection*: this filter has been employed most of all for the selection of the region of interest in the whole image. Because of his properties it was also useful to filter the noise affecting the pattern. It works with different type of kernel algorithm (that is Sobel, Prewitt, or Canny): the block outputs two gradient components of the image, which are the result of a convolution operation. Alternatively, the block can perform a thresholding operation on the gradient magnitudes and provides a binary image, which is a matrix of Boolean values. If a pixel value is 1, it is an edge. With Canny method the block finds edges by looking for the local maxima of the gradient of the input image. It calculates the gradient using the derivative of the Gaussian filter. The Canny method uses two thresholds to detect strong and weak edges. It includes the weak edges in the output only if they are connected to strong edges. As a result, the method is more robust to noise, and more likely to detect true weak edges. and outputs a binary image where the pixels with value 1 correspond to the edges. It is possible to reduce

or increase the capacity of detection varying a parameter (dept of the filter) [2].

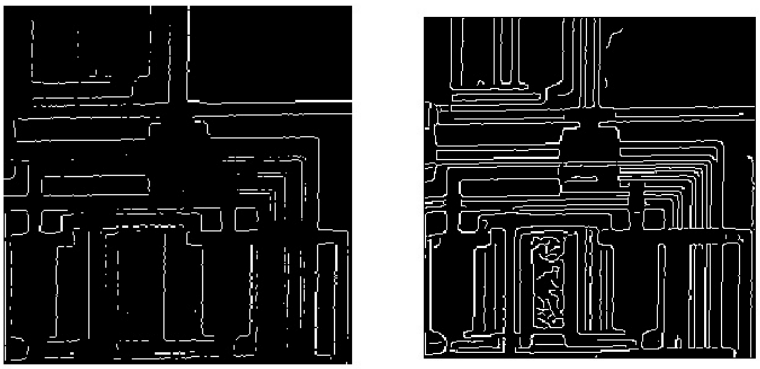

(a) Prewitt Method (b) Canny Method

Figure 5.1: Edge Detection Block: Prewitt and Canny methods

- *Contrast Adjustment*: this filter adjust the contrast of an image by linearly scaling the pixels color intensity value - operation done in each color channel of the frame - between upper and lower limit. All the pixels with value over the upper limit or under the lower limit can be saturated or reduced to zero. For this filter a careful selection of the limits has to be performed in order to not vary the values of the pixels in the region of interest. Using a simple graph the filter works as shown below:

  The references of the filter - that is maximum and minimum value on which the filter operates - can be selected in the same image (Full Range: automatic) or imposed in an input vector.

- *Median Filter*: it performs a median filtering of the input image: the block replaces the central value of a selected sub-matrix with its median

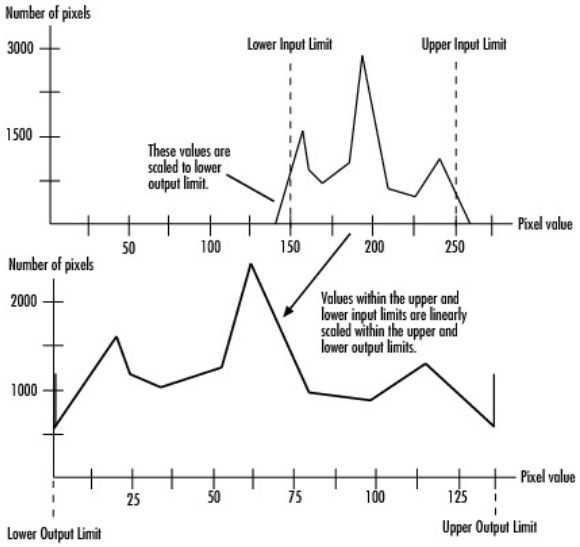

Figure 5.2: Contrast Adjustment: logical operation

value. If the matrix has a center element, the block places the median value just in the middle. The filter can be settled in different ways by changing the options in its dialog box: sub-matrix dimensions can be easily settled up, like the output dimensions or the padding factor. With this last options the value of the center of the sub-matrix can be extended all around the center.

In order to reduce the computational time – the operations of filtering notably slow down the routines – another kind of filter has been realized, simply using the math functions of the MatLab Toolboxes: with the selector block a single row or column or a small matrix, far from the region of interest, has been cropped. Using the block *Mean*, the mean value of the selection is performed: this value can be considered as the background noise. Subtracting this value from the whole image, before performing any kind of analysis, reduce notably the external noise, even if it is still present. This kind of

procedure is also called *Black Pixel Analysis*: usually is performed taking a black image from the same optical circuit employed for the FFDP and all the future operations of filtering – that is noise mean value, or any other kind of filtering operation – comes from the analysis of this black photo. In this case a kind of black pixels analysis is applied in real time on each of patterns analyzed.

5.1.4 Pattern Recognition Subsystem

As discussed at the beginning of the chapter, in some cases the FFDP taken has been edited in a video: the first patterns taken were very sensible to movements, as discussed in the previous chapters. In order to compensate the variations and the movements introduced in the acquisition process a subsystem for pattern following was needed. This process aims to recognize and crop the region of interest in the whole pattern, also using the filters discussed above: these operations are performed during the whole length of the video, and the recognition/following operations are applied in every frame. The subsystem has been built as follow: after all the operations of filtering and noise reduction the video become the input of the subsystem for pattern following. Then the first frame of the video is sampled and become the reference for all the following operations. The operations of sampling are performed by the SImulink block *Sample and Hold*, operated by a *Pulse Generator* in order to set the sampling period. This means that the reference changes during the play of the video: this operation must be done in order to make the subsystem follow the FFDP even if it changes. If patterns changes while reference remains the first frame, the operations of recognisance and tracking could be compromised if the variations in the pattern during the video are strong enough. To reduce the computational

time it is useful to introduce in the logical chain a selector to better focus the reference and improve the recognisance process: the better is defined the reference, the better the software will target the region of interest. The recognisance process is performed by a *2D Correlation* block: it makes a cross-correlation in two dimensions – so on rows and columns of the input matrix – in order to find the maximum similarity between the processed frame and the reference. Mathematically the block works applying the following law: if the processed images are A and B, the first with dimension (Ma,Na) and the second (Mb,Nb), the 2-D correlation will be:

$$C(i,j) = \sum_{m=0}^{Ma-1} \sum_{n=0}^{Na-1} A(m,n) \cdot conj(B(m+i, n+j)) \tag{5.1}$$

where $0 \leq i < Ma + Mb - 1$ and $0 \leq j < Na + Nb - 1$.

Practically the block works with some simple rules: let's take two matrix I1 of dimensions 5×5 and I2 of dimensions 3×3. The correlation operation will be made as following:

1. Slide the center element of I2 so that lies on top of the (1,3) element of I1;
2. Multiply each weight in I2 by the element of I1 underneath;
3. Sum the individual products from step 2.

This block can be settled to make the operations of cross-correlation on the whole pattern, so that the recognisance algorithm can focus the region of interest wherever it may be. The settings can be chosen among three options: *Full*, *Same as Input Port*, *Valid* and each option is referred to the dimension of output matrix. Moreover the output values can be normalized using another option. The output matrix is then processed in a *Maximum* block, that

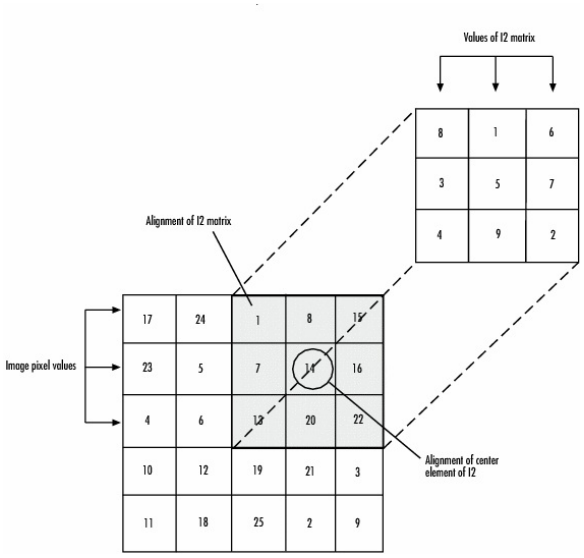

Figure 5.3: 2DCorr: logical operation

outputs the index of the maximum value in the matrix of correlation. In this way is possible to focus the sub-matrix of the pattern that have the maximum similarity with the pattern: the index from *Maximum* block become the center of a figure that enclose the region of interest, drawn with the *Draw Shapes* block. It is possible to change the shape of the boundary figure setting the block with different options: among all these, it is possible to increase or decrease the area of the shape drawn, that corresponds to the region of interest. After this process is possible to crop the only region of interest simply subtracting the processed pattern from the original pattern.

5.1.5 Pattern Analysis Subsystems

Several kind of analysis has been performed on the FFDP: in some cases, some of the analysis have been run using directly some blocks from Simulink. Obviously some analysis on pixels light intensity have been performed: us-

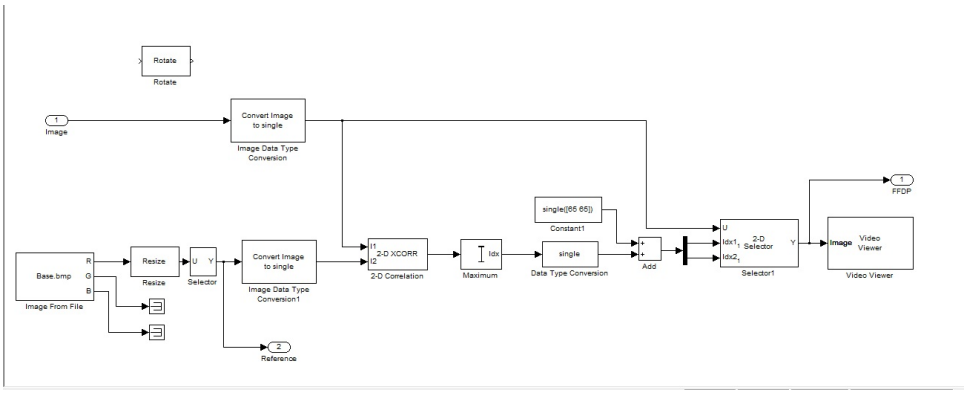

Figure 5.4: Image detection subsystem

ing simply a *Sum* block, pixels intensity of the region of interest has been compared to the pixels intensity of the whole pattern, in order to better comprehend the weight of the noise on the frame, and to see if the light from the laser was totally included in the FFDP. Other simple visualizations - that is, for example, FFDP with new color scales or images processing in binary forms - can be realized using blocks like *Matrix Viewer*. With this process is possible to recognize at first sight where are the maximum peak of light intensity in the FFDP. To improve the analysis processes, other subsystems has been realized: because some of the main guidelines of the FFDP were known other kind of analysis has been performed in order to verify all these specs. For example, in case of CCR with dihedral angle, to understand if FFDP has few light in the central part, the middle row or the middle column of the region of interest have been analyzed: by using plot of the pixels intensity is possible to see if light is more focused in the external lobes than in the center. To perform this process a *Vector Scope* block has been applied. The same simple principles have been employed to process the patterns changes during the thermal tests: a row, a column or also a sub-matrix of the whole pattern

can be used to check any change in respect with the patterns taken when the CCR was not thermally tested. In order to have some results a dedicated subsystem has been created: it operates three "geometrical" analysis, on the middle row, on the middle column and on some sub-matrix – called in the subsystem *Mega-pixels*. The analysis is performed as following: a reference FFDP is fixed – that is the same reference employed for the pattern recognition subsystem – and on this pattern the middle row, the middle column and the mega-pixels are extracted. The same operations are performed, on every frame, on the video of the FFDP running, or on a new image of FFDP taken during a thermal test. In every element (row, column and mega-pixel) a sum to calculate the total light intensity is performed: comparing this sum with the results coming from the reference is possible to fix an "index" in order to simply test the possible changes in the FFDP. To check this analysis method some tests have been performed: using a calculated FFDP, a short video has been edited, rotating or shifting the pattern of a defined step in order to see the changes in the indexes. From this tests it derives that the analysis on row or column is a good flag to check possible rotation of the FFDP – a variation of ± 2 in the indexes of row/column analysis corresponds to a 1° rotation –, while the more wide analysis on mega-pixels is useful to check the variation of light intensity in a more precise way then using a simple visualization. This subsystem is connected on the pattern recognisance subsystem: if the algorithm of image following is correctly working all the shifting in the pattern will be compensated. This "follow-up" system could disguise potential changes in patterns caused by a deformation of CCR that make the FFDP shift: thanks to a little delay in the reconnaissance, and associating this process to the results of other analysis it is possible to notice the translational movement of the pattern in the charts produced at the end

of each run.

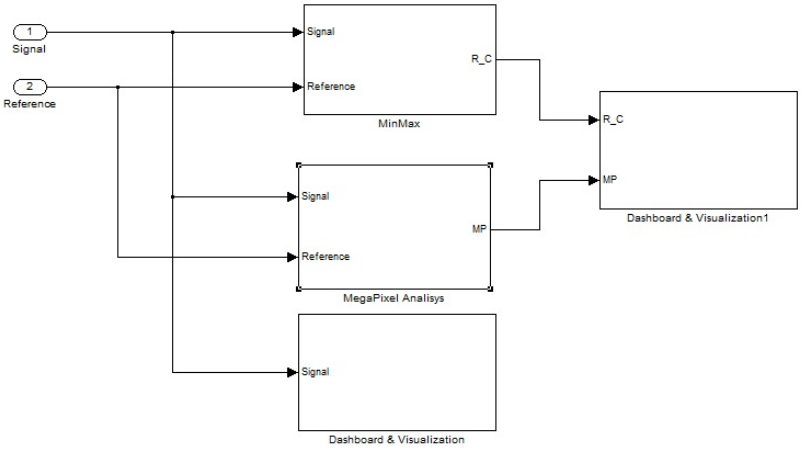

(a) Analysis Subsystems

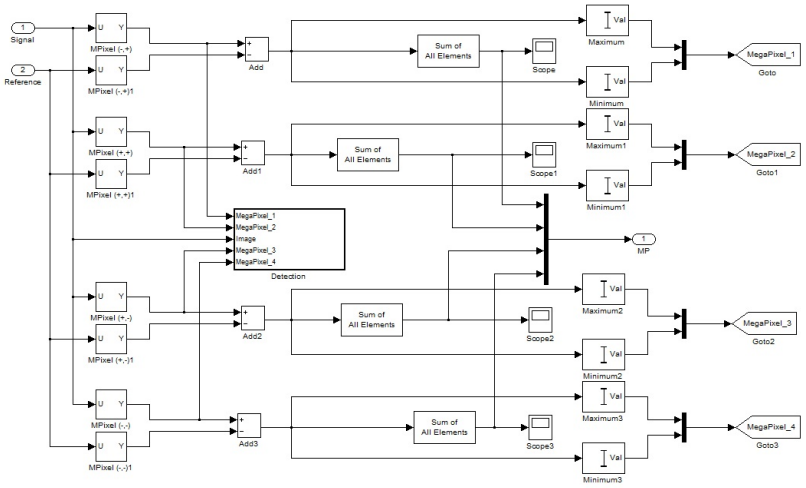

(b) Megapixel Analysis

Figure 5.5: Image Analysis subsystems

5.2 Image treatment

With the last configuration of optical bench the idea to take real time video has been given up. Because of the great stability of the patterns and the new camera suppressing most of the noise affecting the patterns, only photos has been taken: hence, some photos during tests development have been taken and analyzed later with much more care than in the case of the videos.

5.2.1 Comparison between theoretical and observed images

To have some references and to better understand if the software produced works well, some comparison between theoretical and observed FFDP has been realized. The theoretical patterns have been provided by Dr. Reinhart Neubert and created using *Diffract01*, a program realized by Dr. David Arnold, in his ownership with regular license. All the observed patterns have been taken in *GFZ - GeoForschungsZentrum* laboratories in Potsdam in June/July 2011. In the following pages the software will be shown with particular references to the MatLab functions employed, taken from *Image Processing Toolbox* and *Signal Processing Toolbox*. The aim of the software is to perform a complete comparison between theoretical and observed images in order to give some quality factor, to better understand if images taken in laboratory are significant. The image is loaded into MatLab and it is ready to be processed. Then the maximum value of the matrix is calculated using two times the function "*max*". In this case the image in "*.bmp*" has two dimensions and so the repetition of function "*max*" is necessary to have the absolute maximum of the matrix. With function "*im2single*" the image is converted into a matrix of single (unit8) values: the function converts

the values into unsigned 8-bit integers. The elements of an uint8 variable have a range from 0 to 255. After the calculation of the dimension of the image the middle row is selected, and a vector of values to create the x-axis is implemented: obviously the x axis will go from 1 up to the length of the middle row of the image. Then, after a definition of the values that characterize the double slit screen and the optical bench (that is spacing, depth and height of the slit, wavelength of the laser beam) the theoretical curve is calculated, using the following formula:

$$T = \left[\cos\left(\pi\frac{d}{\lambda}\alpha\right)\right]^2 \cdot \left[\frac{\sin\left(\pi\frac{a}{\lambda}\alpha\right)}{\left(\pi\frac{a}{\lambda}\alpha\right)}\right]^2 \tag{5.2}$$

where$d$ and a are respectively the spacing between the slits and their thickness, λ is the wavelength of the laser and α is a geometrical coefficient in which are present both a conversion factor to reduce pixels in microradians and a coefficient that centers the theoretical curve on the observed one. To have the best matching between theoretical and observed curve a range of values id defined: the coefficient that maximize the convolution between the two curves will be considered as the optimum value to use into the formulas of unity measurements conversion. Hence, in the program there is a comparison between the observed curve and all the theoretical ones, each of them calculated for the specific value of the coefficient. Obviously some operations are needed in order to have the best possible match like the change of measurement unit from pixels to microradians or the shifting of the center of the theoretical curve in the center of the observed one. At the end of the cycle, so when the optimum coefficient has been found, there is an operation of scaling in order to have both the curves with the same amplitude. The scaling factor is simply the ratio between the maximum values of the observed curve and of the theoretical one. To have the best matching of the curves

(and also for the next analysis process) the calibration curves are convoluted using the function from MatLab "*conv2*": the command computes the two-dimensional convolution of two matrices A and B. The size of the output in each dimension is equal to the sum of the corresponding dimensions of the input matrices, minus one. "*conv2*" uses a straightforward formal implementation of the two-dimensional convolution equation in spatial form. If a and b are functions of two discrete variables, n_1 and n_2, then the formula for the two-dimensional convolution of a and b is [1]:

$$Out(n_1, n_2) = \sum_{k_1=-\infty}^{\infty} \sum_{k_2=-\infty}^{\infty} a(k_1, k_2) b(n_1 - k_1, n_2 - k_2) \tag{5.3}$$

In the declaration of the function "*conv2*" it is possible to select also a part of the output computed specifying a *shape* parameter: using the shape "*'same'*" the output will return the central part of the convolution of the same size as the first matrix computed in the function. So the operation of convolution is executed on the correspondent rows and columns of the two vectors of the observed and theoretical measurements. The second part of the program allows to make a direct comparison between a theoretical FFDP and an observed one. First of all a conversion from microradians to pixels is needed: in this case the conversion has been applied to the theoretical image, expressed in microradians, using the coefficient of maximum convolution calculated before. Obviously it would be possible realize the inverse operation on the observed FFDP. All the images analyzed are in *.jpg* format, so that are considered as 3-D matrix: the 3rd dimension corresponds to the RGB color channels. This means that for our purposes is necessary to use only the channel that corresponds to the laser wavelength. After the selection of the channel a normalization procedure is applied: the observed image is transformed into a purely mathematical matrix (in this way each

pixels is not limited to 255). Then it is multiplied by 255 (saturation value of the color channel) and divided for the maximum value of the matrix of the "mathematical image". This process is applied only to the observed image because the theoretical one is considered already normalized. After that image is transformed into a simple grayscale image (pixels value are from 0 to 1).

Then a simple routine for image matching has been implemented: input image is converted into a binary image. The output image replaces all pixels in the input image with luminance greater than a specific threshold with the value 1 (white) and replaces all other pixels with the value 0 (black). The MatLab function that allow to realize this process works only with grayscale images: if the input image is not a grayscale one, the function converts the input image to grayscale, and then converts this grayscale image to binary by thresholding. When threshold is not specified the function filters the image on a mean value. In this way image will have white pixels only where highest values of pixels are present [1].

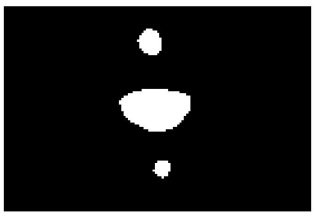

Figure 5.6: *im2bw* function effect on the image

This assure that the whole image is completely black and only the useful pixels (that are the ones corresponding to the FFDP) are white colored. To detect where the image has white pixels (that is to locate the "skeleton" of the FFDP) a sum process along row and column is performed, and then indexes

of non-zero element of the sum are calculated. Because of the theoretical images are square matrix of 101×101 pixels, the aim of this routine is also to select the FFDP enclosed into a box with the same dimensions of the reference. To have a square selection a simple equation could be written: working with BW image, suppose that X and Y are the pixels that has to be cropped from the whole image on x-axis and y-axis, and suppose that A and B are the indexes of the first and last useful column, like in the figure:

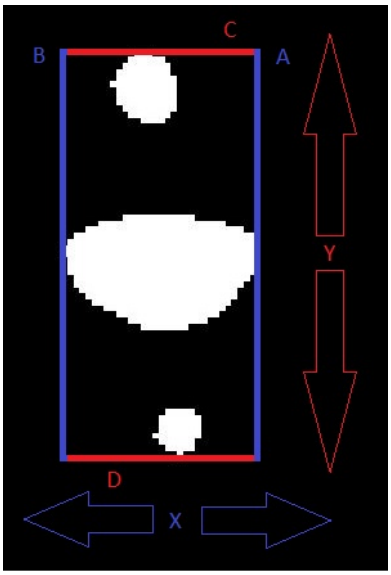

Figure 5.7: BW image: red and blue lines represent frist/last useful row/column

If the image has to have the same dimensions of the theoretical one (that is the vector *Scale*) the equations to calculate X and Y will be:

$$Scale(Row) = (B + X) - (A - X) \tag{5.4}$$

$$X = \frac{Scale(Row) - B + A}{2} \tag{5.5}$$

$$Scale(Column) = (D + X) - (C - X) \tag{5.6}$$

$$Y = \frac{Scale(Column) - D + C}{2} \tag{5.7}$$

These equations must to be used in all cases: if the reference matrix is square X and Y will have the same value, if the reference matrix is rectangular X and Y will have different values. When these coefficient are known the matrix can be cropped. Because the reference matrix has inverted values on pixels, the cropped image has to be inverted too: so the complementary image of the cropped FFDP will be created. To have the observed image of the same dimensions of the reference a resizing must to be applied, referring always to the dimensions of the theoretical image. Then some analysis for the quality of the image are provided: the formulas implemented for the image processing are [1], [3]:

Mean Square Error	$MSE = \frac{1}{MN} \sum_{j=1}^{M} \sum_{k=1}^{N} \left(x_{j,k} - x'_{j,k}\right)^2$
Peak Signal to Noise Ratio	$PSNR = 10 \log \frac{(2^n-1)^2}{MSE} = 10 \log \frac{255^2}{MSE}$
Normalized Cross-Correlation	$NK = \sum_{j=1}^{M} \sum_{k=1}^{N} x_{j,k} \cdot x'_{j,k} \Big/ \sum_{j=1}^{M} \sum_{k=1}^{N} x_{j,k}^2$
Average Difference	$AD = \sum_{j=1}^{M} \sum_{k=1}^{N} \left(x_{j,k} - x'_{j,k}\right) \Big/ MN$
Structural Content	$SC = \sum_{j=1}^{M} \sum_{k=1}^{N} {x_{j,k}}^2 \Big/ \sum_{j=1}^{M} \sum_{k=1}^{N} {x'_{j,k}}^2$
Maximum Difference	$MD = Max\left(\left\|x_{j,k} - x'_{j,k}\right\|\right)$
Laplacian Mean Square Error	$LMSE = \sum_{j=1}^{M} \sum_{k=1}^{N} \left[O\left(x_{j,k}\right) - O\left(x'_{j,k}\right)\right] \Big/ \sum_{j=1}^{M} \sum_{k=1}^{N} \left[O\left(x_{j,k}\right)\right]^2$ $O\left(x_{j,k}\right) = x_{j+1,k} + x_{j-1,k} + x_{j,k+1} + x_{j,k-1} - 4x_{j,k}$
Normalized Absolute Error	$NAE = \sum_{j=1}^{M} \sum_{k=1}^{N} \left\|x_{j,k} - x'_{j,k}\right\| \Big/ \sum_{j=1}^{M} \sum_{k=1}^{N} \left\|x_{j,k}\right\|$

Figure 5.8: Formulas for quality image analysis

All the formulas have been used for the analysis: the mean square error has been transformed in root mean square error, expressed in percentage and normalized on the maximum value of the theoretical image. The variable employed for the calculation is the error obtained by subtracting the reference

image and the observed one. It is the main parameter used for calculation of the quality indexes. All the parameters are calculated in pure numerical format. All these functions allow to plot the results obtained from the previous calculations: the figures in the next chapters will show the theoretical image and the observed one, the histogram plot of the two images (that show the number of the pixels having the same value), a comparison between the contour plot of the two images (useful to better understand if there are some differences in the shape of the FFDP) and a table in which are shown all the quality indexes calculated before.

5.2.2 Comparison between observed images and annulus analysis

As for the previous software discussed above, the computation of the comparison between FFDP images taken in Rome has been performed using *MatLab* and some of its toolboxes, like *Image Processing Toolbox* and *Signal Processing Toolbox*.

5.2.3 Analysis of FFDP in different conditions

With the software produced it is possible to analyze in several possible ways the FFDP taken during thermo-vacuum tests. It has been realized using the software produced in the previous section, realizing some other improvements to enhance the analysis skill of the same software. To avoid any kind of repetition the parts of the software imported from the previous one will be not commented. The part for the calibration image analysis has been completely imported: obviously these operations allow to calculate the optimum coefficient so that it can be employed to calculate the conversions from

microradians to pixels or the other way round. Moreover this coefficient is indispensable for the future annulus analysis. Hence the conversion in microradians form pixels is needed, in order to uniform the reference measurement unit between the simulation and the real observations. Obviously it would be possible to realize the inverse operation on the observed FFDP, leaving the image as it is. Then the reference image is loaded and its dimensions are scaled using a selected number of pixels (in this case 100 x 100) and the coefficient is employed to search for the best fit between images. The dimension selected will define the size of the FFDP at the end of the process. It has to be noticed that only the red channel of the image is processed and a normalization process is performed, treating image simply as a matrix, in purely mathematical form. It has to be done in order to prevent the saturation of some pixels inside the image. Both "mathematical" images, after normalization, are transformed into grayscale image as explained for the previous software.

Then a double cycle of iterations for the calculation of the weighted centroid of the image is performed: it is necessary to operate in this way in order to realize a centering between the reference image and the one under test. The selection of the FFDP from the observed image is a process realized with no high precision: hence a more fine matching using the coincidence of the centers of the images is supplied. The formula for the weighted centroid is applied for 2-D input, so that it can be written in mathematical form as:

$$WC_x = \frac{\sum_{i=1}^{X}\sum_{j=1}^{Y} iA_{i,j}}{\sum_{i=1}^{X}\sum_{j=1}^{Y} A_{i,j}} \tag{5.8}$$

$$WC_y = \frac{\sum_{i=1}^{X}\sum_{j=1}^{Y} jA_{i,j}}{\sum_{i=1}^{X}\sum_{j=1}^{Y} A_{i,j}} \tag{5.9}$$

where X and Y are the X and Y dimensions of the input A and i and j are the indexes for the selection of the single element of A. So some operations to detect the dimensions and the sum of all the values are performed. When the centroid of the cropped image has been detected it is possible to apply a method very similar to the one discussed above to realize a second crop all around the region of interest. In this case the coefficient employed to set the crop is the one defined by another variable that has to be imposed by the user at the beginning of the software. In this way a second crop has been realized and the region of interest has been selected, avoiding all the possible background noise. Using the same method described above the weighted centroid of the FFDP – both reference and image under test – is performed. In this way images are ready to be analyzed in several possible ways. As discussed above the reason of the double crop has to be found in a solution to exclude the background noise from all the calculation using only mathematical operations, in order to avoid to use of any kind of filter. This part of the software allows to perform the annulus analysis. The commands above have been written to create a mask in order to see only the pixels of the image processed in the area of interest. To realize the annulus two circle must be created: giving a step for the calculation of trigonometrical functions, the circles are calculated with an incremental radius to make the annulus spread more and more, covering the whole image of the FFDP. Using the MatLab function "*roipoly*" the region between the inner circle and the outer circle is calculated: the two masks have the same dimensions of the FFDP cropped and are composed by a white circle on black background. Hence subtracting

the internal from the external only the annulus region remains in white, while the background is black. Finding the indexes of the white pixels and using that indexes on the FFDP image is possible to detect the pixels inside the annulus. Performing a sum of the pixels and normalizing on the area of the annulus, an acceptable value of the total energy inside of the annulus is obtained. This number will be used to estimate the total energy in the returning signal from the satellite detected by the laser ranging station. The radius of the annulus change inside the loop to simulate the effect of the velocity aberration on the ground signal.

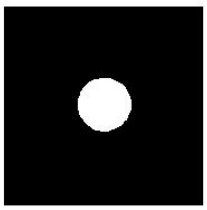

(a) Internal Mask

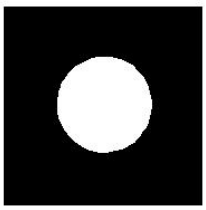

(b) External mask

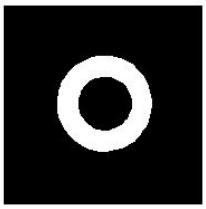

(c) Total Mask

Figure 5.9: Mask applied on the FFDP

5.2.4 Angular Scale calibration

Fixing the dimension of the annulus and performing some calculations on the calibration image mentioned above it is possible to pay particular attention to a specific part of the calculated values in order to match to the specifications coming from the mission of the satellite. Obviously the starting point of this process are the mathematical formulas of the double slit shown in the previous chapter: here will be shown a rough estimation for the calibration taken in Rome during the experiments on the LARES prisms. Let's consider the dimensions of the double slit screen: in this case the screen employed for the calibration test has slits of about 3 cm high and 0.3 mm large. The distance between the slits is about 33 mm. If the wavelength of the laser is well known it is possible to calculate the distance between two peaks of the pattern in μrad:

$$F = \frac{\lambda}{d} = \frac{635 \cdot 10^{-9} m}{33 \cdot 10^{-3} m} \simeq 1.92 \cdot 10^{-5} rad \simeq 19.2 \mu rad \tag{5.10}$$

The software shown above allow to have a measure of the distance between two peaks of the double slit curve in pixels: in this case the distance is about 26 pxs. So:

$$26 pxs \simeq 19.2 \mu rad \simeq 4 \cdot (5 \mu rad) \tag{5.11}$$

If is true that $1 arcsec \simeq 5 \mu rad$:

$$26 pxs \simeq 19.2 \mu rad \simeq 4 \cdot (5 \mu rad) \simeq 4 arcsec \tag{5.12}$$

And so:

$$1 arcsec \simeq 7 pxs \tag{5.13}$$

In this way the relation between arcsec, μrad and pixels has been found. In few words now it is possible to know how many pixels are "visible" under an angle of 1 arcsec. Moreover, for LARES the velocity aberration is included in the range $30 \div 50 \mu rad$. So the annulus in pixels can be computed as follows:

$$Range : \frac{30}{19.2} \cdot 26 \div \frac{50}{19.2} \cdot 26 \simeq 41 \div 68 pxs \tag{5.14}$$

Because in the whole program all the operations has been performed using the image as matrix in mathematical form that can't be visualized a new image called "*Visual()*" is created subtracting the FFDP and the realized mask. Then a GUI interface is created in order to show in real time the spreading of the annulus on the image. The graph represented are the values of the total energy inside the annulus plotted on the microradians. The last graph is the ratio between the two curves above in order to detect any change in the FFDP.

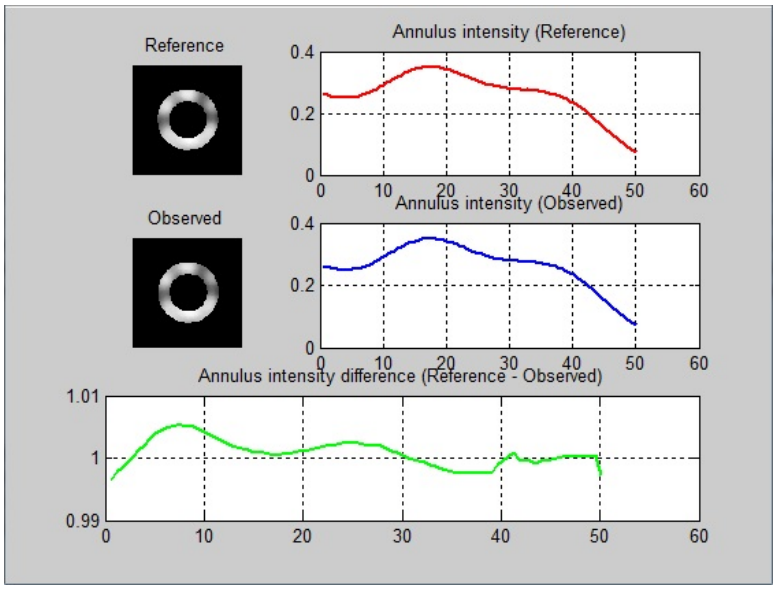

Figure 5.10: GUI Panel: screen-shot taken during running

The formulas employed for qualitative and quantitative analysis are the same as above, but a calculation of distance between the weighted centroids of the FFDP has been added. As above the variable *Eps* is the error calculated subtracting the reference image and the observed one. It is the main parameter employed for calculation of the quality indexes. All the parameters are calculated in pure numerical format: from these functions some graph are created to plot the results obtained from the previous calculations: the figures in the next chapters will show the theoretical image and the observed one (both normalized), with a red dot that represent the weighted centroid, the histogram plot of the two images (that show the number of the pixels having the same value), a comparison between the contour plot of the two image (useful to better understand if there are some difference in the shape of the FFDP) and a table in which are shown all the quality indexes calculated before. For the annulus analysis, for each image, a curve containing all the values of the total energy inside the region of interest is shown. Moreover a curve representing the difference between the values of energy in the annulus of the theoretical and the calculated FFDP is shown.

5.3 Analysis

The software realized to process the FFDP is able to perform different kind of analyses and each of them allow to investigate on different aspects of the pattern, both geometrical and energetic.

- Centroid calculation: as explained during the section about the working principle of the software, this kind of process allow to understand the center of the energetic distribution of the FFDP under analysis. When position of centroids is known a comparison with “intensity center” of

the reference can be performed: in this way it is possible to detect any kind of misalignment caused by geometrical movements. Moreover this calculation can be used also as a first approximation if energy distribution changes strongly after a test, if some loss or addiction of lobes happens.

(a) Theoretical (b) Observed

Figure 5.11: Image processed: the red dot is the calculated centroid

- Histograms: this analysis allow to better understand if FFDP processed has some saturated pixels, caused by a wrong setting of the camera. The plot shows the number of pixels (y-axis) that have the correspondent intensity value shown in x-axis. Hence, if maximum value of the scale is 1, when software processes the image and histogram analysis show a great number of pixels with 1 value means that the level of saturation doesn't allow to analyze image in a suitable way. This kind of analysis allow to change settings of the camera in order to have FFDP completely defined: if histogram shows a distribution of pixels with value included in the middle part of x-axis, image can be considered valid.

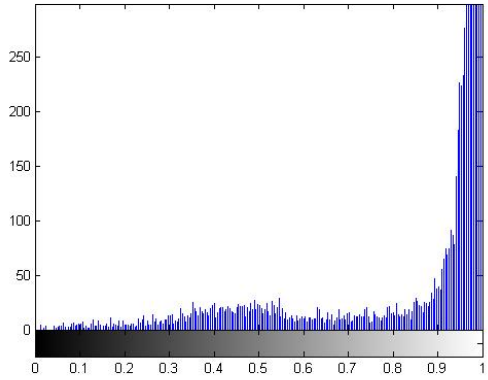

Figure 5.12: Histogram: example of saturated image

- Shape analysis: shape analysis is a first approximation geometrical analysis that allow to compare FFDP simply by eye: the lines of the contour plot match pixels at the same intensity. The number of lines can be selected in an option from MatLab *contour* function: to have a more clear comparison it is suitable to set a not so high number of lines.

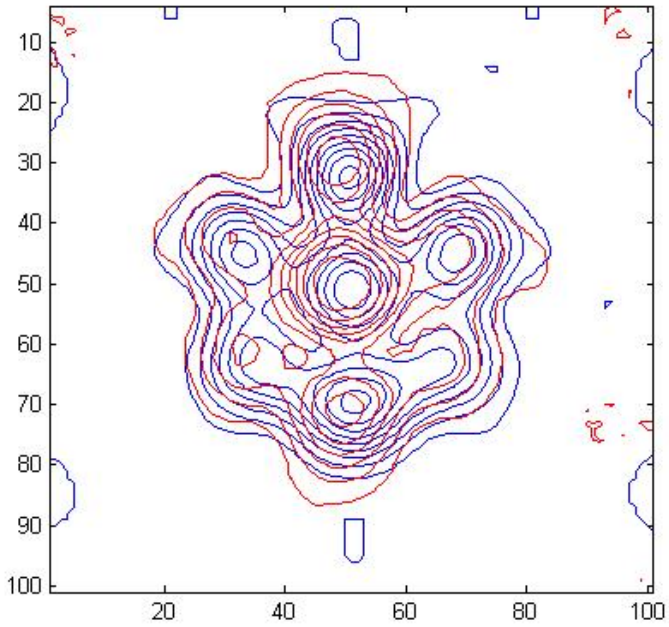

Figure 5.13: Contour plot of the image: red is reference and blue is observed

- Quality factors: the software generates a small table with all the coefficient shown in the table in the previous section: this allow to measure with numbers the difference between reference and observed FFDP. Among all the parameters, the main ones are probably RMS and peak S/N ratio: the first one gives an immediate value of the difference normalized between images, while the second allow to understand the background noise level in the image.

	Values
Root Mean Square Error (%)	8.9992
Maximum Difference	0.2859
Average Difference	0.0217
Normalize Absolute Error	0.0566
Normalized Cross Correlation	1.0085
Peak Signal to Noise Ratio	38.5888
WC X Difference (pxs)	0
WC Y Difference (pxs)	0

Figure 5.14: Example of table of quality indexes

- Annulus Analysis: this is probably the most important analysis performed by the software in order to understand the evolution of FFDP of the CCRs under test: this process allow to estimate the return signal in an area that simulates the zone all around the laser ranging station. As explained in the chapters above this analysis is strictly linked to the velocity aberration – so to the orbital calculation of the satellite – and to the calibration analysis. For LARES satellite the range of interest goes from 30 up to 50 μrad and the thickness of annulus is 20 μrad

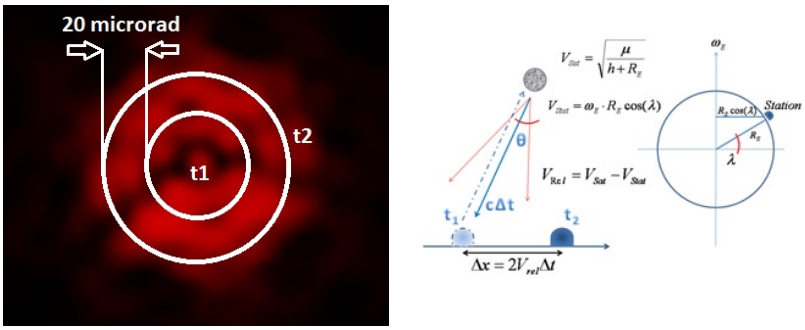

Figure 5.15: Conceptual view of annulus analysis

Chapter 6

Results

In this chapter the results obtained from image processing and analysis software will be shown. Results will be divided into two sections to better explain some of the effects observed during analysis of the FFDP. In the first section there will be the comparison between theoretical patterns and the observed ones realized in *GFZ* laboratory (these experiments have been performed after all the thermo-vacuum tests). The second section will show the comparison between the patterns observed during thermo-vacuum tests in Rome. The patterns shown are only a small part of the big amount of figures taken during all the tests: the more representative FFDP are shown.

6.1 Theoretical VS Observed: GFZ Stage

During June and July 2011 a collaboration with "*GFZ - GeoForschungsZentrum* " has been undertaken, in order to better understand the behavior of the prisms in test conditions and to improve the software for image analysis. During this period some tests have been performed in laboratory to take some FFDP in air and make some comparison with theoretical ones. The

optical bench employed to take the FFDPs is similar to the bench prepared in Rome, as shown in previous chapters. The difference between the two systems consists in the laser generator employed, even if in both cases a laser diode has been used: in Rome the laser is a red one ($\lambda = 635nm$), while the one in GFZ laboratory is a green one ($\lambda = 532nm$). All patterns have been processed using the software shown in previous chapter. All theoretical patterns come from the David Arnold's program "diffract01". The software provides printed output once the parameters for an ideal CCR (dihedral angle offset, angle, etc...) are set. The output needs to be post-processed if one wants to visualize the theoretical FFDP. Dr. Reinhart Neubert, using his software designed in "MathCad", provided us with *.bmp* images of the theoretical FFDP. All the theoretical pictures have to simulate the behavior of the real prism: to do this the value of the offset angle of the prisms under test have been introduced in calculation. The first tests have been made using a reference prism, property of GFZ, that has no dihedral angle offset: in this way all the analysis has been made on a well known figure, so that the optical bench could be set to best fit the observed patterns with the theoretical ones. Another aim of the test was the detection of any kind of deformation in the FFDP introduced by the optical bench. FFDP has been taken at various angles, measured starting from edge 1 going clockwise looking from the tip (direction of reflected beam): 0°, 30°, 60°, 120°, 240°. In the positions 0°, 120° and 240° the edges of the CCR, respectively edge 1, 2 and 3 are directed perpendicularly to the optical table defined as a reference plane. The CCR tab of edge 1 has the CCR ID number impressed; edge 2 and 3 are the edges obtained rotating clockwise the CCR of 120° and 240° from the first one. In figure 5.1 the rotation rule is shown.

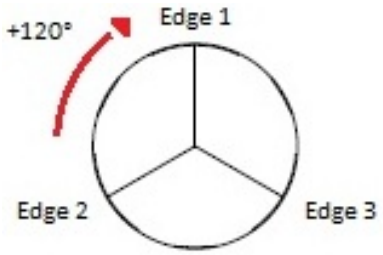

Figure 6.1: Rotation of the prism during the test. Tip of the prism is shown

In front of the camera a rotating polarizer has been positioned, so that the beam from the prism can be analyzed in all its components. If the polarizer is in vertical position it is in agreement with the laser polarization so that there will be no attenuation of the light at all. As known, in an uncoated CCR, each reflection reverses the sense of one component of the wave-vector for any particular incident ray, with the result that the ray finally emerges antiparallel to the direction of incidence, independently of the cube-corner orientation (RIFERIMENTO ARTICOLO FRANCIS). The polarization of the laser is vertical and camera settings are the following:

$$ISO = 200 \tag{6.1}$$

$$Exp = 1/125 \tag{6.2}$$

The analysis is based on the results coming from the intensity of the calibration pattern. The following figure has been realized employing a double slit screen in front of a flat mirror. The figure shows that the CCD of the camera is working correctly in a linear range and that laser beam is sufficiently uniform. The curve reports is the profile of the light intensity of the pixels of the middle row of the calibration pattern.

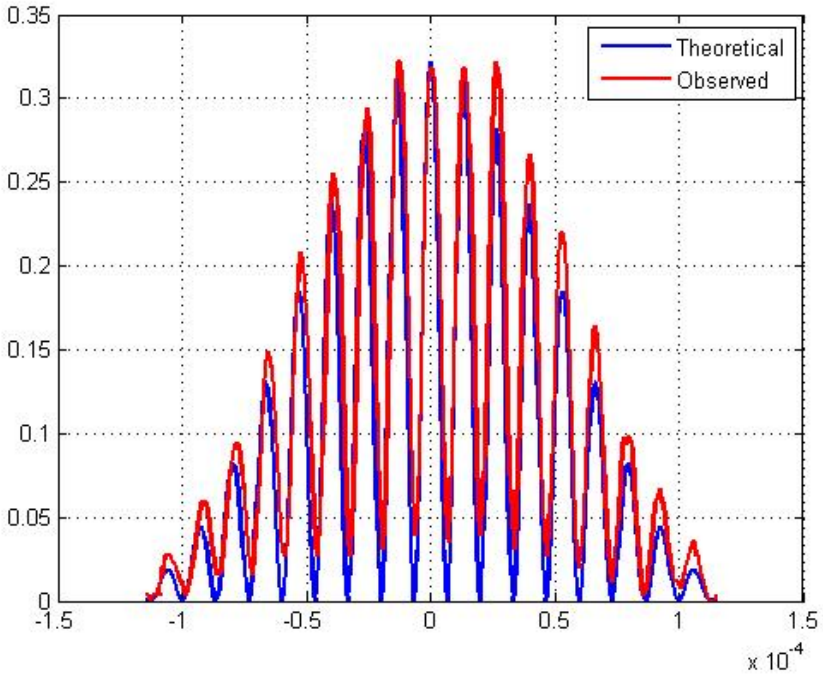

Figure 6.2: Diffraction pattern of the double slit: blue is calculated and red is observed.

The coefficient calculated for the conversion of pixels-to-microradians is:

$$\frac{\mu rad}{pixels} = 1.3570$$

FFDP from reference prism has been taken in different position, rotating the support in which it is mounted. Also an analysis on parallel and orthogonal component of the FFDP - respect to the polarization direction - has been performed.

6.1.1 Reference Prism: Total - Angle = 0°

These pictures has been generated using the MatLab software described in the previous chapters: as written above a theoretical pattern, obtained from mathematical calculation, has been compared with a pattern observed during a test with the optical bench in GFZ. This test has been performed to better understand the functioning of the software and its analysis capability. The image treated is a well known pattern: a CCR with zero dihedral angle offset. In this first phase test the analysis performed regards only the detection of the FFDP, the centroid calculation (red dot), a pixel intensity analysis and the shape analysis.

(a) Theoretical (b) Observed

Figure 6.3: Theoretical and Observed Image

	Values
Root Mean Square Error (%)	8.9992
Maximum Difference	0.2859
Average Difference	0.0217
Normalize Absolute Error	0.0566
Normalized Cross Correlation	1.0085
Peak Signal to Noise Ratio	38.5888
WC X Difference (pxs)	0
WC Y Difference (pxs)	0

Figure 6.4: Table of quality indexes

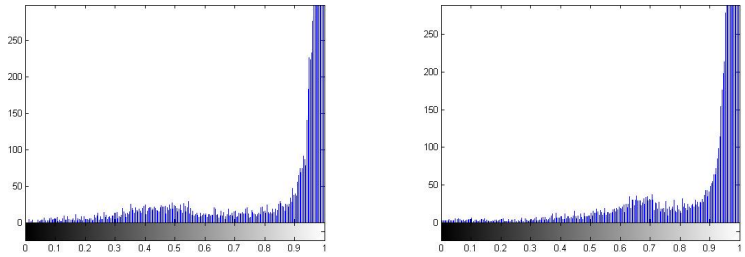

(a) Theoretical (b) Observed

Figure 6.5: Histogram of Images: theoretical and observed

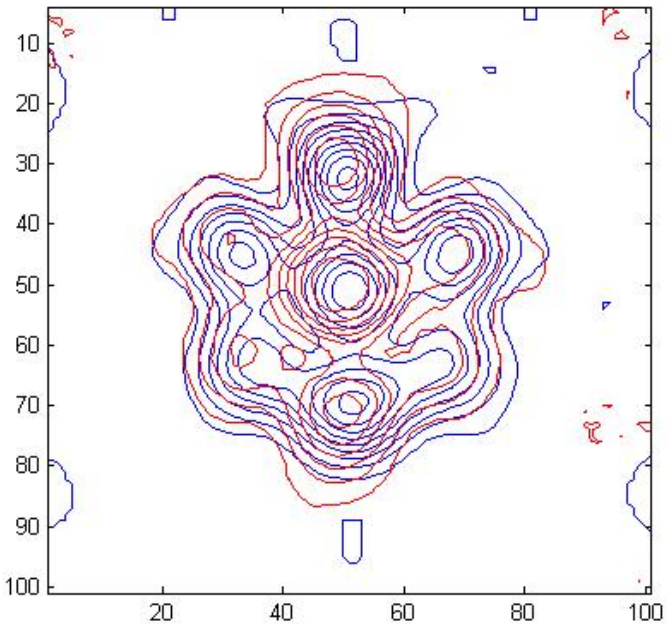

Figure 6.6: Contour plot of the image: red is reference and blue is observed

From the graphs showed above and referring to the table of values calculated during the analysis seems that the distribution of energy can be easily comparable because the centroids of the two figures are very close (this ef-

fect can be seen superimposing the figures generated after the analysis): this means that the shape analysis will show contours lines very close each other. Looking at the table in figure 5.4 it results that almost all the comparisons performed with the numerical factor described in the previous chapter are represented by small numbers: the RMS between the figures is under 10%, the average difference is around 2% and the factor of correlation is close to 1. The S/N ratio is high: this is strictly linked to the environment in which the observed pattern has been taken. Even if the background light has been reduced as possible some noise is still present. Another remark can be done on the pixels intensity analysis: the histograms shows a very similar distribution of the light intensity. The great number of pixels saturated (1 value) come from the particular kind of CCR employed for the test: with no dihedral angle offset the light form the CCR is centered on a small part of the camera CCD and obviously, even if camera works in linear range, saturation of the pixels is present.

6.1.2 Reference Prism: Parallel Component - Angle 0°

As above this figure shows another comparisons between the calculated and observed parallel component of the FFDP of the test CCR with no dihedral angle offset. As explained above these test have been made to have a plain idea of the functioning of the software.

(a) Theoretical (b) Observed

Figure 6.7: Theoretical and Observed Image

	Values
Root Mean Square Error (%)	7.4042
Maximum Difference	0.3552
Average Difference	0.0085
Normalize Absolute Error	0.0474
Normalized Cross Correlation	0.9848
Peak Signal to Noise Ratio	39.4360
WC X Difference (pxs)	0
WC Y Difference (pxs)	0

Figure 6.8: Table of quality indexes

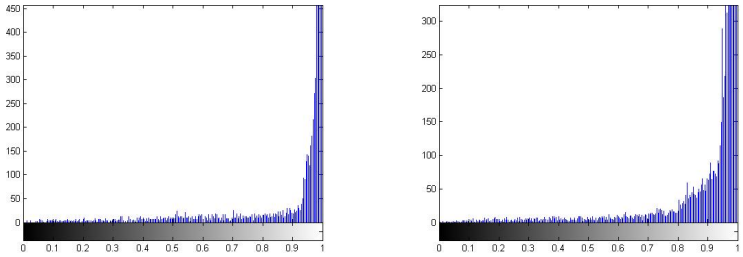

(a) Theoretical (b) Observed

Figure 6.9: Histogram of Images: theoretical and observed

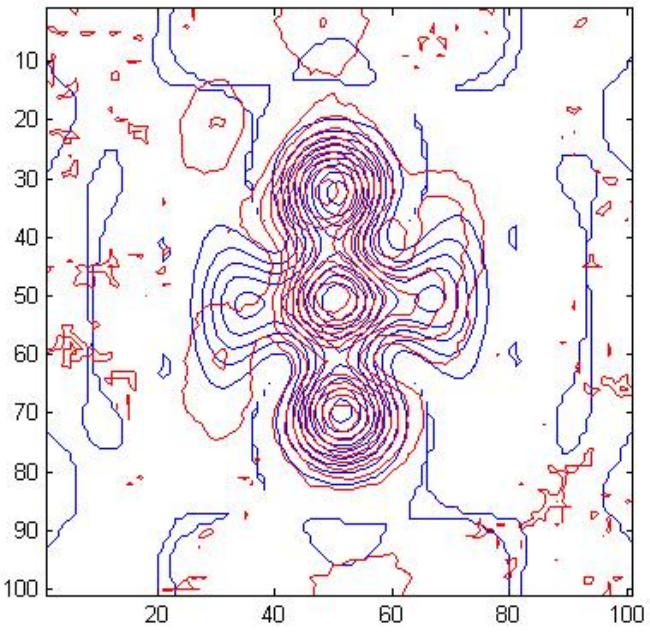

Figure 6.10: Contour plot of the image: red is reference and blue is observed

As for the previous analysis pictures can be easily compared because the centroids of the energy distribution is quite similar. So all the comments made for the previous analysis can be considered valid also for these tests. It

had to be noticed that the observed patterns seems to be a little misaligned on the vertical direction in respect to the theoretical picture: even if this effect is present all the analysis give good results, comparable with the previous ones. In this case the background noise increases a little.

6.1.3 Reference Prism: Orthogonal Component - Angle 0°

This another test realized on the CCR with no dihedral angle offset: in this case the orthogonal component of the FFDP has been analyzed. As in the previous analysis the comparison is realized between a calculated distribution of energy and an observed one.

(a) Theoretical (b) Observed

Figure 6.11: Theoretical and Observed Image

	Values
Root Mean Square Error (%)	10.7018
Maximum Difference	0.4961
Average Difference	0.0204
Normalize Absolute Error	0.0663
Normalized Cross Correlation	0.9722
Peak Signal to Noise Ratio	37.8362
WC X Difference (pxs)	0
WC Y Difference (pxs)	0

Figure 6.12: Table of quality indexes

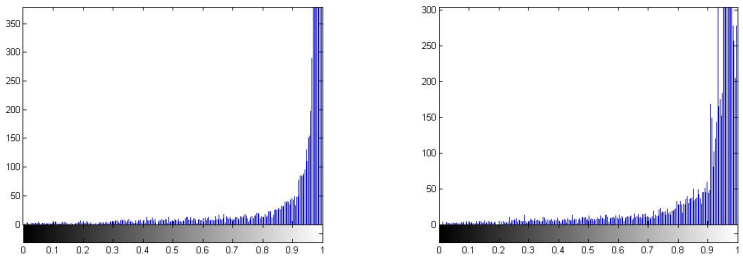

(a) Theoretical (b) Observed

Figure 6.13: Histogram of Images: theoretical and observed

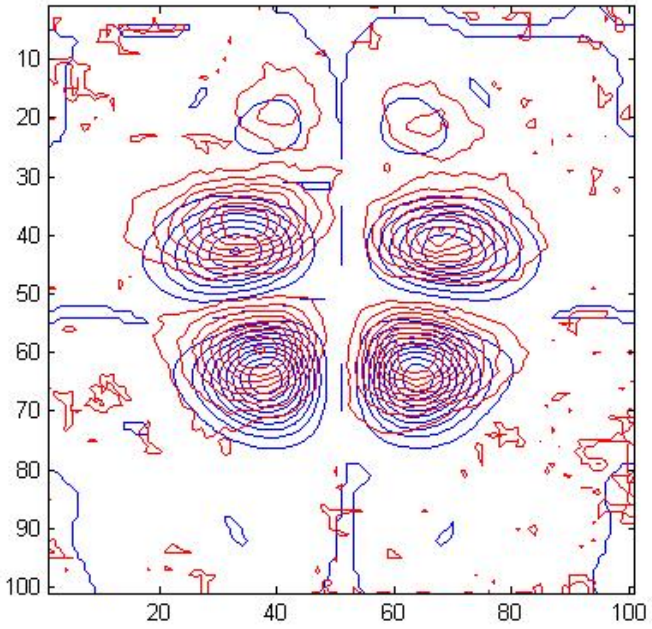

Figure 6.14: Contour plot of the image: red is reference and blue is observed

All the comments on these analysis are very similar to the ones made for the images above. In this case there is an increased RMS probably caused by a bigger amount of background noise.

6.1.4 Reference Prism: Angle = 120°

With this experience the symmetry of the reference prism has been tested: rotating the CCR according to the laws described in the first part of this chapter, FFDP with edge 2 upward has been taken and analyzed. If CCR has been realized in respect to the optical tolerance imposed the FFDP will be absolutely symmetric.

(a) Theoretical (b) Observed

Figure 6.15: Theoretical and Observed Image

	Values
Root Mean Square Error (%)	11.9449
Maximum Difference	0.4709
Average Difference	0.0678
Normalize Absolute Error	0.0733
Normalized Cross Correlation	0.9342
Peak Signal to Noise Ratio	37.3590
WC X Difference (pxs)	0
WC Y Difference (pxs)	0

Figure 6.16: Table of quality indexes

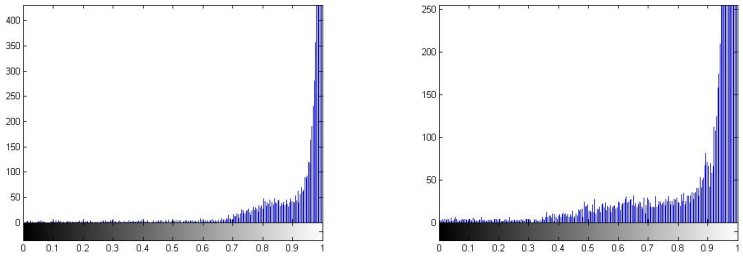

(a) Theoretical (b) Observed

Figure 6.17: Histogram of Images: theoretical and observed

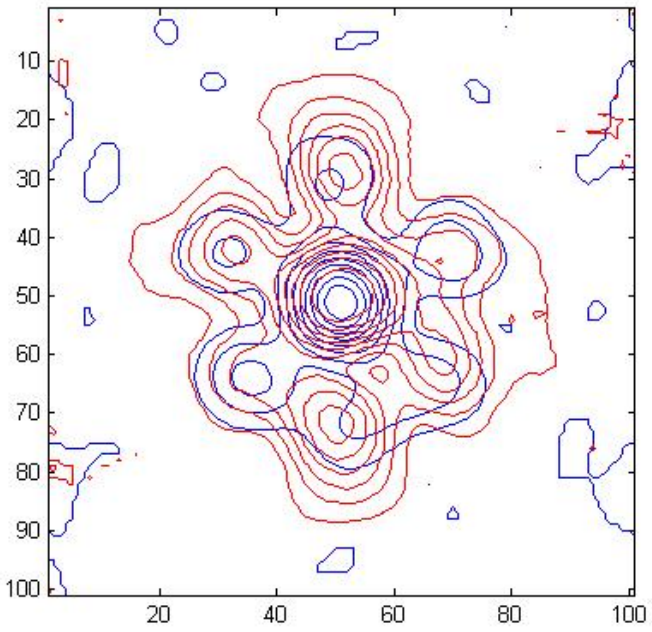

Figure 6.18: Contour plot of the image: red is reference and blue is observed

The analysis shows that the symmetry is respected: shape analysis and the table of mathematical value shows some acceptable results ($RMS \simeq 10\%$, background noise level near to the other analysis). The tolerance of the three

back-faces has been checked from Carl Zeiss's datasheet of the prism and it is equal on all the faces: for this reason probably part of the errors measured can be caused by a little misalignment between the plane of polarization of the laser and the direction of the edge: the rotating system in which the prism was enclosed allowed only rotation by hand, without a micrometric screw for precision movements, so some degrees of difference could have raised up the error between theoretical and observed images.

6.1.5 Reference Prism: Angle = 240°

As in the previous analysis FFDP with edge 3 up has been taken and analyzed. In this case the results expected from the analysis changes from the previous cases because of the possible misalignment between the polarization plane and the edge of the CCR.

(a) Theoretical (b) Observed

Figure 6.19: Theoretical and Observed Image

	Values
Root Mean Square Error (%)	12.4816
Maximum Difference	0.5831
Average Difference	0.0646
Normalize Absolute Error	0.0727
Normalized Cross Correlation	0.9380
Peak Signal to Noise Ratio	37.1681
WC X Difference (pxs)	0
WC Y Difference (pxs)	0

Figure 6.20: Table of quality indexes

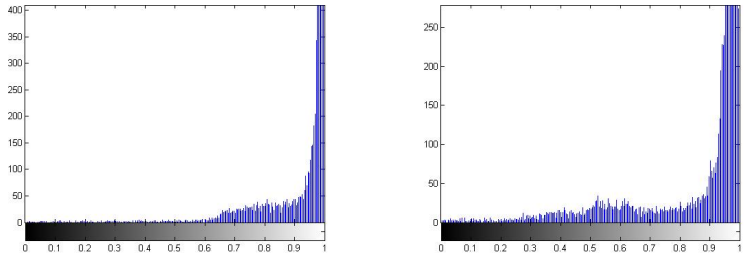

(a) Theoretical (b) Observed

Figure 6.21: Histogram of Images: theoretical and observed

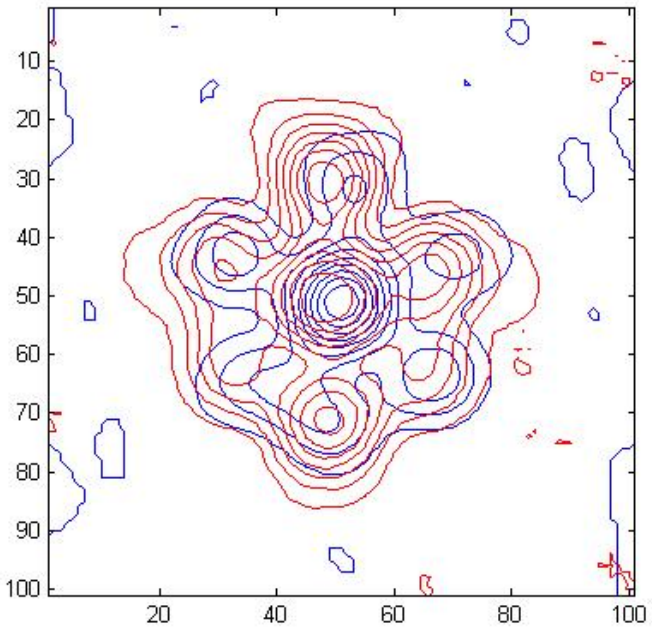

Figure 6.22: Contour plot of the image: red is reference and blue is observed

As shown by the analysis the difference between the patterns is around 10%. This effect can be assumed coming from some misalignment in the position of the prism: it has been introduced into the mounting system, po-

sitioned on the bench and rotated by hand, so that the probability to have some degrees of misalignment respect to the position in which the theoretical pattern has been calculated is quite high. However, excluding these small effects, evaluating from the calibration pattern that camera was linearly working and also evaluating the shape analysis it is possible to believe that the optical bench doesn't introduce negative effects on the FFDPs.

6.2 CCR from LARES

Before to show all the analysis and the results obtained from the image treatment applied to the FFDP taken during the test in simulated space environment some results from general tests on LARES CCRs will be shown and commented: some effects noticed during the analysis of reference prism from GFZ has suggested to make some optical experiments taking FFDP simply in air in order to fix a sort of "bias" that has to be considered during the analysis of thermo-vacuum tests. The experiences realized in GFZ with the prism No°92 (property of GFZ), No°54 and No°51 have shown some structural effects, different for each prism, caused by a probable deformation on the back-faces or on the front face of the CCR. These effects can be revealed by an observation of the FFDP observed with the optical bench compared with the theoretical ones calculated with the software of Reinhart Neubert. These deformations can't be detected easily because the causes could derives from various factors: deformations caused by mechanical stress, deformation caused by thermal stress, deformation caused by a not-respected optical tolerance during working processes, etc. Anyway it is impossible to assess these kind of effects only by an analysis of FFDP: to do this a interferometric analysis of the optical surfaces is absolutely required. During GFZ stages some requests of these informations has been forwarded to the manufacturers of the CCR, but, because of the CCRs has been realized several years ago, it has been impossible recover these data in few time. For this reason the nature of these deformations can be detected only by similarity between theoretical and observed patterns: anyway it was almost impossible to realize theoretical patterns close to the observed one without the informations about the deformations. Anyway some trials on the theoretical patterns have been performed in order to detect as best as possible some of the deforma-

tions: several images of FFDP has been computed but the results have had no match with the observed patterns.

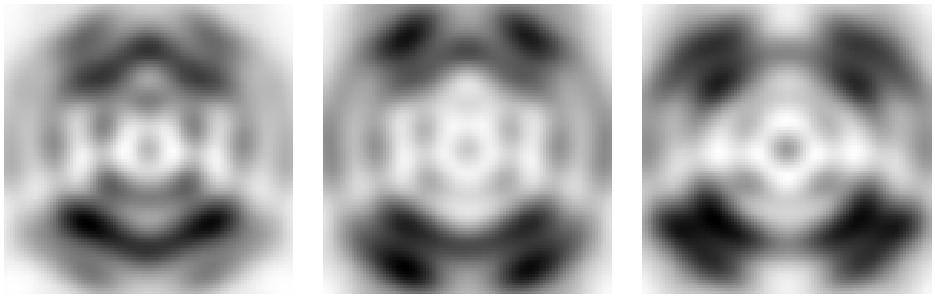

(a) Plane Front Face (b) Spherical Front face (c) Cylindrical Front Face

Figure 6.23: Examples of patterns from CCR with different curvature of front face

Hence these effects, not modeled in the theoretical patterns employed for the comparisons, causes a quite strong error in the calculation of the quality factors and in the morphological analysis. The theoretical patterns employed are calculated using the known (from Zeiss) offset angles but assuming ideal flat surfaces. Some other errors has been introduced also because of some small changes in azimuth angles between figures as seen in previous cases. For this reason the optical general analysis on LARES prisms have been considered in themselves, without any influence on the other results. Anyway the tests performed gave an idea of a random "error level" that should have to be taken into account in other possible optical analysis: obviously if the comparison is performed between a reference and observed FFDP taken on the same CCR these effects can be neglected. All the tests have been performed following the laws explained above, with the exception of the parallel and orthogonal component. In this section all the results will be shown without comments to avoid repetitions and because the results coming from

the tests are explained as well as possible above: because is not possible to quantify how these effects affect FFDP any comment on the morphological analysis and on the quality factor is considered useless. The results are the following:

6.2.1 CCR no° 92: Angle = 0°

(a) Theoretical (b) Observed

Figure 6.24: Theoretical and Observed Image

	Values
Root Mean Square Error (%)	21.6762
Maximum Difference	0.6306
Average Difference	0.0911
Normalize Absolute Error	0.2542
Normalized Cross Correlation	1.0886
Peak Signal to Noise Ratio	34.7710
WC X Difference (pxs)	1
WC Y Difference (pxs)	0

Figure 6.25: Table of quality indexes

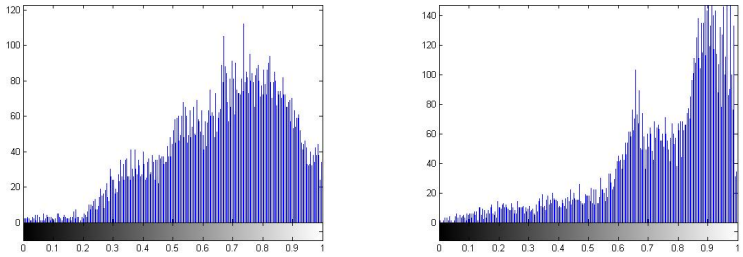

(a) Theoretical (b) Observed

Figure 6.26: Histogram of Images: theoretical and observed

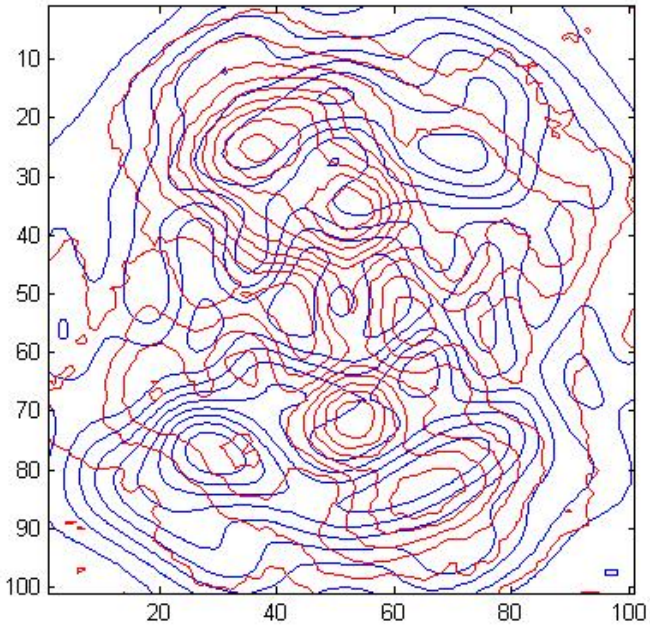

Figure 6.27: Contour plot of the image: red is reference and blue is observed

6.2.2 CCR no° 92: Angle = 30°

(a) Theoretical (b) Observed

Figure 6.28: Theoretical and Observed Image

	Values
Root Mean Square Error (%)	20.7316
Maximum Difference	0.6128
Average Difference	0.0176
Normalize Absolute Error	0.2547
Normalized Cross Correlation	0.9921
Peak Signal to Noise Ratio	34.9645
WC X Difference (pxs)	1
WC Y Difference (pxs)	0

Figure 6.29: Table of quality indexes

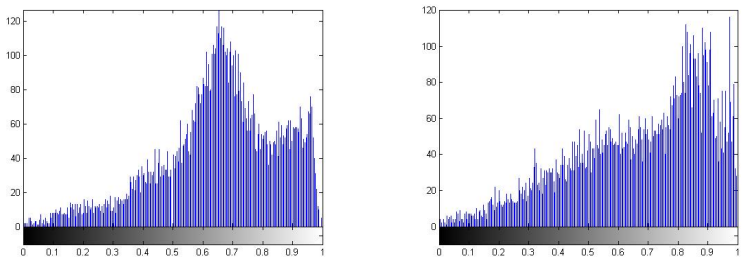

(a) Theoretical (b) Observed

Figure 6.30: Histogram of Images: theoretical and observed

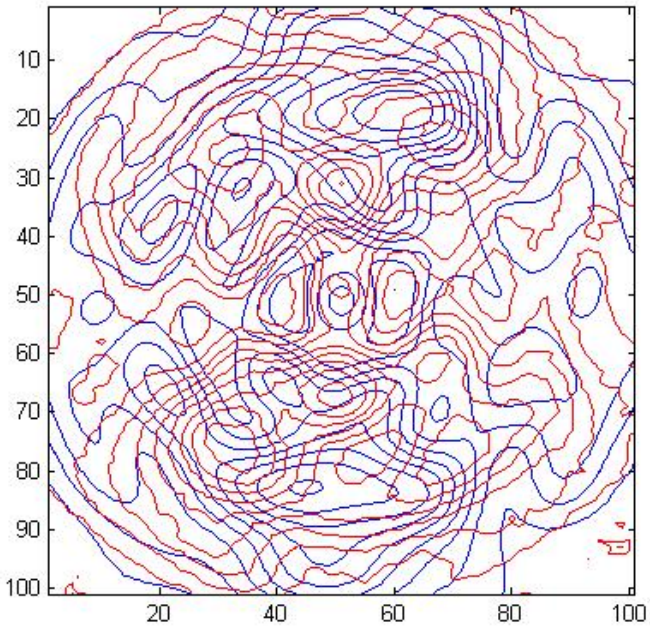

Figure 6.31: Contour plot of the image: red is reference and blue is observed

6.2.3 CCR no° 92: Angle = 60°

(a) Theoretical (b) Observed

Figure 6.32: Theoretical and Observed Image

	Values
Root Mean Square Error (%)	24.0513
Maximum Difference	0.5804
Average Difference	0.0649
Normalize Absolute Error	0.2915
Normalized Cross Correlation	1.0476
Peak Signal to Noise Ratio	34.3194
WC X Difference (pxs)	0
WC Y Difference (pxs)	2

Figure 6.33: Table of quality indexes

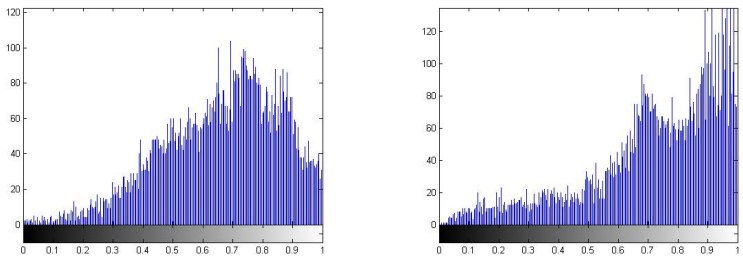

(a) Theoretical (b) Observed

Figure 6.34: Histogram of Images: theoretical and observed

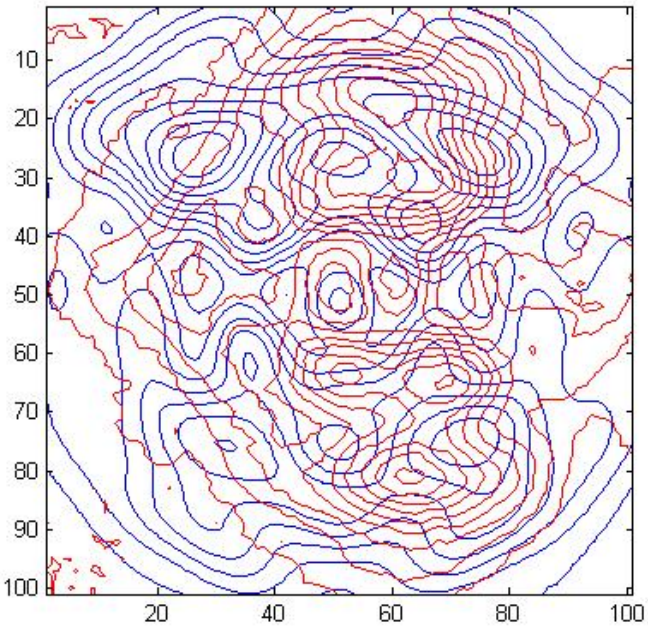

Figure 6.35: Contour plot of the image: red is reference and blue is observed

6.2.4 CCR no° 92: Angle = 120°

(a) Theoretical (b) Observed

Figure 6.36: Theoretical and Observed Image

	Values
Root Mean Square Error (%)	23.2582
Maximum Difference	0.5545
Average Difference	0.1274
Normalize Absolute Error	0.2958
Normalized Cross Correlation	1.1258
Peak Signal to Noise Ratio	34.4650
WC X Difference (pxs)	1
WC Y Difference (pxs)	0

Figure 6.37: Table of quality indexes

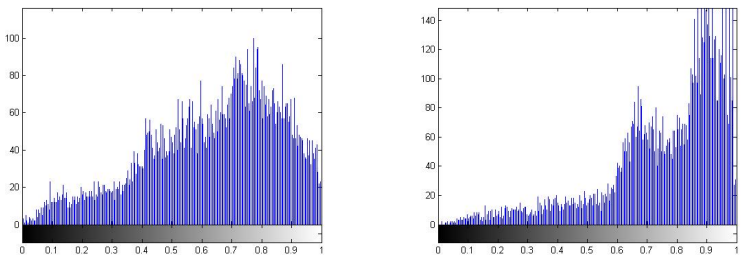

(a) Theoretical (b) Observed

Figure 6.38: Histogram of Images: theoretical and observed

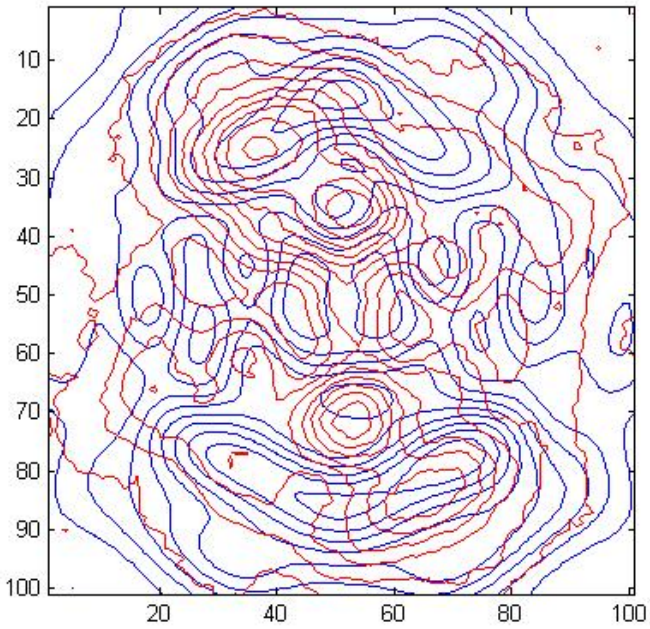

Figure 6.39: Contour plot of the image: red is reference and blue is observed

6.2.5 CCR no° 92: Angle = 240°

(a) Theoretical (b) Observed

Figure 6.40: Theoretical and Observed Image

	Values
Root Mean Square Error (%)	19.6194
Maximum Difference	0.6768
Average Difference	0.1017
Normalize Absolute Error	0.2405
Normalized Cross Correlation	1.1078
Peak Signal to Noise Ratio	35.2039
WC X Difference (pxs)	1
WC Y Difference (pxs)	0

Figure 6.41: Table of quality indexes

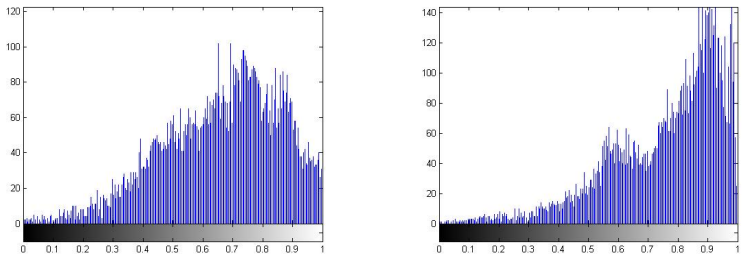

(a) Theoretical (b) Observed

Figure 6.42: Histogram of Images: theoretical and observed

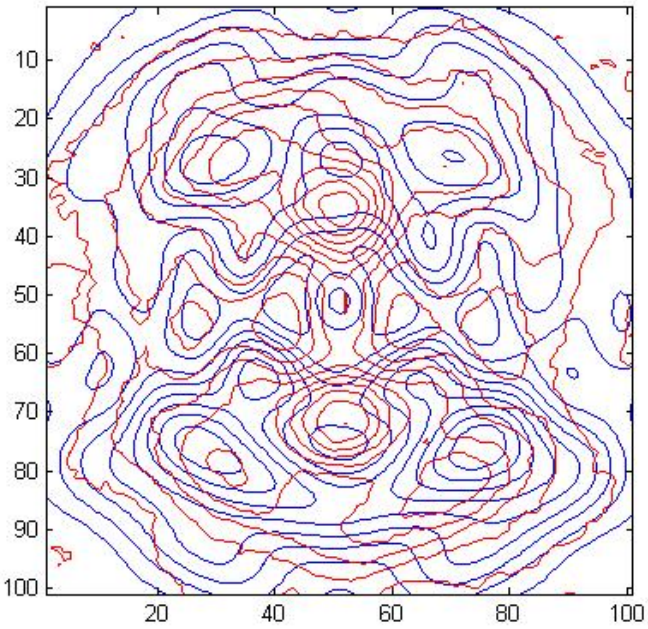

Figure 6.43: Contour plot of the image: red is reference and blue is observed

6.2.6 CCR no° 51: Angle = 0°

(a) Theoretical (b) Observed

Figure 6.44: Theoretical and Observed Image

	Values
Root Mean Square Error (%)	23.7834
Maximum Difference	0.6425
Average Difference	0.0970
Normalize Absolute Error	0.2613
Normalized Cross Correlation	1.0618
Peak Signal to Noise Ratio	34.3681
WC X Difference (pxs)	1
WC Y Difference (pxs)	1

Figure 6.45: Table of quality indexes

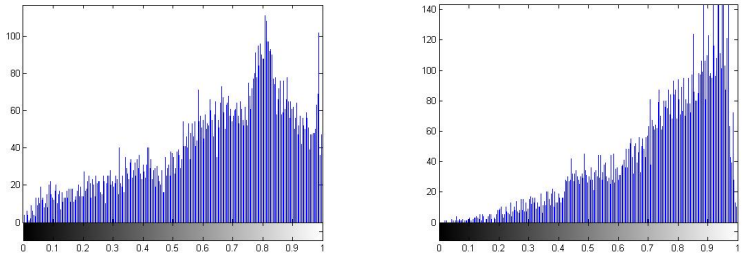

(a) Theoretical (b) Observed

Figure 6.46: Histogram of Images: theoretical and observed

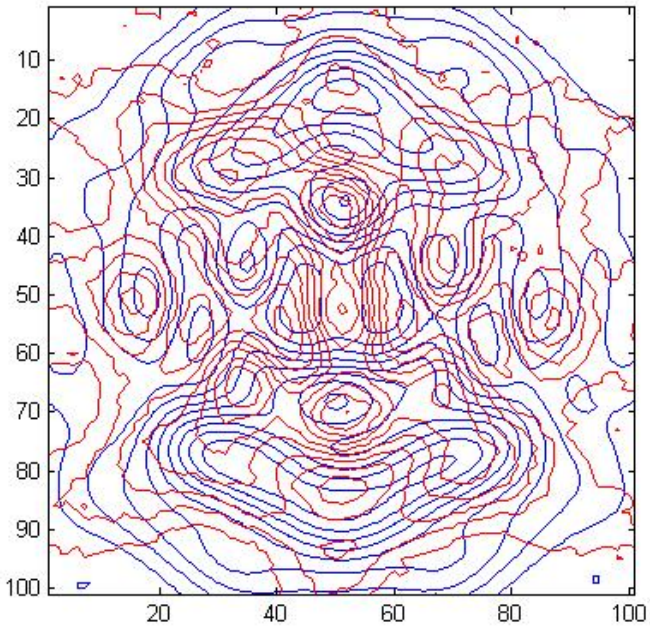

Figure 6.47: Contour plot of the image: red is reference and blue is observed

6.2.7 CCR no° 51: Angle = 30°

(a) Theoretical (b) Observed

Figure 6.48: Theoretical and Observed Image

	Values
Root Mean Square Error (%)	17.9421
Maximum Difference	0.6642
Average Difference	0.0454
Normalize Absolute Error	0.1809
Normalized Cross Correlation	1.0336
Peak Signal to Noise Ratio	35.5921
WC X Difference (pxs)	0
WC Y Difference (pxs)	0

Figure 6.49: Table of quality indexes

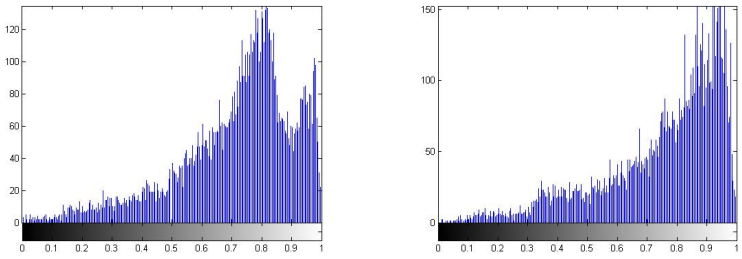

(a) Theoretical (b) Observed

Figure 6.50: Histogram of Images: theoretical and observed

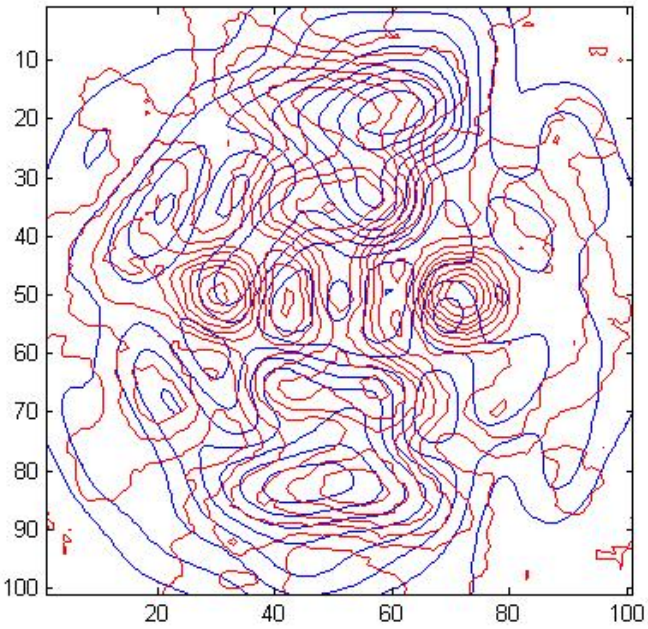

Figure 6.51: Contour plot of the image: red is reference and blue is observed

6.2.8 CCR no° 51: Angle = 60°

(a) Theoretical (b) Observed

Figure 6.52: Theoretical and Observed Image

	Values
Root Mean Square Error (%)	19.3653
Maximum Difference	0.4806
Average Difference	0.1124
Normalize Absolute Error	0.2282
Normalized Cross Correlation	1.1137
Peak Signal to Noise Ratio	35.2606
WC X Difference (pxs)	1
WC Y Difference (pxs)	0

Figure 6.53: Table of quality indexes

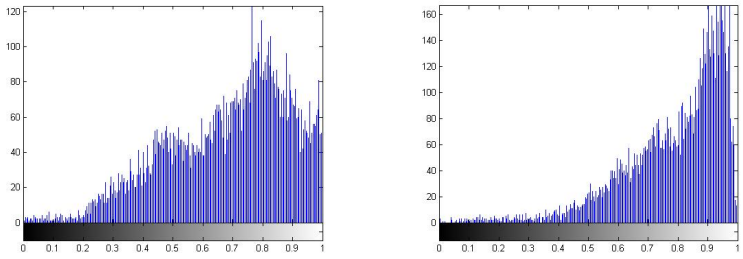

(a) Theoretical (b) Observed

Figure 6.54: Histogram of Images: theoretical and observed

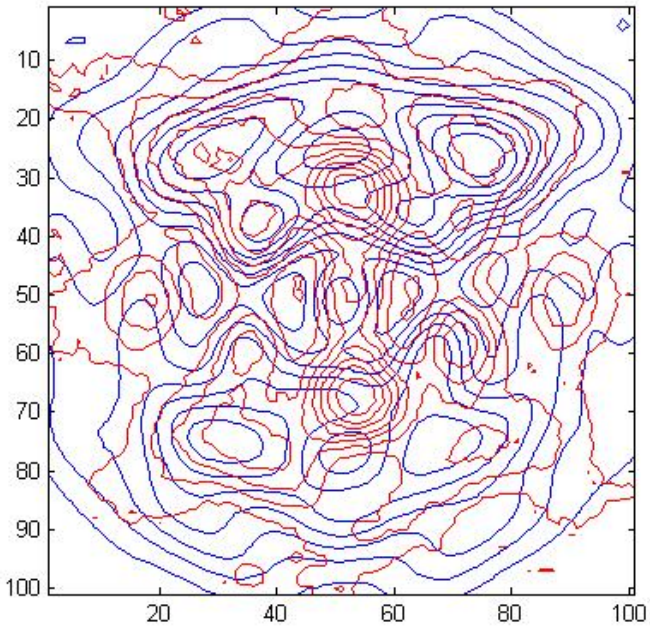

Figure 6.55: Contour plot of the image: red is reference and blue is observed

6.2.9 CCR no° 51: Angle = 120°

(a) Theoretical (b) Observed

Figure 6.56: Theoretical and Observed Image

	Values
Root Mean Square Error (%)	19.4831
Maximum Difference	0.6424
Average Difference	0.0810
Normalize Absolute Error	0.2153
Normalized Cross Correlation	1.0710
Peak Signal to Noise Ratio	35.2342
WC X Difference (pxs)	0
WC Y Difference (pxs)	0

Figure 6.57: Table of quality indexes

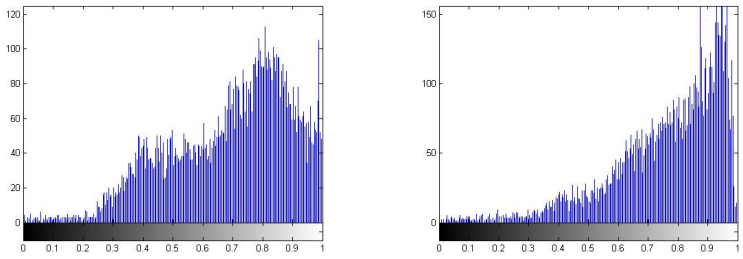

(a) Theoretical (b) Observed

Figure 6.58: Histogram of Images: theoretical and observed

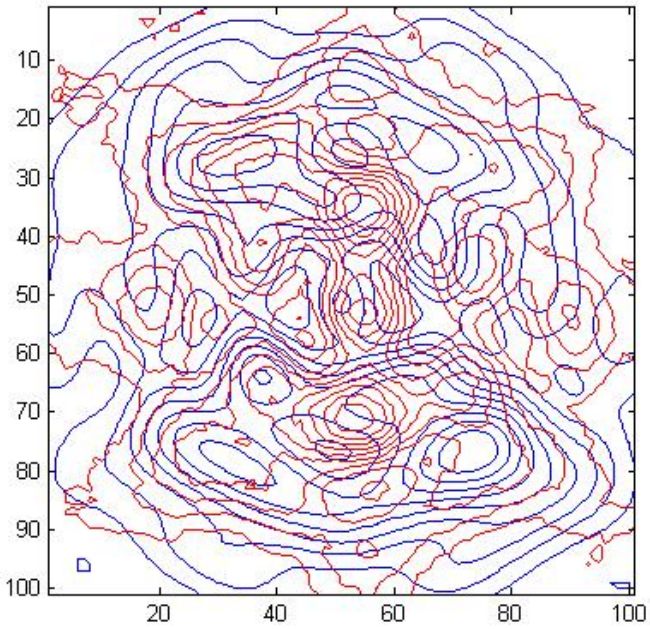

Figure 6.59: Contour plot of the image: red is reference and blue is observed

6.2.10 CCR no° 51: Angle = 240°

(a) Theoretical (b) Observed

Figure 6.60: Theoretical and Observed Image

	Values
Root Mean Square Error (%)	21.9673
Maximum Difference	0.6474
Average Difference	0.1064
Normalize Absolute Error	0.2536
Normalized Cross Correlation	1.0962
Peak Signal to Noise Ratio	34.7130
WC X Difference (pxs)	0
WC Y Difference (pxs)	0

Figure 6.61: Table of quality indexes

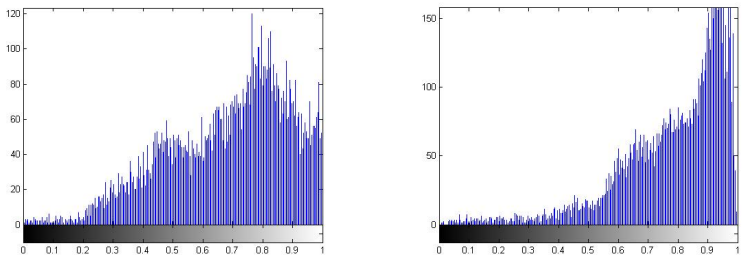

(a) Theoretical (b) Observed

Figure 6.62: Histogram of Images: theoretical and observed

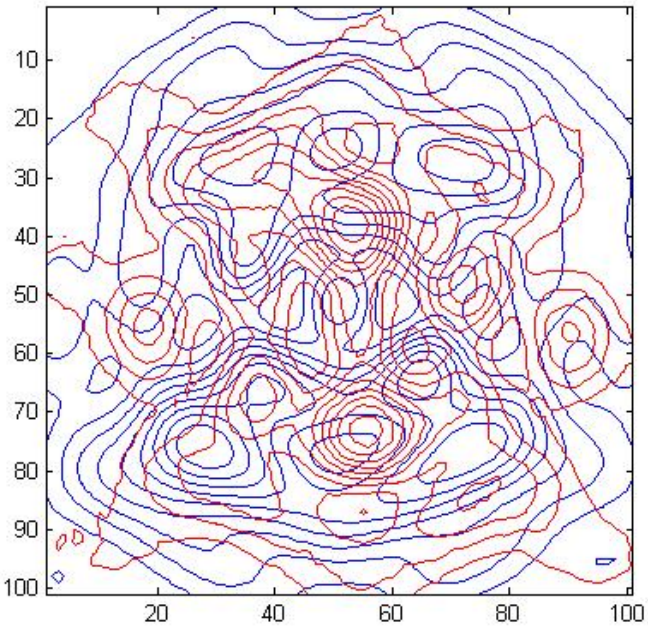

Figure 6.63: Contour plot of the image: red is reference and blue is observed

6.2.11 CCR no° 54: Angle = 0°

(a) Theoretical (b) Observed

Figure 6.64: Theoretical and Observed Image

	Values
Root Mean Square Error (%)	24.5993
Maximum Difference	0.6372
Average Difference	0.1534
Normalize Absolute Error	0.3020
Normalized Cross Correlation	1.1592
Peak Signal to Noise Ratio	34.2216
WC X Difference (pxs)	1
WC Y Difference (pxs)	1

Figure 6.65: Table of quality indexes

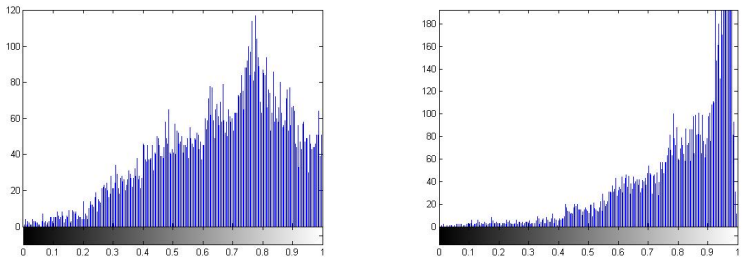

(a) Theoretical (b) Observed

Figure 6.66: Histogram of Images: theoretical and observed

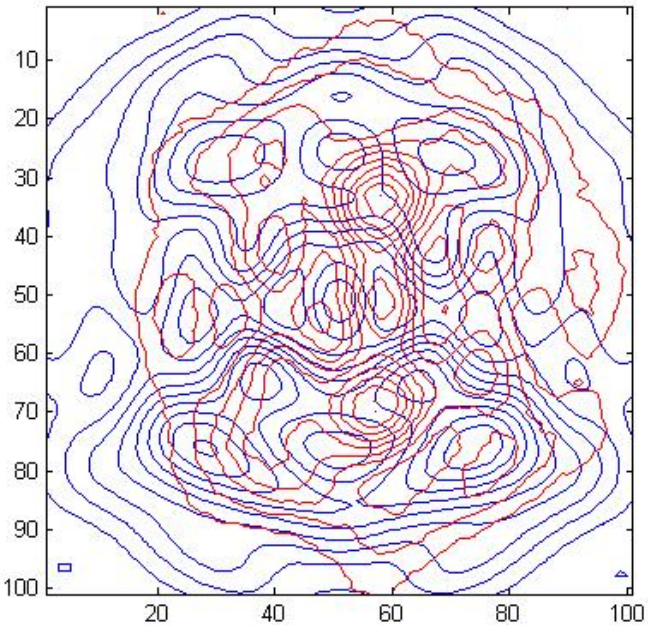

Figure 6.67: Contour plot of the image: red is reference and blue is observed

6.2.12 CCR no° 54: Angle = 30°

(a) Theoretical (b) Observed

Figure 6.68: Theoretical and Observed Image

	Values
Root Mean Square Error (%)	21.6021
Maximum Difference	0.4595
Average Difference	0.1192
Normalize Absolute Error	0.2544
Normalized Cross Correlation	1.1249
Peak Signal to Noise Ratio	34.7858
WC X Difference (pxs)	0
WC Y Difference (pxs)	0

Figure 6.69: Table of quality indexes

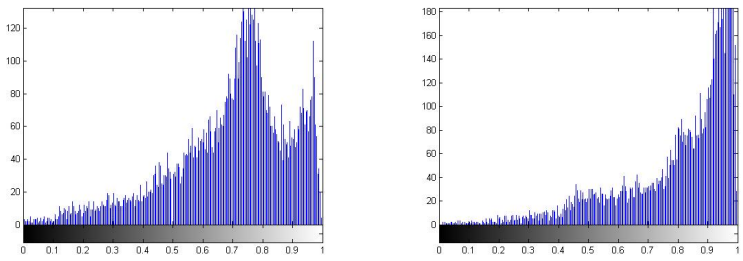

(a) Theoretical (b) Observed

Figure 6.70: Histogram of Images: theoretical and observed

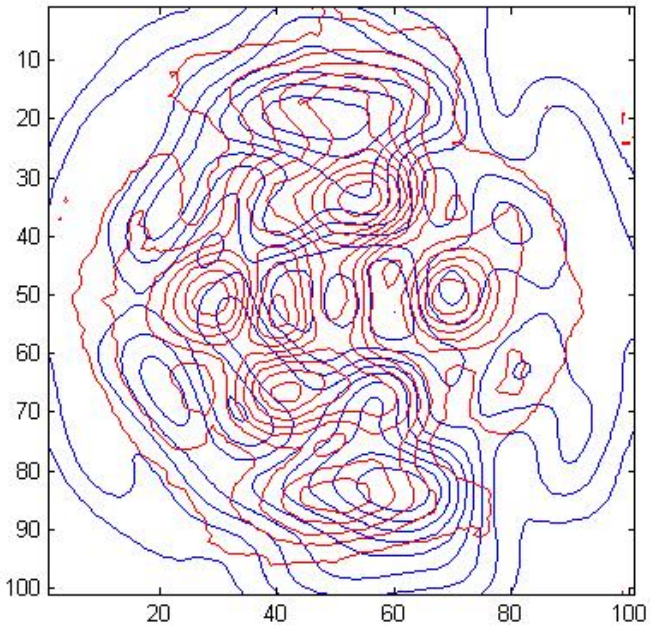

Figure 6.71: Contour plot of the image: red is reference and blue is observed

6.2.13 CCR no° 54: Angle = 60°

(a) Theoretical (b) Observed

Figure 6.72: Theoretical and Observed Image

	Values
Root Mean Square Error (%)	26.5127
Maximum Difference	0.8140
Average Difference	0.1532
Normalize Absolute Error	0.3191
Normalized Cross Correlation	1.1477
Peak Signal to Noise Ratio	33.8963
WC X Difference (pxs)	0
WC Y Difference (pxs)	0

Figure 6.73: Table of quality indexes

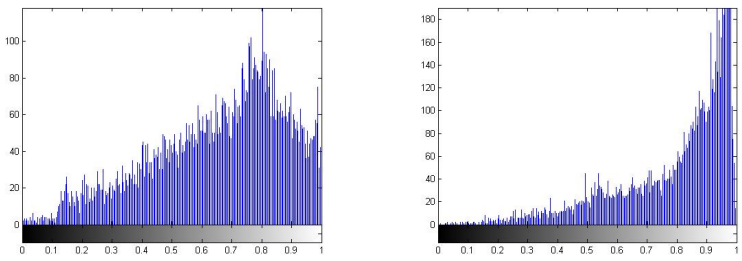

(a) Theoretical (b) Observed

Figure 6.74: Histogram of Images: theoretical and observed

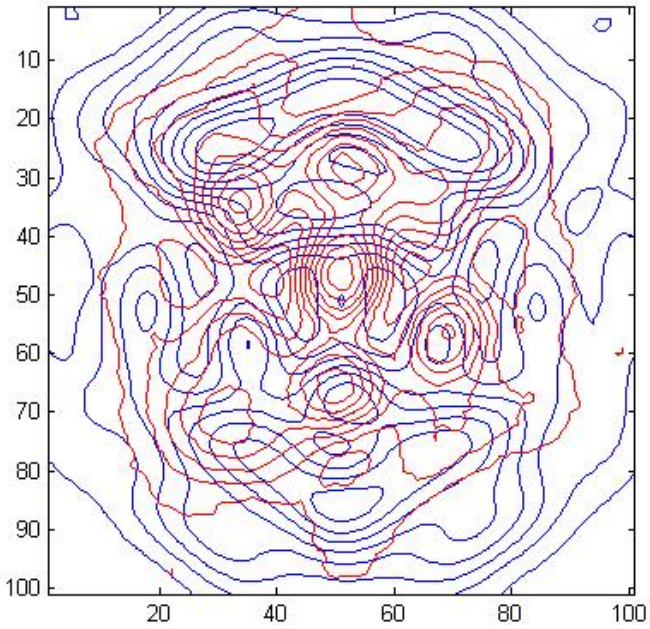

Figure 6.75: Contour plot of the image: red is reference and blue is observed

6.2.14 CCR no° 54: Angle = 120°

(a) Theoretical (b) Observed

Figure 6.76: Theoretical and Observed Image

	Values
Root Mean Square Error (%)	25.7697
Maximum Difference	0.7566
Average Difference	0.1273
Normalize Absolute Error	0.3029
Normalized Cross Correlation	1.1223
Peak Signal to Noise Ratio	34.0197
WC X Difference (pxs)	0
WC Y Difference (pxs)	0

Figure 6.77: Table of quality indexes

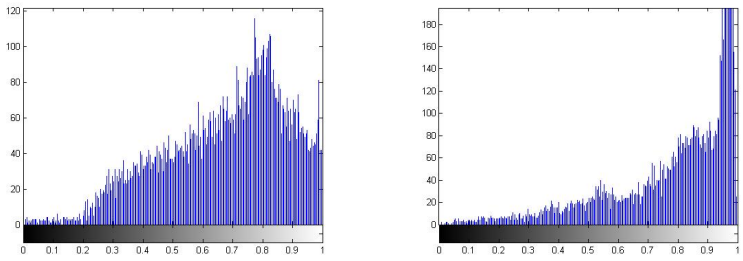

(a) Theoretical (b) Observed

Figure 6.78: Histogram of Images: theoretical and observed

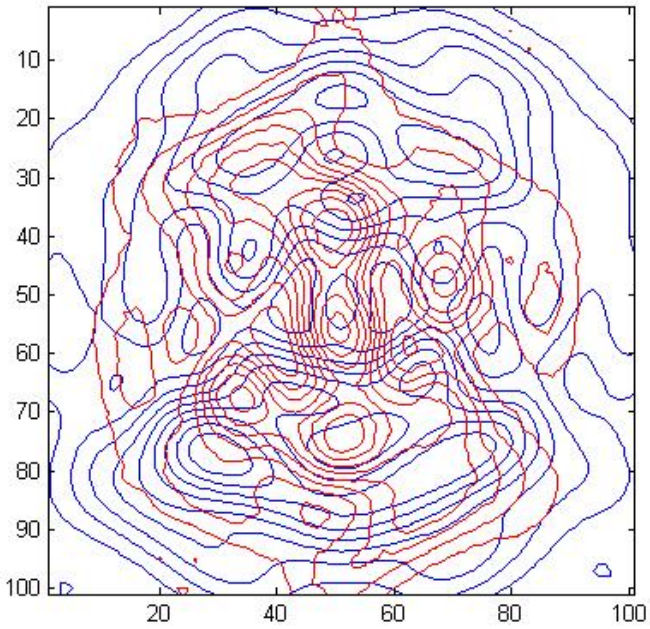

Figure 6.79: Contour plot of the image: red is reference and blue is observed

6.2.15 CCR no° 54: Angle = 240°

(a) Theoretical (b) Observed

Figure 6.80: Theoretical and Observed Image

	Values
Root Mean Square Error (%)	27.2547
Maximum Difference	0.7922
Average Difference	0.1540
Normalize Absolute Error	0.3221
Normalized Cross Correlation	1.1453
Peak Signal to Noise Ratio	33.7764
WC X Difference (pxs)	1
WC Y Difference (pxs)	0

Figure 6.81: Table of quality indexes

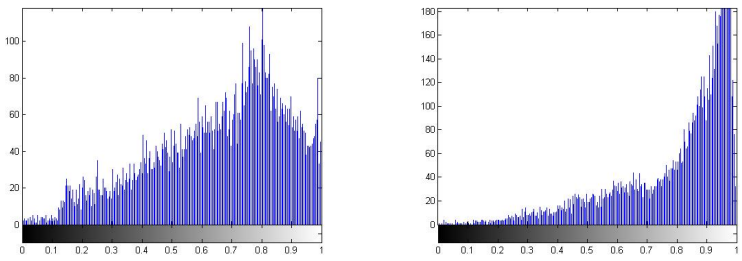

(a) Theoretical (b) Observed

Figure 6.82: Histogram of Images: theoretical and observed

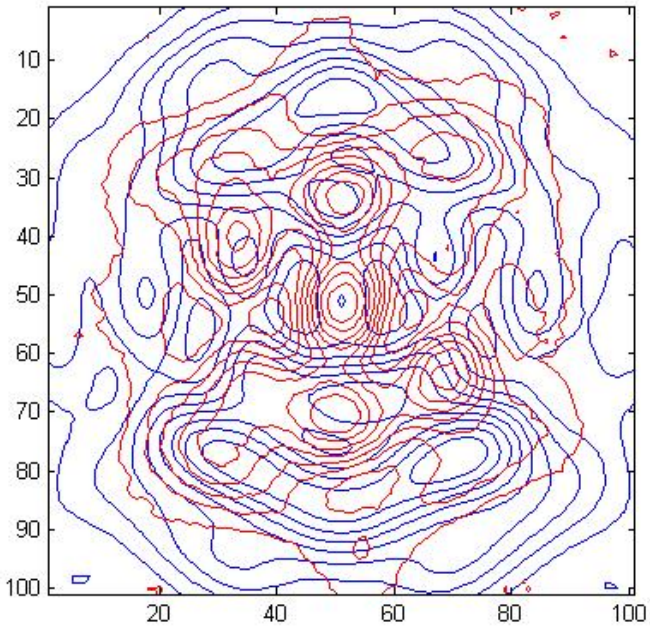

Figure 6.83: Contour plot of the image: red is reference and blue is observed

6.3 FFDP under space conditions analysis

The following section will show the analysis realized on the FFDP taken during thermo-vacuum tests of the prism No°54 and 51. All the tests have been performed following the methods and the rules explained in the previous chapters. All the tests performed on CCRs can be summarized as follows:

- CCR Test: prism is tested not in vacuum and the comparison is between FFDP inside and outside the chamber. Usually this test is performed before starting a new test.

- Deep-Space Test: prism is tested in deep space conditions. It is mounted in a breadboard, usually heated in a range that goes from 80°C up to 150°C while the walls of the chamber are at -192°C. It allows to detect changes in FFDPs caused by thermal expansion of the prism inside the breadboard.

- Sun Test: prism is mounted inside the breadboard and it is exposed directly to the light of sun simulator. Walls of the chamber are at -192°C. It allows to detect changes in FFDPs caused by thermal expansion of the prism inside the breadboard.

- Screw Test: the mounting screws of the breadboard are fastened at different level of torque, to detect if some structural deformations coming from the mounting system affect the FFDP. Usually the test is performed not in vacuum and the reference is at 0 Nm torque of the screws.

The tests will be shown divided by data and number of CCR under test. As for the previous section the calibration pattern, realized using a double slit

screen and in the same conditions described above. During the whole Ph.D. experience a great number of test in simulated space environment have been realized and here only the most significant will be shown. Obviously some of the test has been performed in order to investigate on all unexpected behaviors discovered during the results analysis. As made above for the optical tests in air the calibration pattern obtained from the double slit screen will be shown: even if on the external fringes seems there some problems of correlation, in the middle part there is a good matching of the curves: this effects may have been caused by the mirror employed for the double slit pattern, that resulted to be not of good optical quality ($< labmda/8$)). The results are the following:

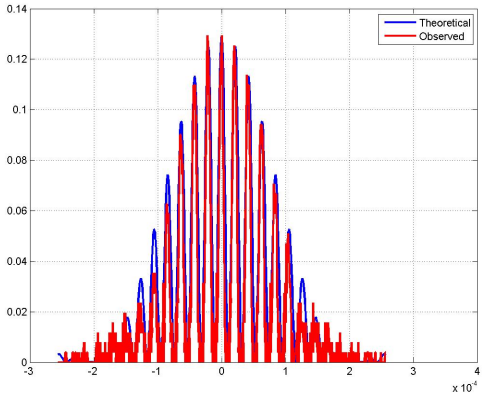

Figure 6.84: Comparison between calculated and observed calibration curves.

The coefficient calculated for the conversion of pixels-to-microradians is:

$$\frac{\mu rad}{pixels} = 1.6370$$

About the camera settings, most of the photos has been taken with:

$$ISO = 100 \div 200 \quad (6.3)$$

$$Exp = 1/500 \quad (6.4)$$

The double value of the ISO comes form the changes made in camera setting during the tests. Some changes have been made also in laser power. In these results the annulus analysis has been included, according to all the calculation made for velocity aberration and the thickness of the annulus. Hence these analyses will show also the effects of possible deformation of the prism caused by space conditions on the returning signal. The aim of annulus analysis is to detect if there will be some possible changes in the spreading of the energy coming form the CCRs mounted on LARES: obviously in case of strong effects there will be some possibilities that ground station will miss the returning signal, losing the tracking of the satellite. Anyway all the results have to be evaluated considering that laser arriving on the earth form LARES CCRs has a magnitude stronger than the one coming from other laser ranged satellite (i.e. 1000 times stronger that laser coming from LAGEOS 1 and 2).

6.4 CCR No°54 - Test of 30/03/2011 - CCR Test

With prism No°54 the first tests has been performed. In this section the FFDPs shown has been taken with a temporary configuration of optical table and hence the quality of the images is not sufficient. The noise introduced by the camera is clearly visible in all the photos and it affects mainly the morphological analysis. As shown in the results the contours detection has to be considered not valid. The results will be shown so all the changes

in the configuration of optical table will results more clear. The following results are coming from a simple test in air, comparing the FFDP taken inside and outside the thermo-vacuum chamber. The aim of the test was to detect some possible effects introduced by the optical window mounted on the chamber. Unfortunately, the high noise level was not helpful to detect small changes. Photos has been taken for all the three edges of No°54 prism, and the reference considered is the FFDP taken inside the chamber. All the patterns has been taken with laser power settled at 18.5 mA. Camera settings are:

$$ISO = 200 \tag{6.5}$$

$$Exp = 500 \tag{6.6}$$

The results are the following:

6.4.1 Edge 1 up

(a) Reference (b) Observed

Figure 6.85: Reference and Observed Image

	Values
Root Mean Square Error (%)	6.0195
Maximum Difference	0.2485
Average Difference	0.0180
Normalize Absolute Error	0.1319
Normalized Cross Correlation	1.0134
Peak Signal to Noise Ratio	40.3352
WC X Difference (pxs)	5
WC Y Difference (pxs)	0

Figure 6.86: Table of quality indexes

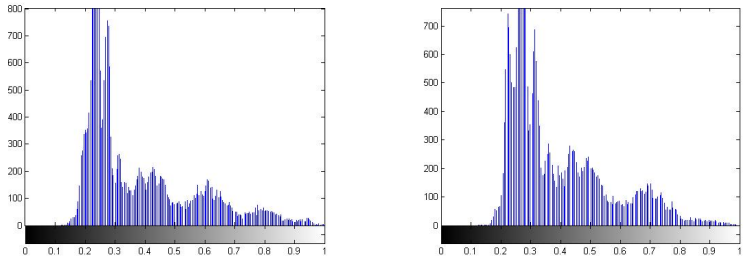

(a) Theoretical (b) Observed

Figure 6.87: Histogram of Images: reference and observed

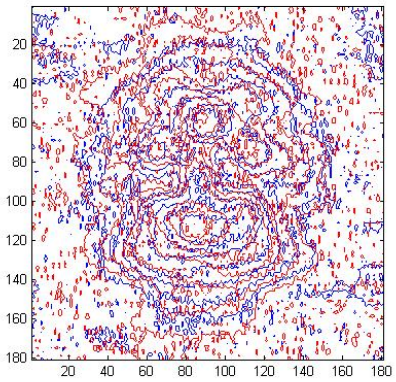

Figure 6.88: Contour plot of the image: red is reference and blue is observed

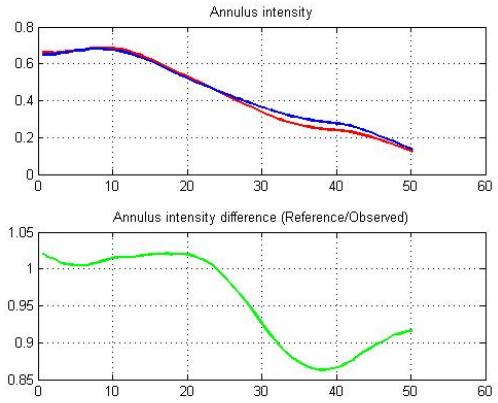

Figure 6.89: Annulus analysis: red is reference, blue is observed, green is the ratio

6.4.2 Edge 2 up

(a) Reference (b) Observed

Figure 6.90: Reference and Observed Image

	Values
Root Mean Square Error (%)	8.2897
Maximum Difference	0.5289
Average Difference	0.0327
Normalize Absolute Error	0.1486
Normalized Cross Correlation	0.8824
Peak Signal to Noise Ratio	38.9454
WC X Difference (pxs)	0
WC Y Difference (pxs)	0

Figure 6.91: Table of quality indexes

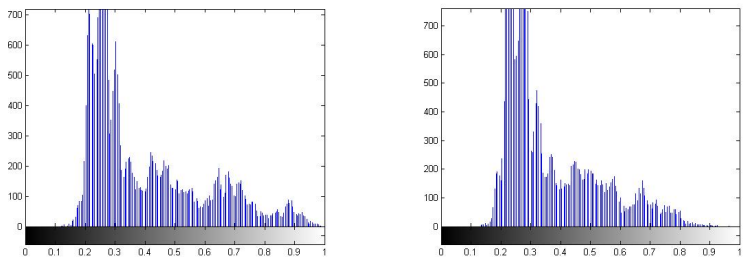

(a) Theoretical (b) Observed

Figure 6.92: Histogram of Images: reference and observed

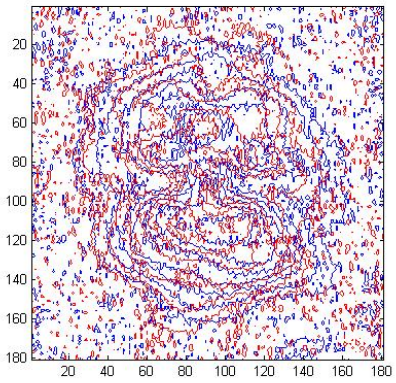

Figure 6.93: Contour plot of the image: red is reference and blue is observed

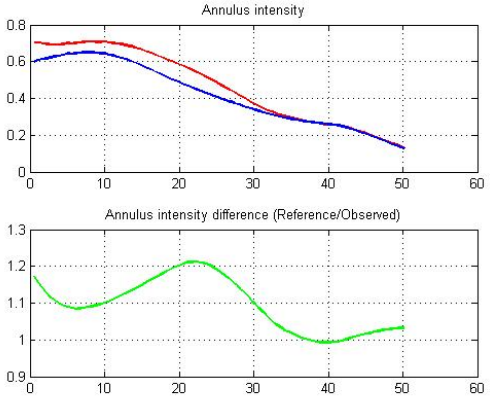

Figure 6.94: Annulus analysis: red is reference, blue is observed, green is the ratio

6.4.3 Edge 3 up

(a) Reference (b) Observed

Figure 6.95: Reference and Observed Image

	Values
Root Mean Square Error (%)	6.7779
Maximum Difference	0.3548
Average Difference	0.0018
Normalize Absolute Error	0.1447
Normalized Cross Correlation	0.9632
Peak Signal to Noise Ratio	39.8198
WC X Difference (pxs)	2
WC Y Difference (pxs)	0

Figure 6.96: Table of quality indexes

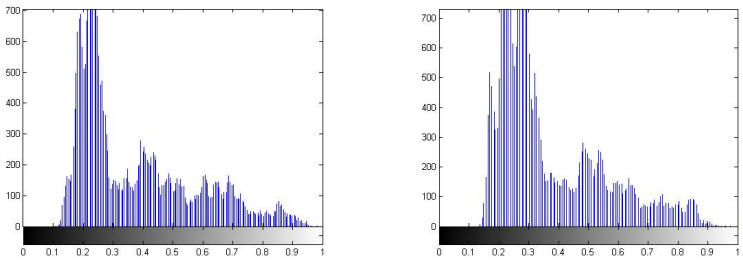

(a) Theoretical (b) Observed

Figure 6.97: Histogram of Images: reference and observed

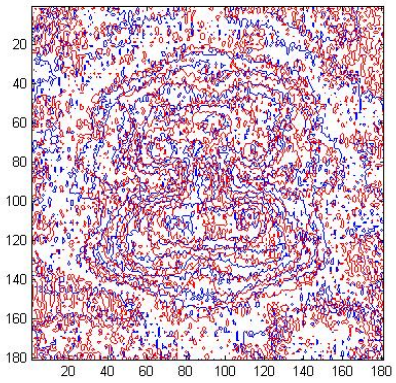

Figure 6.98: Contour plot of the image: red is reference and blue is observed

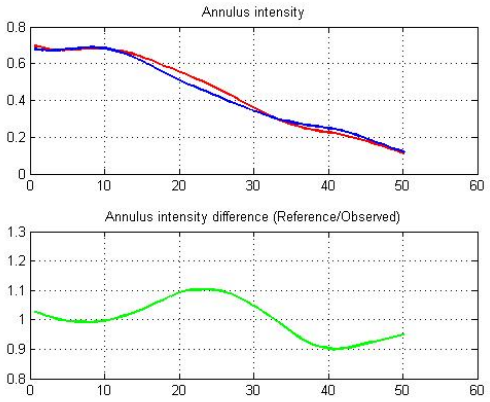

Figure 6.99: Annulus analysis: red is reference, blue is observed, green is the ratio

As specified above, reference is the FFDP taken with the CCR inside the chamber and the comparison term is an FFDP taken outside. It is clear that the morphological analysis is useless, but quality factors seems to have acceptable values: this can be explained because images are treated as matrix, so in mathematical form and, if the noise affecting the images is introduced

by the camera or other fixed devices (like lens or other) it is considered as a bias and images became comparable. Hence RMS error between figures is under 10% and it is probably caused by a small misalignment between the figures, because outside of the chamber breadboard has been positioned on a hand made support obtained cutting some aluminium profiles. Annulus analysis, realized just to make a test, show a signal increased by 10%. Because of the high background noise, has been impossible in these tests to check the introduction of any kind of effect from the optical window. Obviously other tests have been performed to verify the same effects and some of them will be discussed further. Anyway, even if from these results is not demonstrated, optical window of the thermo-vacuum chamber introduces in the FFDP some small effects that could be considered negligible.

6.5 CCR No°54 - Test of 30/03/2011 - Deep-Space Test

After the definitive re-arrangement of the optical table the first tests in deep space condition have been performed: after these tests some changes in executive procedures and way of analyze FFDP have been applied in the later experiences. For example the observation of the strange shape of the FFDP taken during the test let us suppose a remarkable mechanical stress on the CCR, and after some other tests on the mounting system it has been noticed that the levels of nominal torque to impress to the screws of the mounting system has to be revisited. Just from this conclusions all the “screw tests” have been designed and then executed. Moreover, after the “sun test” that will be shown in the next section, it has been noticed that the errors in mounting CCRs with a torque higher than nominal level, if combined with

thermal stress causes strong deformations in FFDP. The reference pattern is a FFDP taken inside the chamber at 150°C, with no cooling system active. All the patterns have been taken with laser power at 18.5 mA. The settings of the camera are:

$$ISO = 100 \div 200 \tag{6.7}$$

$$Exp = 1/500 \tag{6.8}$$

The results are the following:

6.5.1 Deep-Space Test

(a) Reference (b) Observed

Figure 6.100: Reference and Observed Image

	Values
Root Mean Square Error (%)	27.1582
Maximum Difference	0.8013
Average Difference	0.0868
Normalize Absolute Error	0.3626
Normalized Cross Correlation	0.7851
Peak Signal to Noise Ratio	33.7918
WC X Difference (pxs)	7
WC Y Difference (pxs)	0

Figure 6.101: Table of quality indexes

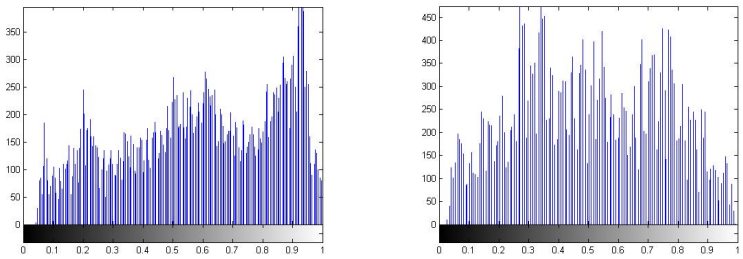

(a) Theoretical (b) Observed

Figure 6.102: Histogram of Images: reference and observed

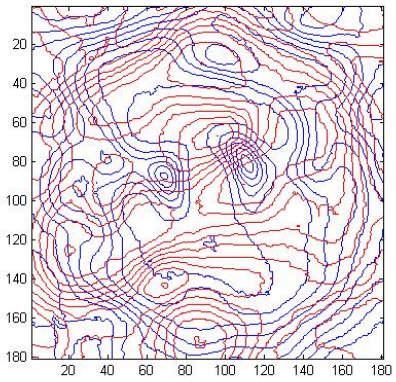

Figure 6.103: Contour plot of the image: red is reference and blue is observed

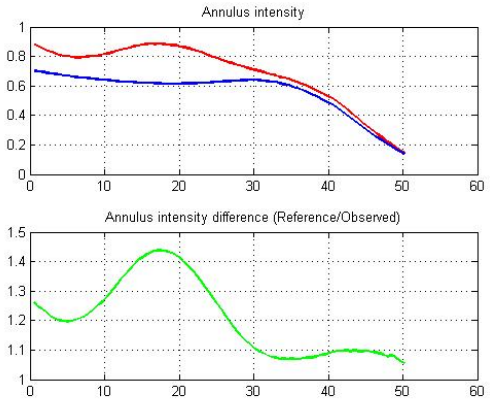

Figure 6.104: Annulus analysis: red is reference, blue is observed, green is the ratio

The results shown a deformed FFDP that is difficult to compare by eye to the reference: the difference of temperature between the two FFDP is around 300°C (reference is at 150°C and observed FFDP is at -192°C) and, obviously summing this stress to the mechanical ones, a deformed figure of diffraction is obtained. Anyway, even if the shape analysis don't give acceptable results, according to the table of quality factors and to the annulus analysis some results can be deduced: because the mechanical stress imposed on the breadboard and on the CCR remains the same from the beginning to the end of the test (if breadboard is mounted inside thermo-vacuum chamber it can't be touched until the test end) the thermal stress can be subtracted from annulus analysis: the RMS factor of about 30% corresponds to a reduction of the integrated energy in the annulus. So, if mechanical stress can be considered as a constant value in the whole test, the misalignment (7 pixels difference between the centroids of the two figures) and the thermal stress causes a reduction of the signal of about 10% in the range of interest.

6.5.2 Sun Test

As above a sun test has been performed in the same day of the previous test: to avoid to contaminate the breadboard and avoiding to repeat outgassing procedure or sensor gluing procedure, the CCR has been directed towards the sun simulator and, at the thermal equilibrium, some FFDP have been taken. As for the previous case a constant mechanical stress in the whole experience must be considered. The reference remains the same as above: it is a diffraction figure taken with the breadboard 150°C without cooling system active. It is possible to notice by eyes a FFDP with stronger differences from the reference than in the previous test: this is probably due to the direct exposition to the sun of the front face of the CCR. All the patterns has been taken with laser power at 18.5 mA. The settings of the camera are:

$$ISO = 100 \div 200 \tag{6.9}$$

$$Exp = 1/500 \tag{6.10}$$

The results are the following:

(a) Reference (b) Observed

Figure 6.105: Reference and Observed Image

	Values
Root Mean Square Error (%)	28.1507
Maximum Difference	0.7795
Average Difference	0.1664
Normalize Absolute Error	0.3672
Normalized Cross Correlation	0.7223
Peak Signal to Noise Ratio	33.6359
WC X Difference (pxs)	27
WC Y Difference (pxs)	0

Figure 6.106: Table of quality indexes

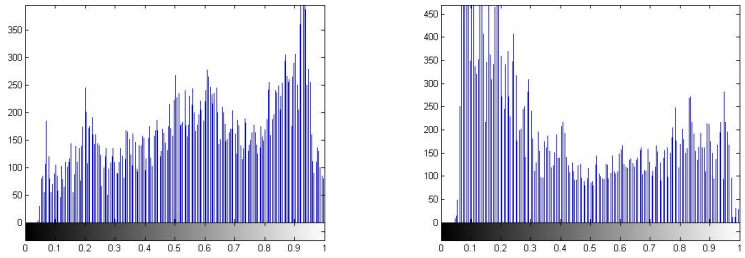

(a) Theoretical (b) Observed

Figure 6.107: Histogram of Images: reference and observed

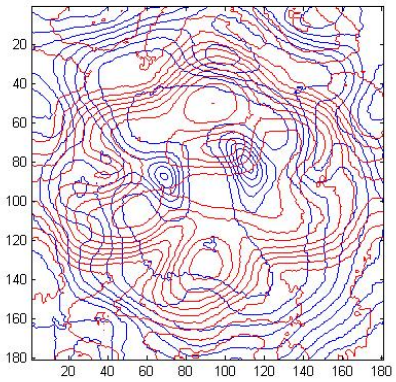

Figure 6.108: Contour plot of the image: red is reference and blue is observed

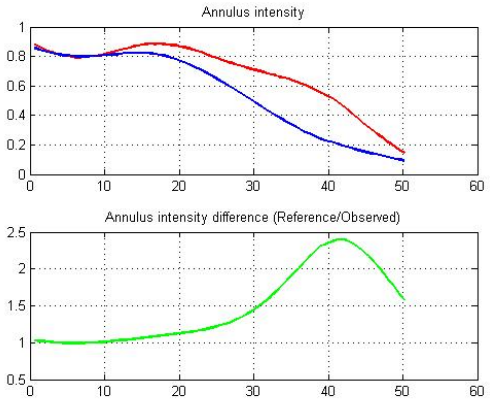

Figure 6.109: Annulus analysis: red is reference, blue is observed, green is the ratio

Results from the analysis of the patterns are similar to the previous ones, also because, as described above, these two tests have been performed one after the other without removing the breadboard from the support inside the chamber. The FFDP under analysis seems to be smaller than the reference: this is probably due to an additional mechanical deformation of the CCR introduced by the direct exposition to the sun simulator. To have a FFDP reduced in shape, the new deformations probably have affected the back-faces of the CCR, modifying the dihedral angle offset of the prism. Obviously the comparison between reference and test FFDP gives results worst than in the previous test: the RMS error increases of some percentage points and in the annulus analysis there is a greater loss of energy as the annulus expands form the center. This was an expected effect because of the shrinking of the FFDP. After the tests, during the disassembly of the prism, an excessive torque applied on the screws has been effectively noticed. So as described above, just from these tests, some ideas to verify also the effects of the mounting system on the prism has come.

6.6 CCR No°54 - Test of 01/04/2011 - Screw Test

In this section the results coming from the validation of the mounting tests will be shown. All the tests have been performed in air in order to detect only the effects coming from a wrong mounting procedure. In order to measure the mechanical stress coming form the previous experience, this tests have been realized employing the same breadboard, the same CCR and the same mounting system of deep space and sun test described above. All the FFDP have been taken in air, without testing breadboard in simulated space condition. The reference is a FFDP taken at near zero torque level: all the others FFDP have been taken mounting the breadboard by hand on the aluminium support out of the chamber. It has to be noticed that from LARES assembly procedures the nominal torque has to be in a range from $0.6 \div 0.8$ Nm: the tests has been performed up to $1 \div 1.5 Nm$. All the patterns has been taken with laser power at 18.5 mA. The settings of the camera are:

$$ISO = 100 \tag{6.11}$$

$$Exp = 1/500 \tag{6.12}$$

The results are the following:

6.6.1 Screw Test - 0.6 Nm

(a) Reference (b) Observed

Figure 6.110: Reference and Observed Image

	Values
Root Mean Square Error (%)	31.1710
Maximum Difference	0.8029
Average Difference	0.1498
Normalize Absolute Error	0.6266
Normalized Cross Correlation	1.0225
Peak Signal to Noise Ratio	33.1933
WC X Difference (pxs)	22
WC Y Difference (pxs)	0

Figure 6.111: Table of quality indexes

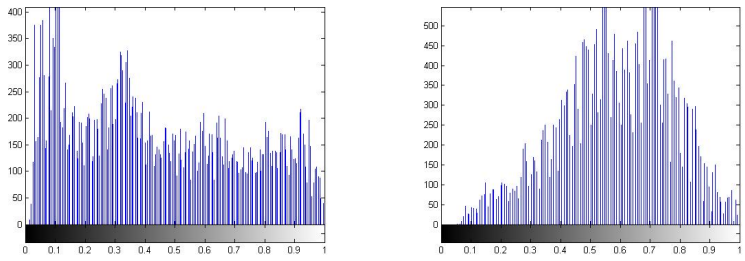

(a) Theoretical (b) Observed

Figure 6.112: Histogram of Images: reference and observed

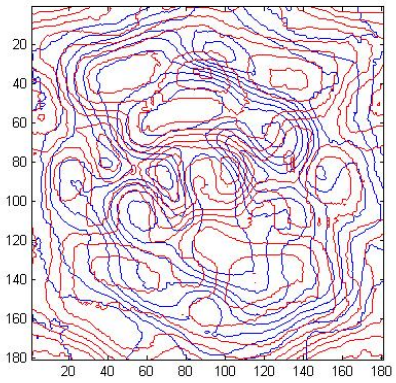

Figure 6.113: Contour plot of the image: red is reference and blue is observed

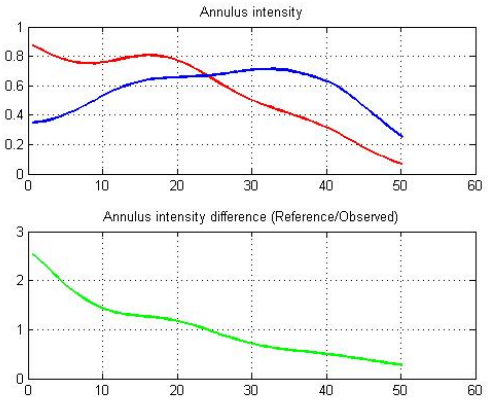

Figure 6.114: Annulus analysis: red is reference, blue is observed, green is the ratio

6.6.2 Screw Test - 0.8 Nm

(a) Reference (b) Observed

Figure 6.115: Reference and Observed Image

	Values
Root Mean Square Error (%)	35.6436
Maximum Difference	0.8762
Average Difference	0.1432
Normalize Absolute Error	0.7295
Normalized Cross Correlation	0.9532
Peak Signal to Noise Ratio	32.6110
WC X Difference (pxs)	30
WC Y Difference (pxs)	0

Figure 6.116: Table of quality indexes

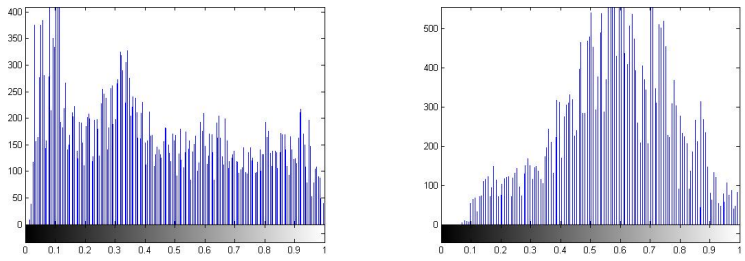

(a) Theoretical (b) Observed

Figure 6.117: Histogram of Images: reference and observed

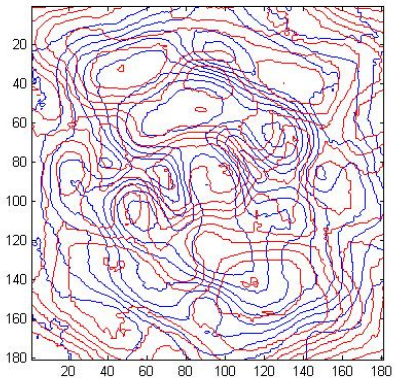

Figure 6.118: Contour plot of the image: red is reference and blue is observed

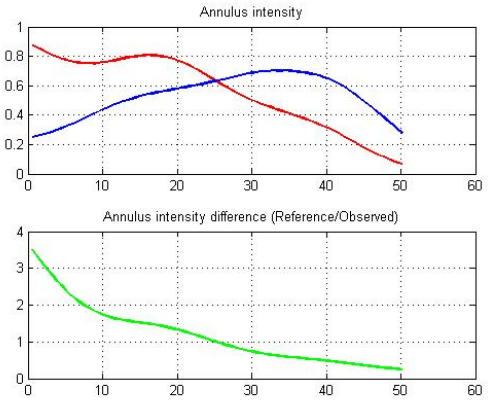

Figure 6.119: Annulus analysis: red is reference, blue is observed, green is the ratio

6.6.3 Screw Test - 1 Nm

(a) Reference (b) Observed

Figure 6.120: Reference and Observed Image

	Values
Root Mean Square Error (%)	36.4518
Maximum Difference	0.8650
Average Difference	0.1495
Normalize Absolute Error	0.7494
Normalized Cross Correlation	0.9560
Peak Signal to Noise Ratio	32.5136
WC X Difference (pxs)	30
WC Y Difference (pxs)	0

Figure 6.121: Table of quality indexes

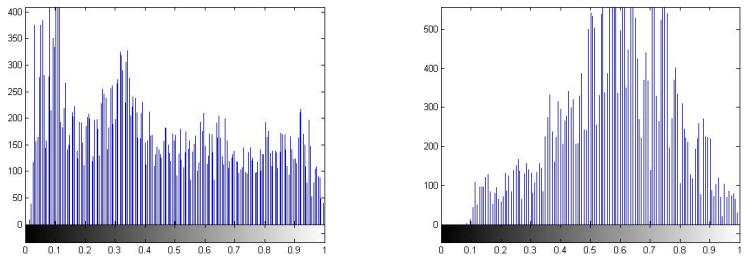

(a) Theoretical (b) Observed

Figure 6.122: Histogram of Images: reference and observed

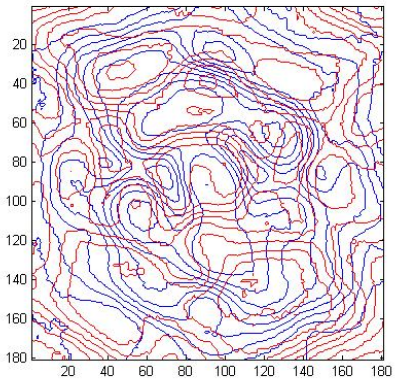

Figure 6.123: Contour plot of the image: red is reference and blue is observed

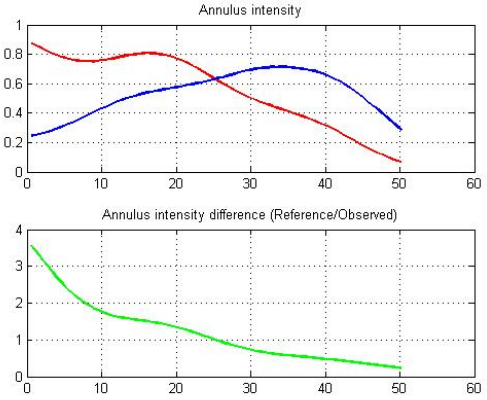

Figure 6.124: Annulus analysis: red is reference, blue is observed, green is the ratio

6.6.4 Screw Test - 1.5 Nm

(a) Reference (b) Observed

Figure 6.125: Reference and Observed Image

	Values
Root Mean Square Error (%)	35.5329
Maximum Difference	0.8765
Average Difference	0.1485
Normalize Absolute Error	0.7304
Normalized Cross Correlation	0.9639
Peak Signal to Noise Ratio	32.6245
WC X Difference (pxs)	30
WC Y Difference (pxs)	0

Figure 6.126: Table of quality indexes

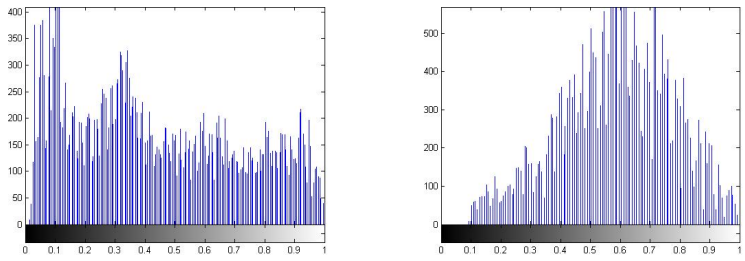

(a) Theoretical (b) Observed

Figure 6.127: Histogram of Images: reference and observed

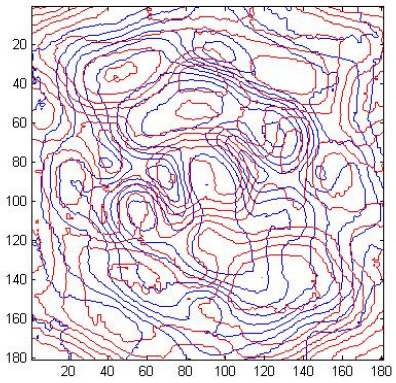

Figure 6.128: Contour plot of the image: red is reference and blue is observed

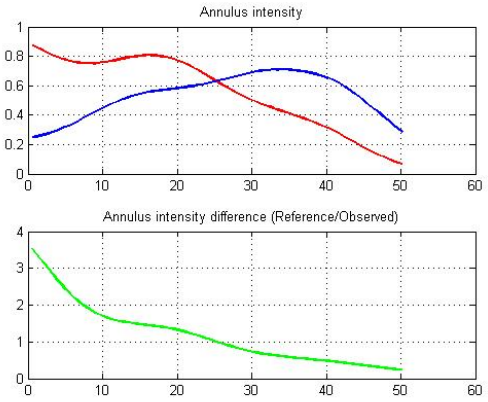

Figure 6.129: Annulus analysis: red is reference, blue is observed, green is the ratio

As it is shown in the results, there is no similarity between the reference and the observed patterns up to 1.5 Nm torque level: this can be due to possible residual deformations in the plastic rings and in the strong misalignment of the FFDP (the positioning has been done by hand). So from these tests no additional informations on the mechanical stress introduced on the CCR

have been obtained.

6.7 CCR No°51 - Test 04/04/2011 - Screw Test

A test similar to the previous one has been repeated with prism No°51: so, CCR, screws and plastic rings has been changed. Moreover more care has been taken in the mounting phases of the prism and in the positioning of the breadboard on the aluminium support. The reference is a FFDP taken in air with screws at full-travel stop. All the measurements has been repeated 6 times per each torque level, up to 1 Nm, changing also laser power and camera settings in each FFDP acquisition. All the FFDP analyzed are from the 3rd series of FFDP and they are taken with laser power at 17 mA. The settings of the camera are:

$$ISO = 200 \tag{6.13}$$

$$Exp = 1/500 \tag{6.14}$$

The results are the following:

6.7.1 Screw Test - 0.4 Nm

(a) Reference (b) Observed

Figure 6.130: Reference and Observed Image

	Values
Root Mean Square Error (%)	7.5296
Maximum Difference	0.2005
Average Difference	0.0062
Normalize Absolute Error	0.1248
Normalized Cross Correlation	1.0014
Peak Signal to Noise Ratio	39.3631
WC X Difference (pxs)	2
WC Y Difference (pxs)	0

Figure 6.131: Table of quality indexes

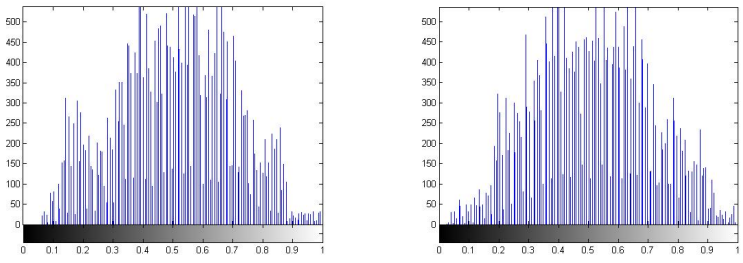

(a) Theoretical (b) Observed

Figure 6.132: Histogram of Images: reference and observed

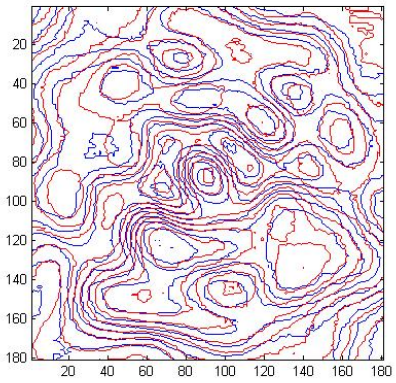

Figure 6.133: Contour plot of the image: red is reference and blue is observed

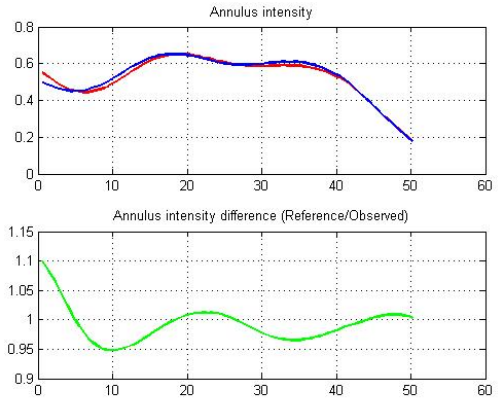

Figure 6.134: Annulus analysis: red is reference, blue is observed, green is the ratio

6.7.2 Screw Test - 0.6 Nm

(a) Reference (b) Observed

Figure 6.135: Reference and Observed Image

	Values
Root Mean Square Error (%)	9.2167
Maximum Difference	0.2481
Average Difference	0.0023
Normalize Absolute Error	0.1522
Normalized Cross Correlation	0.9967
Peak Signal to Noise Ratio	38.4850
WC X Difference (pxs)	1
WC Y Difference (pxs)	0

Figure 6.136: Table of quality indexes

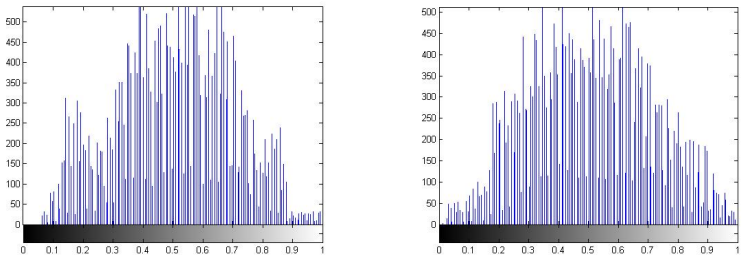

(a) Theoretical (b) Observed

Figure 6.137: Histogram of Images: reference and observed

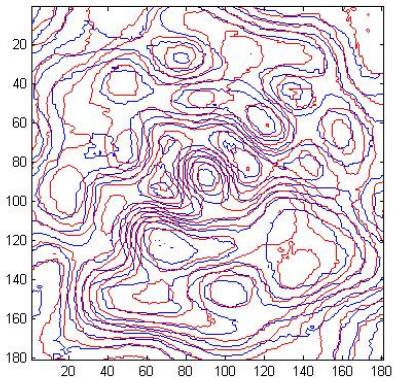

Figure 6.138: Contour plot of the image: red is reference and blue is observed

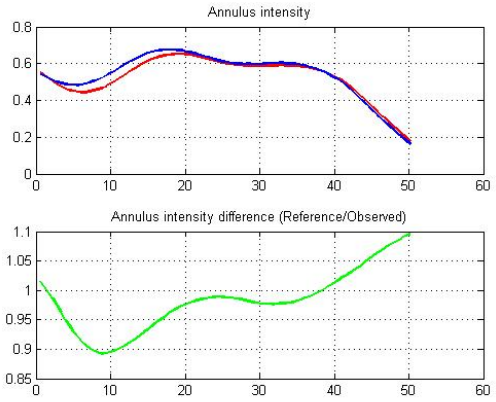

Figure 6.139: Annulus analysis: red is reference, blue is observed, green is the ratio

6.7.3 Screw Test - 0.8 Nm

(a) Reference (b) Observed

Figure 6.140: Reference and Observed Image

	Values
Root Mean Square Error (%)	9.9184
Maximum Difference	0.2412
Average Difference	0.0202
Normalize Absolute Error	0.1619
Normalized Cross Correlation	1.0210
Peak Signal to Noise Ratio	38.1664
WC X Difference (pxs)	4
WC Y Difference (pxs)	0

Figure 6.141: Table of quality indexes

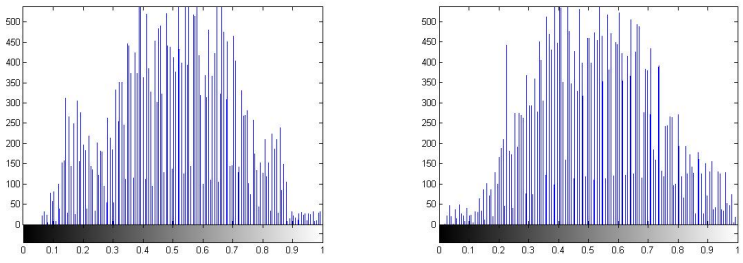

(a) Theoretical (b) Observed

Figure 6.142: Histogram of Images: reference and observed

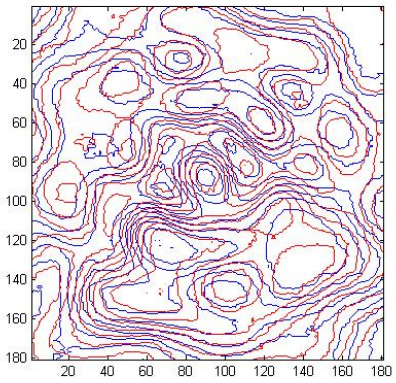

Figure 6.143: Contour plot of the image: red is reference and blue is observed

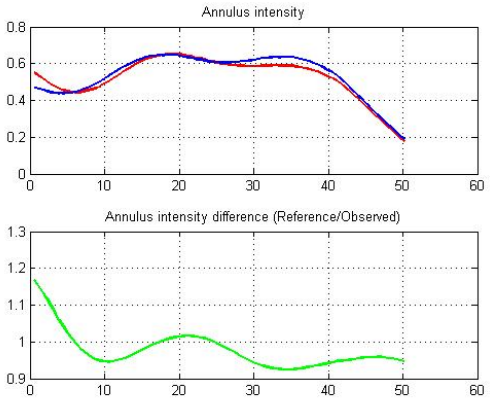

Figure 6.144: Annulus analysis: red is reference, blue is observed, green is the ratio

6.7.4 Screw Test - 1 Nm

(a) Reference (b) Observed

Figure 6.145: Reference and Observed Image

	Values
Root Mean Square Error (%)	12.5833
Maximum Difference	0.3734
Average Difference	0.0059
Normalize Absolute Error	0.2085
Normalized Cross Correlation	0.9754
Peak Signal to Noise Ratio	37.1329
WC X Difference (pxs)	5
WC Y Difference (pxs)	0

Figure 6.146: Table of quality indexes

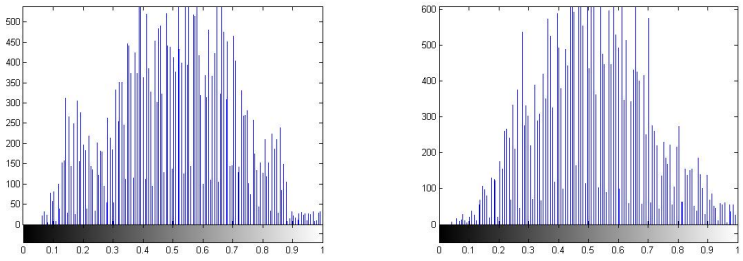

(a) Theoretical (b) Observed

Figure 6.147: Histogram of Images: reference and observed

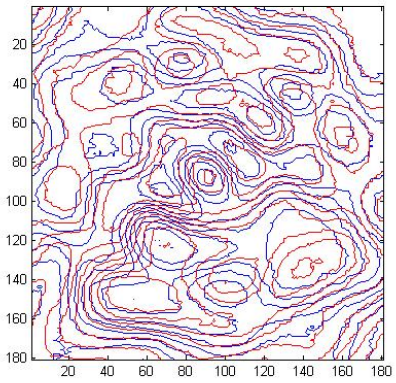

Figure 6.148: Contour plot of the image: red is reference and blue is observed

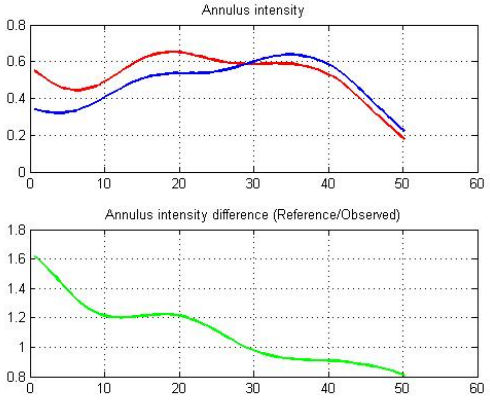

Figure 6.149: Annulus analysis: red is reference, blue is observed, green is the ratio

From the results in the quality factors, the misalignment between figures has been almost completely eliminated. This means that the analysis will give some results on the mechanical stress induced on the CCR without any other effect: morphological analysis reveals a very good similarity between the images and the RMS values follow a logical growth according to the

increasing torque level applied on the screws. The RMS factor increases of about $2 \div 3\%$ per each 0.2 Nm torque level applied and this corresponds to a difference of signal in the annulus analysis around $5 \div 10\%$. Because this effect has been quantified to be so small it will be considered negligible in the further analysis. Anyway to avoid any kind of problem deriving from a wrong torque application on the flight model of LARES the specification about mounting system has been changed fixing at 0.6 Nm the nominal torque level that has to be applied during the assembly of the CCRs.

6.8 CCR No°51 - Test 07/04/2011 - Complete Session

This session performed on No°51 in 07/04/2011 is composed by any kind of test mentioned above. In this case the reference is a FFDP taken inside of the chamber in vacuum but without imposing any thermal conditions. The torque level applied on the screws is 0.8 Nm, compliant with old flight specs. In this session all kind of tests have been preformed: first of all a simply comparison between FFDP taken outside and inside the chamber has been realized. Then a comparison with a FFDP taken at 150°C in vacuum condition has been performed. Then deep-space tests and sun tests have been performed. Results coming from these tests con be considered as the most significant of all the experiences shown: fixing the torque applied to the screws mechanical deformations can be considered constant during the whole experiment. Moreover the first comparison (CCR Test) fixes also the differences between external and vacuum condition. In few words, supposing that from the first test all the differences can be considered a constant value of the test, only effects coming form thermal stress applied to the CCR will

be noticed. Because of the great care taken on all the aspects mentioned above this test can be considered as a reference for the procedures to the other test performed.

6.8.1 CCR Test

(a) Reference (b) Observed

Figure 6.150: Reference and Observed Image

	Values
Root Mean Square Error (%)	17.7686
Maximum Difference	0.2325
Average Difference	0.1054
Normalize Absolute Error	0.2752
Normalized Cross Correlation	1.1348
Peak Signal to Noise Ratio	35.6343
WC X Difference (pxs)	7
WC Y Difference (pxs)	0

Figure 6.151: Table of quality indexes

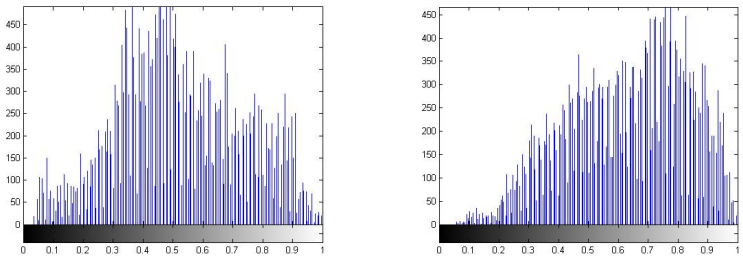

(a) Theoretical (b) Observed

Figure 6.152: Histogram of Images: reference and observed

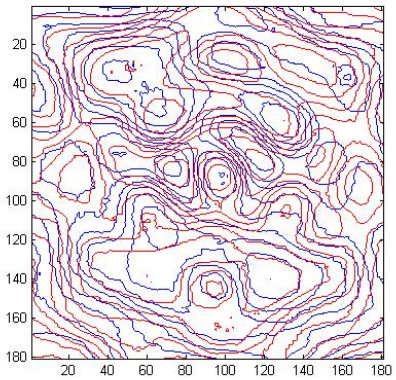

Figure 6.153: Contour plot of the image: red is reference and blue is observed

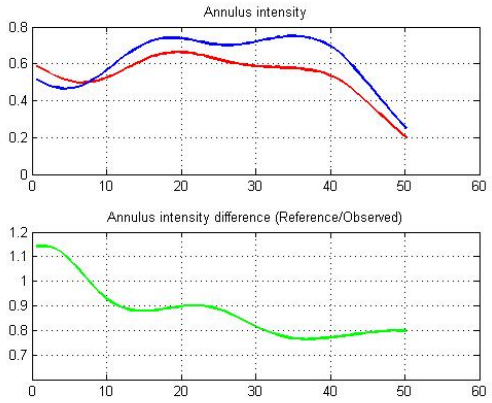

Figure 6.154: Annulus analysis: red is reference, blue is observed, green is the ratio

From the results the effects from the vacuum conditions and errors from possible misalignment or optical window can be easily detected: a difference in RMS error of about 18% is present. As discussed above these effects must be considered a constant for all the next tests. It has to be noticed that even if morphological analysis shows a good similarity between the FFDPs, the one taken in vacuum conditions seems to be expanded, from a geometrical point of view, if compared to the one taken in air. So there is a possibility to consider also a different value of magnification when FFDPs are taken in the chamber: as explained in the chapter regarding optical table, moving camera (or object under observation) along the optical axis some variations in magnifications can be detected if focusing is not very accurate. Because camera has been not equipped with micrometric slides the possibility that this effect is present is quite high: anyway this is a simple geometrical effect that can affect morphological analysis and the calculation of some of the quality factors. The annulus analysis shows an increasing of the integrated energy of about 20% between the two FFDP and these effects must be attributed to

test conditions.

6.8.2 CCR Test - 150°C

(a) Reference (b) Observed

Figure 6.155: Reference and Observed Image

	Values
Root Mean Square Error (%)	22.4900
Maximum Difference	0.5795
Average Difference	0.1487
Normalize Absolute Error	0.3626
Normalized Cross Correlation	0.7134
Peak Signal to Noise Ratio	34.6109
WC X Difference (pxs)	8
WC Y Difference (pxs)	0

Figure 6.156: Table of quality indexes

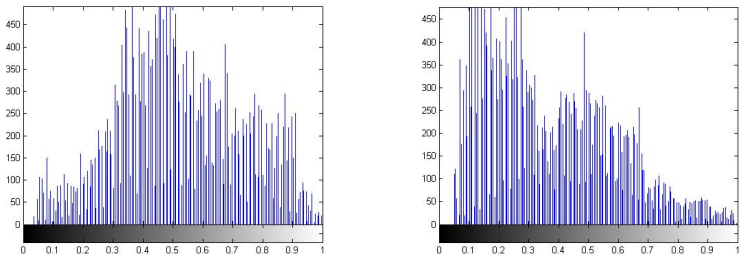

(a) Theoretical (b) Observed

Figure 6.157: Histogram of Images: reference and observed

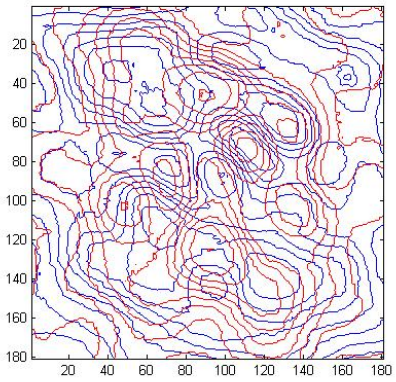

Figure 6.158: Contour plot of the image: red is reference and blue is observed

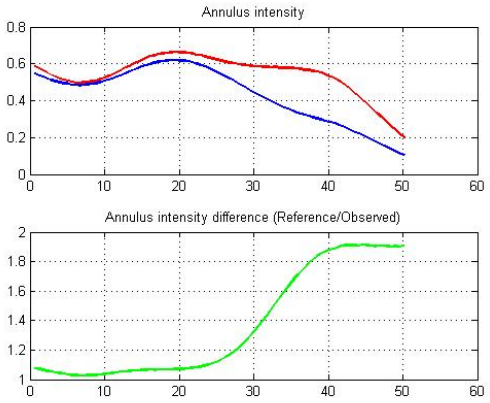

Figure 6.159: Annulus analysis: red is reference, blue is observed, green is the ratio

Increasing the temperature of the breadboard some other effects are added: the RMS error goes up to 22%. In this case the shroud is not supplied with liquid nitrogen, so that this test can be considered as the one with harder thermal conditions. As it is shown in the results FFDP changes his morphology: is seems to become more focused in the central region of the control surface. This modifications affects all the quality factors (+5% in RMS) and, as shown in the graph, the morphological analysis. The background noise level and the alignment are quite near to the values observed in the previous test: 35% Signal to Noise ratio and ¡10 pixels difference between centroids. The annulus analysis shows a remarkable reduction of the signal: from the curves shown seems that in the range of interest integrated energy is softened of about 0.8 times in respect to the reference FFDP. Subtracting from these effects the others described in the previous test it is possible to say that the reduction is around 0.5 times in respect to the reference.

6.8.3 Deep-Space Test

(a) Reference (b) Observed

Figure 6.160: Reference and Observed Image

	Values
Root Mean Square Error (%)	20.5836
Maximum Difference	0.5566
Average Difference	0.1274
Normalize Absolute Error	0.3277
Normalized Cross Correlation	0.7519
Peak Signal to Noise Ratio	34.9956
WC X Difference (pxs)	6
WC Y Difference (pxs)	0

Figure 6.161: Table of quality indexes

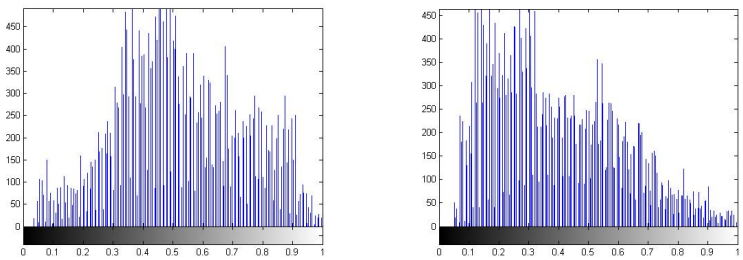

(a) Theoretical (b) Observed

Figure 6.162: Histogram of Images: reference and observed

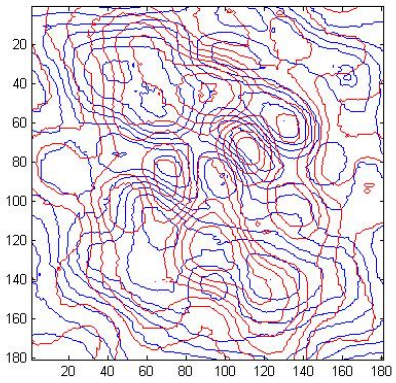

Figure 6.163: Contour plot of the image: red is reference and blue is observed

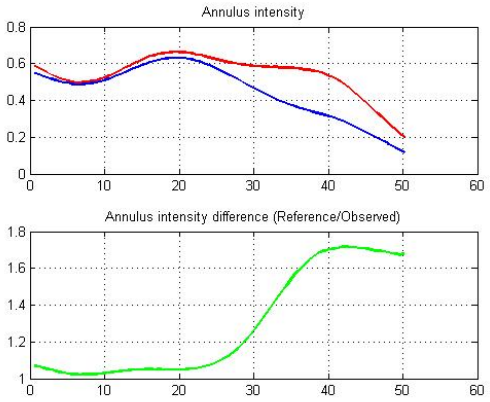

Figure 6.164: Annulus analysis: red is reference, blue is observed, green is the ratio

In this test the effects of the shroud must be added to the test: from the results the RMS error decrease of about 2%, because of the mitigation of thermal condition imposed on the prism: obviously thermal stress is reduced from the previous condition because CCR is exposed to the shroud plate which temperature is about -190°C. So the FFDP results to be less concen-

trated in the middle than in the previous test, but this not means that it goes nearer to the initial conditions: morphological analysis shows a stronger deformation in the upper right part of the control surface, probably due to a local deformation on one of the faces of the CCR. From the annulus analysis the reduction of the signal results to be minus than 1.5 times the original value – subtracting initial bias –: this was an expected result because of the mitigation of thermal stress as described before.

6.8.4 Sun Test

(a) Reference (b) Observed

Figure 6.165: Reference and Observed Image

	Values
Root Mean Square Error (%)	17.3211
Maximum Difference	0.5430
Average Difference	0.1001
Normalize Absolute Error	0.2675
Normalized Cross Correlation	0.7946
Peak Signal to Noise Ratio	35.7450
WC X Difference (pxs)	2
WC Y Difference (pxs)	0

Figure 6.166: Table of quality indexes

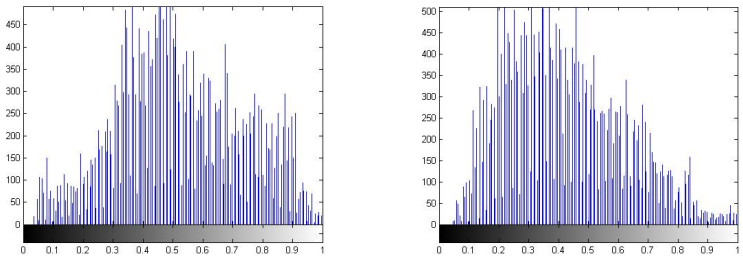

(a) Theoretical (b) Observed

Figure 6.167: Histogram of Images: reference and observed

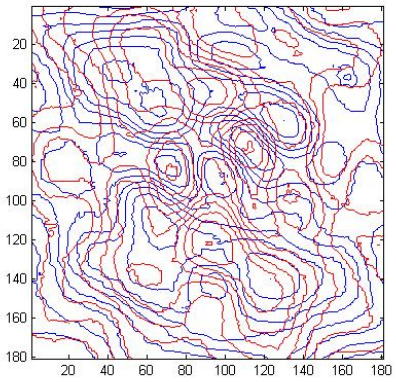

Figure 6.168: Contour plot of the image: red is reference and blue is observed

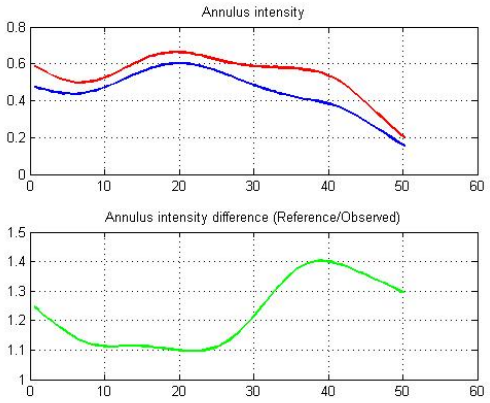

Figure 6.169: Annulus analysis: red is reference, blue is observed, green is the ratio

With the sun simulator active the RMS error decrease of about 5% from the previous test. The reason of the decreasing RMS error can probably come from the long time elapsed in waiting for the steady state temperature of the breadboard exposed to the sun light. So quality factors seems to be better than in the previous tests. Hence seems that the influence of deep space condition and direct sun light condition can be considered as a negligible effect on the FFDP.

Chapter 7

Conclusions

In this work the procedure of qualification and validation od CCRs of LARES satellite has been performed. Results obtained allow to assert that the devices under test are able to work properly even in a temperature range higher than the one calculated and declared in the thermal simulation made by the manufacturer of the satellite. The whole work has been performed in a special thermo-vacuum chamber settled up in 2010 in "La Sapienza - Università di Roma".

Appendix A

Optical Aberration

The term "aberration" implies any difference between the optical characteristic of an object an the characteristics of its image, produced by an optical system. So *aberrations* means properly any flaw of the lenses. Anyway often the term aberration is applied also to all the accidental errors, or of manufacturing or employing of the lenses, or also to all the effects linked to the wave theory of the light.

A.1 Spherical Aberration

Spherical aberration occurs when the refraction of light rays that strike a lens increase or when occurs a reflection of light rays when they hit a mirror near its edge, in comparison with those that hit nearer the center. It signifies a deviation of the device from the norm, so it results in an imperfection of the produced image. Spherical aberration should not be confused with barrel distortion; whereas barrel distortion affects the shape of the image, spherical aberration affects its sharpness. In a more practical way, if we put a lamp behind A lens and then we see its image on a white screen we will not see a

sharp image, but it will be a ring around the filament of the lamp: the rays near the axis of the lens (*paraxial*) create a partial image in the focus, while the rays far from the axis of the lens (*marginal*) not focalize on the same plane and then create a faded ring around the image. So even if the screen is moved nearer or further the lens the image is not clear, because in the first case paraxial rays deform image, and in the second case the same effect is introduced by the marginal rays. So "Positive" spherical aberration means peripheral rays are bent too much. "Negative" spherical aberration means peripheral rays are not bent enough.

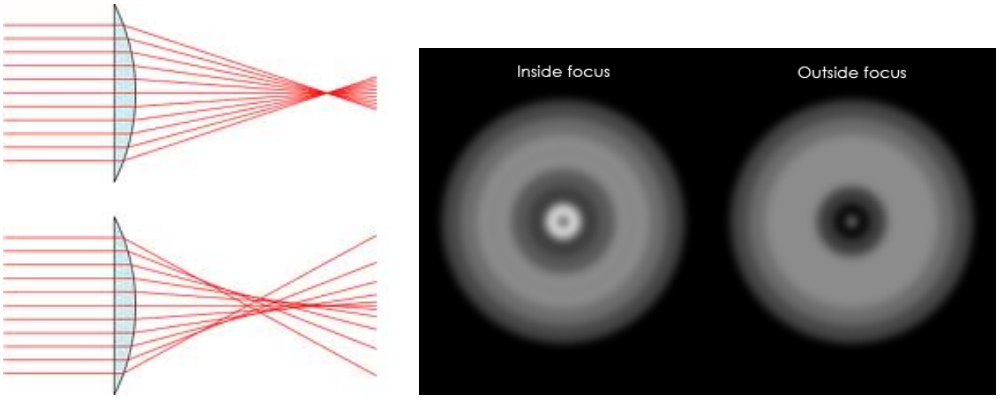

Figure A.1: Spherical Aberration: Optical diagram and example

A.2 Chromatic Aberration

In optics, chromatic aberration (also called achromatism or chromatic distortion, or simply CA) is a type of distortion in which there is a failure of a lens to focus all colors to the same convergence point. It occurs because lenses have a different refractive index for different wavelengths of light (the dispersion of the lens). The refractive index decreases with increasing wavelength.

Chromatic aberration can be both axial (longitudinal), in that different wavelengths are focused at a different distance from the lens, in different points on the optical axis (focus shift); and transverse (lateral), in that different wavelengths are focused at different positions in the focal plane (because the magnification and/or distortion of the lens also varies with wavelength; indicated in graphs as change in focus length). The acronym LCA is used, but ambiguous, and may refer to either longitudinal or lateral CA; for clarity, this article uses "axial" (shift in the direction of the optical axis) and "transverse" (shift perpendicular to the optical axis). These two types have different characteristics, and may occur together. Axial CA occurs throughout the image, and is reduced by stopping down the light (this increases depth of field, so though the different wavelength focus at different distances, they are still in acceptable focus). Transverse CA does not occur in the center, and increases towards the edge, but is not affected by stopping down. To see practically an example of chromatic aberration is useful to employ a white light behind a lens. The image of the lamp will be probably similar to the ones seen with a simple lamp and spherical aberration. If we put a screen in the same direction of the rays, a little bit inclined with respect to the middle of the image it will be possible to see dispersion of the refraction index, that is the variations of the focal length with the variations of wavelength.

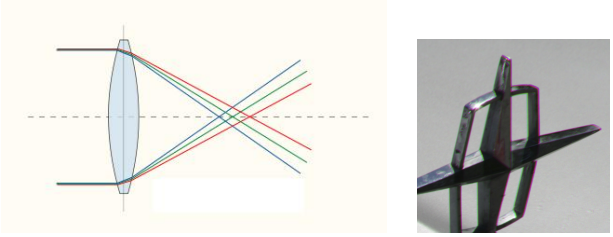

Figure A.2: Chromatic Aberration: Optical diagram and example

A.3 Coma

The coma (also called comatic aberration) in an optical system refers to the aberration inherent to certain optical designs or due to imperfection in the lens or other components which results in off-axis point sources such as stars appearing distorted, appearing to have a tail (coma) like a comet. Specifically, coma is defined as a variation in magnification over the entrance pupil. In refractive or diffractive optical systems, especially those imaging a wide spectral range, coma can be a function of wavelength, in which case it is a form of chromatic aberration. Coma is an inherent property of telescopes using parabolic mirrors. Light from a point source in the center of the field is perfectly focused at the focal point of the mirror (unlike a spherical mirror, where light from the outer part of the mirror focuses closer to the mirror than light from the center–spherical aberration). However, when the light source is off-center (off-axis), the different parts of the mirror do not reflect the light to the same point. This results in a point of light that is not in the center of the field looking wedge-shaped. The further off-axis, the worse this effect is. This causes stars, seen as a point source light, to appear to have a cometary coma, hence the name.

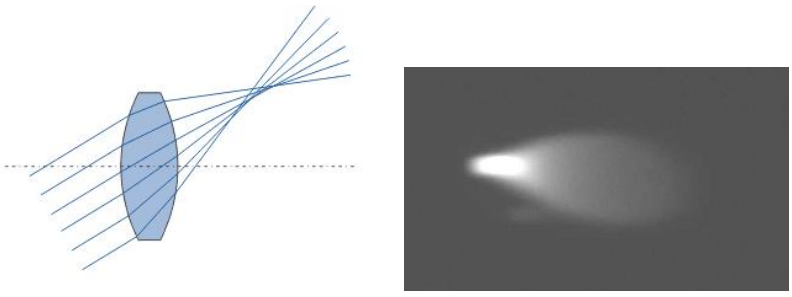

Figure A.3: Coma: Optical diagram and example

A.4 Astigmatism

An optical system with astigmatism is one where rays that propagate in two perpendicular planes have different foci. If an optical system with astigmatism is used to form an image of a cross, the vertical and horizontal lines will be in sharp focus at two different distances. There are two distinct forms of astigmatism. The first is a third-order aberration, which occurs for objects (or parts of objects) away from the optical axis. This form of aberration occurs even when the optical system is perfectly symmetrical. This is often referred to as a "monochromatic aberration", because it occurs even for light of a single wavelength. This terminology may be misleading, however, as the amount of aberration can vary strongly with wavelength in an optical system. The second form of astigmatism occurs when the optical system is not symmetric about the optical axis. This may be by design (as in the case of a cylindrical lens), or due to manufacturing errors in the surfaces of the components or misalignment of the components. In this case, astigmatism is observed even for rays from on-axis object points. In the analysis of this form of astigmatism, it is most common to consider rays from a given point on the object, which propagate in two special planes. The first plane is the tangential plane. This is the plane which includes both the object point being considered and the axis of symmetry. Rays that propagate in this plane are called tangential rays. Planes that include the optical axis are meridional planes. It is common to simplify problems in radially-symmetric optical systems by choosing object points in the vertical ("y") plane only. This plane is then sometimes referred to as the meridional plane. The second special plane is the sagittal plane. This is defined as the plane, orthogonal to the tangential plane, which contains the object point being considered and intersects the optical axis at the entrance pupil of the optical system. This plane

contains the chief ray, but does not contain the optic axis. It is therefore a skew plane, in other words not a meridional plane. Rays propagating in this plane are called sagittal rays. In third-order astigmatism, the sagittal and transverse rays form foci at different distances along the optic axis. These foci are called the sagittal focus and the transverse focus, respectively. In the presence of astigmatism, an off-axis point on the object is not sharply imaged by the optical system. Instead, sharp lines are formed at the sagittal and transverse foci. The image at the transverse focus is a short line, oriented in the direction of the sagittal plane; images of circles centered on the optic axis, or lines tangential to such circles, will be sharp in this plane. The image at the sagittal focus is a short line, oriented in the tangential direction; images of spokes radiating from the center are sharp at this focus. In between these two foci, a round but "blurry" image is formed. This is called the medial focus or circle of least confusion. This plane often represents the best compromise image location in a system with astigmatism. The amount of aberration due to astigmatism is proportional to the square of the angle between the rays from the object and the optical axis of the system. With care, an optical system can be designed to reduce or eliminate astigmatism. Such systems are called anastigmats.

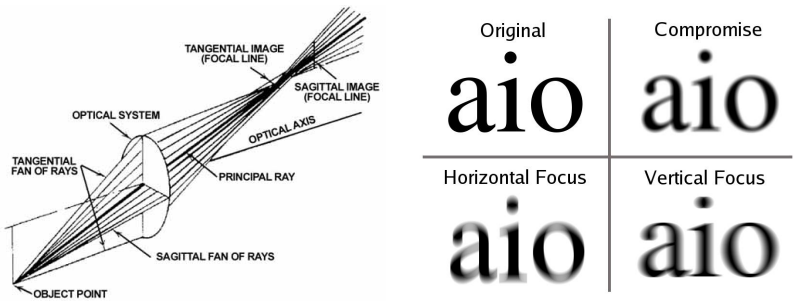

Figure A.4: Astigmatism: Optical diagram and example

Appendix B

Software

B.1 Software for Theoretical vs. Observed Patterns

```
clc, close all; clear all

%Calibration - Find the coefficient to transform microrad in pxs

I = imread('Calibration_new.bmp');

Max = max(max(I));

Image = im2single(I);

Dim = size(Image);

Middle = Image(Dim(1)/2,:,2);

x = 1:1:length(Middle);

d = 40;
a = 4;

lambda = 0.532*1e-3;
```

```
Fringes = [];
Envelope = [];

coeff = 0.1:0.001:0.170;

for j = 1:1:length(coeff)

    c = (pi/(180*3600))*coeff(j);

    alpha = (x-length(Middle)*0.5)*c;

    for i = 1:length(alpha)

        F(i) = pi*(d/lambda)*alpha(i);
        E(i) = pi*(a/lambda)*alpha(i);

        Fringes(i) = (cos(F(i)))^2;

        if Fringes(i)<0
            Fringes(i) = -Fringes(i);
        end

        Envelope(i) = (sin(E(i))/E(i))^2;

        if Envelope(i)<0
            Envelope(i) = -Envelope(i);
        end

        if alpha(i) == 0
            Envelope(i) = 1;
        end

        Total(i) = Fringes(i)*Envelope(i);

        if Total(i)<0
            Total(i) = -Total(i);
        end

    end
```

```
    Scale = max(Middle)/max(Total);

    Tot = Total*Scale;

    Temp(j,:) = conv2(Middle,Tot,'same');

    M = max(Temp');

    [r,c] = find(M == max(M));

    max_coeff = coeff(c);

end

%Transform microrad in pxs

mrad2pxs = 1e-6*(180/pi)*3600*(1/max_coeff);

%Loading Reference and scale it on pxs

T = imread('total51_00_00.bmp');

Math_T = double(T);

S_T = sum(sum(Math_T));

Theoretical = mat2gray(Math_T);

T_corr = mat2gray(Math_T);

Dim_F = size(T_corr);

%Prova = round(Dim_F/4);

Scale = Dim_F*mrad2pxs;

for i = 1:Dim_F(1)

    for j = 1:Dim_F(2)

        X_T_vect(i,j) = (i*Math_T(i,j));
```

```
        Y_T_vect(i,j) = (j*Math_T(i,j));

    end

end

X_T = round(sum(sum(X_T_vect))/S_T);
Y_T = round(sum(sum(Y_T_vect))/S_T);

%Loading Observed and select the colour channel

Observed = imread('CCR51_00.jpg');

I_green = Observed(:,:,2);

Math_O = double(I_green);

Norm_math_O = (Math_O.*255)./max(max(Math_O));

I = mat2gray(Norm_math_O);

%Find position and center of the FFDP

I_BW = im2bw(I);

S_column = sum(I_BW,1);

S_row = sum(I_BW,2);

Index_Column = find(S_column);

Index_Row = find(S_row);

Coeff = [100 100];

Crop_corr = I(Index_Row(1)-Coeff(1):Index_Row(length(Index_Row))+Coeff(1)
      ,...
    Index_Column(1)-Coeff(2):Index_Column(length(Index_Column))+Coeff(2));

O_corr = imcomplement(Crop_corr);
I = imcomplement(Crop_corr);
```

```
Dim_O = size(O_corr);

S_O = sum(sum(O_corr));

for i = 1:Dim_O(1)

    for j = 1:Dim_O(2)

        X_O_vect(i,j) = (i*O_corr(i,j));
        Y_O_vect(i,j) = (j*O_corr(i,j));

    end

end

X_O = round(sum(sum(X_O_vect))/S_O);
Y_O = round(sum(sum(Y_O_vect))/S_O);

Ratio = Dim_O./Dim_F;

Prova_X = X_T*Ratio(1);

Prova_Y = Y_T*Ratio(2);

Size_O_X = round(Prova_X-(Scale(1)/2):Prova_X+(Scale(1)/2));

Size_O_Y = round(Prova_Y-(Scale(2)/2):Prova_Y+(Scale(2)/2));

Crop = I(Size_O_X,Size_O_Y);

FFDP = imresize(Crop,Dim_F);

Dim_FFDP = size(FFDP);

S_FFDP = sum(sum(FFDP));

for i = 1:Dim_FFDP(1)

    for j = 1:Dim_FFDP(2)
```

```
            X_FFDP_vect(i,j) = (i*FFDP(i,j));
            Y_FFDP_vect(i,j) = (j*FFDP(i,j));

        end

    end

    X_FFDP = round(sum(sum(X_FFDP_vect))/S_FFDP);
    Y_FFDP = round(sum(sum(Y_FFDP_vect))/S_FFDP);

    %ANALISYS

    %Parameters

    Ref = Theoretical;
    Obs = FFDP;

    [M N] = size(Theoretical);
    Eps = Ref - Obs;

    %Root Mean Square Error

    RMSE = (sqrt(sum(sum(Eps.*Eps))/(M*N)))*100;

    %Maximum Difference & Average Difference

    MD = abs(max(max(Eps)));
    AD = abs(sum(sum(Eps))/(M*N));

    %Normalize Absolute Error

    NAE = sum(sum(abs(Eps)))/sum(sum(Ref));

    %Normalized Cross Correlation

    NCC = sum(sum(Ref.*Obs))/sum(sum(Ref.*Ref));

    %PSNR (Peak Signal to Noise Ratio)

    if(RMSE > 0)
        PSNR = 10*log(255*255/RMSE)/log(10);
```

```
else
    PSNR = 99;
end

%Centroid Difference

X_diff = abs(X_T-X_FFDP);
Y_diff = abs(Y_T-Y_FFDP);

%Figures

figure('Name','Theoretical','NumberTitle','off')
imshow(Theoretical)
hold on
plot(X_T,Y_T,'r.','MarkerSize',10)

figure('Name','Observed','NumberTitle','off')
imshow(FFDP)
hold on
plot(X_FFDP,Y_FFDP,'r.','MarkerSize',10)

figure('Name','Histogram Teoretical','NumberTitle','off')
imhist(Theoretical)

figure('Name','Histogram Observed','NumberTitle','off')
imhist(FFDP)
figure('Name','Contours','NumberTitle','off')
Q = imcontour(Theoretical,'b.');
hold on
R = imcontour(FFDP,'r-');

f = figure('Position',[1 1 390 180],'Name','Values','NumberTitle','off');
Data = [RMSE;MD;AD;NAE;NCC;PSNR;X_diff;Y_diff];
c_names = {'Values'};
r_names = {'Root Mean Square Error (%)','Maximum Difference','Average
      Difference',...
    'Normalize Absolute Error','Normalized Cross Correlation','Peak Signal
         to Noise Ratio',...
    'WC X Difference (pxs)','WC Y Difference (pxs)'};
t = uitable('Data',Data,'ColumnName',c_names,...
            'RowName',r_names,'Position',[3 3 400 175]);
```

B.2 Software for analysis of FFDP taken in Rome

```
clc, close all; clear all

tic

%Calibration - Find the coefficient to transform microrad in pxs

I = imread('Prova_red.bmp');

Max = max(max(I));

Image = im2single(I);

Dim = size(Image);

Middle = Image(Dim(1)/2,:,2);

x = 1:1:length(Middle);

d = 33;
a = 3;

lambda = 0.635*1e-3;

Fringes = [];
Envelope = [];

coeff = 0.1:0.001:0.170;

for j = 1:1:length(coeff)

    c = (pi/(180*3600))*coeff(j);

    alpha = (x-length(Middle)*0.5)*c;

    for i = 1:length(alpha)

        F(i) = pi*(d/lambda)*alpha(i);
```

```
        E(i) = pi*(a/lambda)*alpha(i);

        Fringes(i) = (cos(F(i)))^2;

        if Fringes(i)<0
            Fringes(i) = -Fringes(i);
        end

        Envelope(i) = (sin(E(i))/E(i))^2;

        if Envelope(i)<0
            Envelope(i) = -Envelope(i);
        end

        if alpha(i) == 0
            Envelope(i) = 1;
        end

        Total(i) = Fringes(i)*Envelope(i);

        if Total(i)<0
            Total(i) = -Total(i);
        end

    end

    Scale = max(Middle)/max(Total);

    Tot = Total*Scale;

    Temp(j,:) = conv2(Middle,Tot,'same');

    M = max(Temp');

    [r,c] = find(M == max(M));

    max_coeff = coeff(c);

end

%Transform microrad in pxs
```

```
mrad2pxs = 1e-6*(180/pi)*3600*(1/max_coeff);

Dim_image = [180 180];

% Loading Reference and select the colour channel

R = imread('IMG_0181.jpg');

R_red = R(:,:,1);

Math_R = double(R_red);

Norm_math_R = (Math_R.*255)./max(max(Math_R));

Gray_R = mat2gray(Norm_math_R);

% Loading Image and select the colour channel

O = imread('IMG_0281.jpg');

O_red = O(:,:,1);

Math_O = double(O_red);

Norm_math_O = (Math_O.*255)./max(max(Math_O));

Gray_O = mat2gray(Norm_math_O);

%Find position and center of the FFDP

R_BW = im2bw(Gray_R);
O_BW = im2bw(Gray_O);

S_column_R = sum(R_BW,1);
S_column_O = sum(O_BW,1);

S_row_R = sum(R_BW,2);
S_row_O = sum(O_BW,2);

Index_Column_R = find(S_column_R);
```

```
Index_Column_O = find(S_column_O);

Index_Row_R = find(S_row_R);
Index_Row_O = find(S_row_O);

Coeff = [100  100];

Crop_R = Gray_R(Index_Row_R(1)-Coeff(1):Index_Row_R(length(Index_Row_R))+
      Coeff(1),...
    Index_Column_R(1)-Coeff(2):Index_Column_R(length(Index_Column_R))+Coeff
         (2));
Crop_O = Gray_O(Index_Row_O(1)-Coeff(1):Index_Row_O(length(Index_Row_O))+
      Coeff(1),...
    Index_Column_O(1)-Coeff(2):Index_Column_O(length(Index_Column_O))+Coeff
         (2));

I_R = Crop_R;
I_O = Crop_O;

Dim_R = size(I_R);
Dim_O = size(I_O);

S_R = sum(sum(I_R));
S_O = sum(sum(I_O));

for i = 1:Dim_R(1)

    for j = 1:Dim_R(2)

        X_R_vect(i,j) = (i*I_R(i,j));
        Y_R_vect(i,j) = (j*I_R(i,j));

    end

end

for i = 1:Dim_O(1)

    for j = 1:Dim_O(2)

        X_O_vect(i,j) = (i*I_O(i,j));
```

```
        Y_O_vect(i,j) = (j*I_O(i,j));

    end

end

X_R = round(sum(sum(X_R_vect))/S_R);
Y_R = round(sum(sum(Y_R_vect))/S_R);
X_O = round(sum(sum(X_O_vect))/S_O);
Y_O = round(sum(sum(Y_O_vect))/S_O);

Size_R_X = round(X_R-(Dim_image(1)/2):X_R+(Dim_image(1)/2));
Size_R_Y = round(Y_R-(Dim_image(2)/2):Y_R+(Dim_image(2)/2));
Size_O_X = round(X_O-(Dim_image(1)/2):X_O+(Dim_image(1)/2));
Size_O_Y = round(Y_O-(Dim_image(2)/2):Y_O+(Dim_image(2)/2));

Reference = I_R(Size_R_X,Size_R_Y);
Observed = I_O(Size_O_X,Size_O_Y);

Dim_Ref = size(Reference);
Dim_Obs = size(Observed);

S_Ref = sum(sum(Reference));
S_Obs = sum(sum(Observed));

for i = 1:Dim_Ref(1)

    for j = 1:Dim_Ref(2)

        X_Ref_vect(i,j) = (i*Reference(i,j));
        Y_Ref_vect(i,j) = (j*Reference(i,j));

    end

end

X_Ref = round(sum(sum(X_Ref_vect))/S_Ref);
Y_Ref = round(sum(sum(Y_Ref_vect))/S_Ref);

for i = 1:Dim_Obs(1)
```

```
    for j = 1:Dim_Obs(2)

        X_Obs_vect(i,j) = (i*Observed(i,j));
        Y_Obs_vect(i,j) = (j*Observed(i,j));

    end

end

X_Obs = round(sum(sum(X_Obs_vect))/S_Obs);
Y_Obs = round(sum(sum(Y_Obs_vect))/S_Obs);

step = 0:.1:2*pi;

for i = 1:(Dim_Ref(1)/2)

    r_int = i-1;
    r_ext = r_int+19;

    Area = (2*pi*(r_ext^2))-(2*pi*(r_int^2));

    x_int_R(i,:) = round(r_int*cos(step) + X_Ref);
    y_int_R(i,:) = round(r_int*sin(step) + Y_Ref);

    x_ext_R(i,:) = round(r_ext*cos(step) + X_Ref);
    y_ext_R(i,:) = round(r_ext*sin(step) + Y_Ref);

    Mask_int_R(:,:,i) = roipoly(Reference,x_int_R(i,:),y_int_R(i,:));
    Mask_ext_R(:,:,i) = roipoly(Reference,x_ext_R(i,:),y_ext_R(i,:));

    Mask_R(:,:,i) =  Mask_ext_R(:,:,i)-Mask_int_R(:,:,i);

    [r_R c_R] = find(Mask_R(:,:,i));

    for j = 1:length(r_R)

        x_R = r_R(j);
        y_R = c_R(j);

        Sum_R(j,i) = Reference(x_R,y_R);
```

```
    end

    Ann_R(:,i) = sum(Sum_R(:,i))/Area;

    Visual_R(:,:,i) = Reference - imcomplement(Mask_R(:,:,i));

    x_int_O(i,:) = round(r_int*cos(step) + X_Obs);
    y_int_O(i,:) = round(r_int*sin(step) + Y_Obs);

    x_ext_O(i,:) = round(r_ext*cos(step) + X_Obs);
    y_ext_O(i,:) = round(r_ext*sin(step) + Y_Obs);

    Mask_int_O(:,:,i) = roipoly(Reference,x_int_O(i,:),y_int_O(i,:));
    Mask_ext_O(:,:,i) = roipoly(Reference,x_ext_O(i,:),y_ext_O(i,:));

    Mask_O(:,:,i) =  Mask_ext_O(:,:,i) - Mask_int_O(:,:,i);

    [r_O c_O] = find(Mask_O(:,:,i) == 1);

    for j = 1:length(r_O)

        x_O = r_O(j);
        y_O = c_O(j);

        Sum_O(j,i) = Reference(x_O,y_O);

    end

    Ann_O(:,i) = sum(Sum_O(:,i))/Area;

    Visual_O(:,:,i) = Observed - imcomplement(Mask_O(:,:,i));

end

%ANALISYS

%Parameters

Ref = Reference;
Obs = Observed;
```

```
[M N] = size(Reference);
Eps = Ref - Obs;

%Root Mean Square Error

RMSE = (sqrt(sum(sum(Eps.*Eps))/(M*N)))*100;

%Maximum Difference & Average Difference

MD = abs(max(max(Eps)));
AD = abs(sum(sum(Eps))/(M*N));

%Normalize Absolute Error

NAE = sum(sum(abs(Eps)))/sum(sum(Ref));

%Normalized Cross Correlation

NCC = sum(sum(Ref.*Obs))/sum(sum(Ref.*Ref));

%PSNR (Peak Signal to Noise Ratio)

if(RMSE > 0)
    PSNR = 10*log(255*255/RMSE)/log(10);
else
    PSNR = 99;
end

%Centroid Difference

X_diff = abs(X_R-X_O);
Y_diff = abs(Y_O-Y_O);

%Visualization

T = size(Visual_R);

Axis = (1:T(3))/mrad2pxs;

Diff = Ann_R./Ann_O;
```

```
for i = 1:T(3)

    figure(1)

    subplot(3,3,1);
    title('Reference')
    imshow(Visual_R(:,:,i));
    hold on

    subplot(3,3,2:3);
    plot(Axis,Ann_R,'r','linewidth',2);
    title('Annulus intensity (Reference)')
    grid on

    subplot(3,3,4);
    title('Observed')
    imshow(Visual_O(:,:,i));
    hold on

    subplot(3,3,5:6);
    plot(Axis,Ann_O,'b','linewidth',2);
    title('Annulus intensity (Observed)')
    grid on

    subplot(3,3,7:9)
    plot(Axis,Diff,'g','linewidth',2);
    title('Annulus intensity difference (Reference - Observed)')
    grid on

end

%Figures

figure('Name','Reference','NumberTitle','off')
imshow(Reference)
hold on
plot(X_Ref,Y_Ref,'r.','MarkerSize',10)

figure('Name','Observed','NumberTitle','off')
imshow(Observed)
hold on
```

```
plot(X_Obs,Y_Obs,'r.','MarkerSize',10)

figure('Name','Histogram Referenece','NumberTitle','off')
imhist(Reference)

figure('Name','Histogram Observed','NumberTitle','off')
imhist(Observed)
figure('Name','Contours','NumberTitle','off')
Q = imcontour(Reference,'b.');
hold on
R = imcontour(Observed,'r-');

f = figure('Position',[1 1 390 180],'Name','Values','NumberTitle','off');
Data = [RMSE;MD;AD;NAE;NCC;PSNR;X_diff;Y_diff];
c_names = {'Values'};
r_names = {'Root Mean Square Error (%)','Maximum Difference','Average
      Difference',...
    'Normalize Absolute Error','Normalized Cross Correlation','Peak Signal
         to Noise Ratio',...
    'WC X Difference (pxs)','WC Y Difference (pxs)'};
t = uitable('Data',Data,'ColumnName',c_names,...
            'RowName',r_names,'Position',[3 3 400 175]);

toc
```

Bibliography

[1] Arnold, D.A., Method of calculating retroreflector-array transfer functions, Smithsonian Astrophysical Observatory Special Report No. 382, 165 pp., 1979.

[2] Mathworks Support and Documentation on web: Matlab, Mathworks files exchange central, Image Acquisition Toolbox, Image Processing Toolbox, Signal Processing Toolbox.

[3] Wikipedia, the free enciclopedya.

[4] Làszlò Csink, Szabolcs Sergyàn *Color Histogram Normalization using Matlab and Applications in CBIR*, SSIP 2005, Szeged

[5] Rafael C. Gonzales, Richard E. Woods, Steve L. Eddins *Digital Image Processing Using MATLAB*, Gatesmark Publishing, 2003

[6] Alasdair McAndrew, *An Introduction to Digital Image Processing with Matlab*, Notes for SCM2511, Image Processing 1

[7] Daniele Spano, Report No°1, 24/06/2011

[8] Edwards website

[1] I. Ciufolini, A. Paolozzi, I. Peroni, A Preliminary Study for a Satellite Minimizing Solar Radiation Perturbations, Atti del XIV AIDAA Congress, (Oct. 1997 Naples, Italy) Vol. II, pp. 521-530

[2] I. Ciufolini, A. Paolozzi, I. Peroni, et al. (1998). LARES, Laser Relativity Satellite,for the study of the Earth gravitational field and general relativity measurement. Phase A report, studio piccole missioni ASI.

[3] I. Ciufolini, Measurement of the Lense-Thirring drag on high-altitude laser-ranged artificial satellites, Phys. Rev. Lett., 56, 278-281, 1986.

[4] I. Ciufolini, A. Paolozzi, I. Peroni, A. Gabrielli, A study for a laser-ranged relativity satellite, Applied Mechanics in the Americas, Proc. of the PACAM VI. (vol. 6, pp. 467-470).

[5] A. Paolozzi. (2002). A New Laser Ranged Satellite for Testing General Relativity. Ninth Marcel Grossmann Meeting on General Relativity. (pp. 1766-1770). Edited by V.G. Gurzadyan, R.T. Jantzen and R. Ruffini, published by World Scientific.

[6] I. Ciufolini, D.G. Currie, A. Paolozzi (2003). The LARES Mission for Testing the Dynamics of General Relativity. IEEE Aerospace Conference. March. Montana, USA.

[7] I. Ciufolini, A. Paolozzi. (1999). LARES: A New Laser-ranged Satellite for Fundamental Physics and General Relativity. Actual problems of aviation and aerospace systems. vol. 1, pp. 61-73 ISSN: 1727-6853.

[8] A. Bosco, C. Cantone, S. Dell'Agnello, G.O. Delle Monache, M. A. Franceschi, M. Garattini, T. Napolitano, I. Ciufolini, A. Agneni, F. Graziani, P. Ialongo, A. Lucantoni, Paolozzi A., I. Peroni, G. Sindoni

G. Bellettini, R. Tauraso, E. C. Pavlis, D.G. Currie, D.P. Rubincam, D. A. Arnold, R. Matzner, V. J. Slabinski. (2006). Probing gravity in neo with high-accuracy laserranged test masses. International journal of modern physics D. ISSN: 0218-2718.

[9] I. Ciufolini, E. Pavlis, Nature 431, 958 (2004).